UNIVERSITÀ
DEGLI STUDI
DI PADOVA

Sede Amministrativa: Università degli Studi di Padova

Dipartimento di Geoscienze

DOTTORATO DI RICERCA IN : Scienze della Terra

CICLO XXVII

COMPRESSIBILITY AND THERMAL EXPANSION OF GARNETS WITH COMPOSITIONS TYPICAL OF INCLUSIONS IN DIAMONDS

Coordinatore : Ch.mo Prof. Massimiliano ZATTIN

Supervisore :Ch.mo Prof. Fabrizio NESTOLA

Dottorando : Sula MILANI

ABSTRACT

Most of the diamonds formed in the sub-cratonic lithospheric mantle, in the so called 'diamond window', but only 1% of these diamonds have mineral phases trapped as inclusions. Although inclusion-bearing diamonds are so rare, they are geologically important, because they are the only direct and unaltered samples that we have from the Earth's mantle. For this reason, the determination of their pressure of formation (i.e. depth of provenance) is fundamental to better constrain the chemico-physical environment in which they formed.

The pressure of formation can be typically estimated by classical geobarometry methods that are based on the cation partitioning between mantle minerals. However, these methods can only be applied to rare cases (e.g. only when the appropriate set of mineral assemblages is present in the same inclusion within a diamond). Recently, an alternative method has been developed, the 'elastic method'. This method is based on the residual pressure (P_{inc}) of the inclusion still trapped in the diamond while at room conditions (i.e. room temperature and pressure). This P_{inc} arises from the contrast in elastic properties (expansivity and compressibility) between the diamond host and the trapped inclusion regardless the *P-T-t* path taken during the exhumation. In principle this method can be applied to any diamond-mineral inclusion pair, but requires accurate knowledge of the thermoelastic parameters of the diamond host and inclusion and an accurate determination of P_{inc}.

Given that in literature reliable thermo-elastic parameters for diamond already exist, in this thesis I focused on the determination of the bulk modulus and thermal expansion of a series of garnets, which, together with olivines, are the most abundant phase included in diamonds. Garnet inclusions show a broad chemical variability and therefore the key point is to understand the compositional dependence of garnet elastic coefficients. This can be done by determining the elastic properties of the relevant garnet end-members (pyrope, almandine, grossular, and uvarovite) thus retrieving their variation within the solid solutions. This PhD project provides new values of the compressibility and thermal expansion for pyrope ($Mg_3Al_2Si_3O_{12}$), almandine

($Fe_3Al_2Si_3O_{12}$), grossular ($Ca_3Al_2Si_3O_{12}$), and uvarovite ($Ca_3Cr_2Si_3O_{12}$) garnet end-members, determined by in-situ high-pressure and high-temperature single-crystal X-ray diffraction experiments. As a simple proof of concept the elastic properties of a synthetic single crystal with eclogitic-like composition (i.e. $Py_{51}Al_{22}Gr_{27}$) have been determined. In order to test if the compositional dependence of garnet elasticity can be reliably modeled assuming an ideal mixing model the measured elastic coefficients for this complex solid solution ($Py_{51}Al_{22}Gr_{27}$) have been compared to those calculated from the end-member properties. Two sets of entrapment pressures at temperatures typical for subcratonic-lithospheric regions for the eclogitic-like garnet were therefore calculated with the 'elastic method', using both the observed and the extrapolated elastic parameters.

The results show that the differences between the calculated and measured values produced discrepancies in the entrapment pressures of about 0.03 GPa along the entire temperature range considered (e.g. 1000 – 1800 K). Such difference in entrapment pressures cause shifts of less than 1 km in estimation of the depth of formation for the pair. Despite other minor uncertainties that may arise applying the elastic method to garnets still trapped in diamonds (e.g. more complex garnet solid solutions, presence of fractures of the host around the inclusion), these results clearly indicate that the elastic method allows retrieving the pressure of formation for garnet inclusion in diamonds with uncertainties one order of magnitude lower than classical geobarometry.

RIASSUNTO

La maggior parte dei diamanti si sono formati nel mantello litosferico sub-cratonico, e più precisamente nella porzione di mantello definita in inglese come *'diamond window'*. Solo l'1% di questi diamanti contiene altre fasi minerlai incluse. Nonostate la loro rara ricorrenza sono molto importanti nelle Scienze della Terra, in quanto rappresentano gli unici campioni che contengono al loro interno le fasi minerali del mantello terrestre più profonde e non alterate che vengono studiate oggigiorno. Per questo motivo la determinazione della loro pressione di formazione, e quindi della loro profondità di provenienza, è di rilevante importanza per determinare le condizioni chimico-fisiche dell'ambiente in cui si sono formati.

Nella maggior parte dei casi la pressione di provenienza di tali campioni viene determinata applicando la geobarometria classica, che si basa sul partizionamento degli elementi chimici tra i minerali costituenti il mantello. Questo metodo però può venir utilizzato soltanto in rari casi, ovvero quando all'interno dello stesso diamante sono presenti le fasi minerali adatte. Per questo motivo negli ultimi decenni è stato sviluppato un metodo alternativo, definito come metodo elastico. Questo metodo permette la determinazione della pressione di formazione considerando la pressione residua, definita come P_{inc}, alla quale è soggetto il minerale incluso in condizioni superficiali, ovvero a pressione e temperatura ambiente. La P_{inc} è dovuta alle differenze nelle propietà termoelastiche (compressibilità ed espansività) del diamante e dell'incluso. In linea di principio il metodo elastico può essere applicato a qualsiasi diamante contenente una o più fasi minerali incluse, ma è necessaria l'accurata conoscienza dei parametri termoelastici sia del diamante che del minerale incluso.

Dal momento che in passato i parametri termoelastici del diamante sono già stati determinati con accuratezza, nel presente lavoro di tesi mi sono focalizzata sulla determinazione del *bulk modulus* ed espansione termica dei granati, che assieme alle olivine sono le fasi minerali più abbondanti incluse nei diamanti. A causa della complessa variabilità composizionale dei granati è molto importante studiare come le propietà termoelastiche dei granati variano con la composizione chimica. Questo può

essere determinato solamente studiando le propietà elastiche dei termini estremi, quali il piropo, l'almandino, la grossularia e l'uvarovite. Per questo motivo durante il lavoro della presente tesi sono stati determinati dei nuovi valori del *bulk modulus* e dell'espansione termica di piropo ($Mg_3Al_2Si_3O_{12}$), almandino ($Fe_3Al_2Si_3O_{12}$), grossularia ($Ca_3Al_2Si_3O_{12}$) e uvarovite ($Ca_3Cr_2Si_3O_{12}$). Questi parametri sono stati determinati tramite esperimenti di diffrazione a raggi-X ad alta pressione e temperatura in-situ. In conclusione sono state determinate le propietà elastiche di un cristallo singolo sintetico di composizione eclogitica (i.e. $Py_{51}Al_{22}Gr_{27}$). Per verificare se la variazione del bulk modulus misurata può essere calcolata considerando una soluzione solida ideale, è stato fatto un semplice calcolo di media pesata. A questo punto le pressioni di intrappolamento di un granato eclogitico sono state calcolate con il metodo elastico in condizioni di mantello litosferico subcratonico considerando i valori termoelastici calcolati e misurati.

I risulatati ottenuti evidenziano la minima differenza tra la pressione di intrappolamento calcolata con il coefficiente misurato e calcolato, che è di soli 0.03 GPa, nell'intera regione termica considerata (1000-1800 K). Tale differenza nel calcolo della pressione corrisponde a una differenza nella profonditá di formazione di solo 1 km. Nonostante le ulteriori complicazioni che potrebbero comparire con l'applicazione del metodo elastico, come per esempio la presenza di soluzioni solide più complesse e la presenza di fratture, questo risultato dimostra chiaramente la potenzialità del metodo elastico nel calcolare le pressioni di intrappolamento con incertezze di un'ordine di grandezza inferiori a quelle calcolate con la geobarometria classica.

ACKNOWLEDGEMENTS

I would like to thank Prof. Fabrizio Nestola, who gave me the possibility to do a PhD at the University of Padua. I gratefully thank Dott. Matteo Alvaro, Dott. Ross Angel, and Dott. Daria Pasqual for the help in the experimental work, the scientific discussions and the precious support during this PhD. Thanks also to Prof. Paolo Nimis and Prof. Maria Chiara Domeneghetti for the support and suggestions. Thanks to Prof. Stephan Klemme and Dott. Tiziana Boffa Ballaran for the nice periods I had at the Institute of Mineralogy of the University of Münster and at the Bayerisches Geoinstitut, Bayreuth. Thanks also to Dott. Charles Geiger and Dott. Vincenzo Stagno for providing some of the garnet samples used in this study.

I doubt I could have gotten through the PhD without you, Luca. It's all thanks to you, keeping me on the right path, picking me up when I fell down, and always being with me.

THESIS LAYOUT

This thesis consists of an introduction chapter, which provides a brief overview of the current state of knowledge on diamonds and their occurrence, with emphasis on issues addressed in this work, and outlines the particular focuses and aims of the thesis as a whole. The introduction is followed by one manuscript which has been submitted to a peer-reviewed journal (i.e. *Manuscript 1*), one manuscript in preparation (i.e. *Manuscript 2*), and a chapter dedicated to the results obtained in the last high-pressure experiment. The manuscripts develop and discuss in detail specific lines of research that have been pursued during the PhD. A chapter on the analytical and experimental approach describes the methodologies used in this work. The thesis concludes with a discussion on the main results of the work and their bearing on future studies on diamond geobarometry.

CONTENTS

INTRODUCTION

Diamonds are geologist best friends. It is one of the most precious mineral used in jeweler, and being the hardest material known on the Earth it is also used for several industrial/technological applications. Despite diamond has been widely used since long time (e.g. it is mentioned in Indian manuscripts dated more than 2000 years ago), only in the last few decades such material has undergone several detailed scientific investigations. Diamond is in fact the paramount phase to understand evolution and the physico-chemical condition of the Earth's upper mantle mainly because: (i) it is the stable phase through which carbon is stored in the deep mantle for long geologic time; (ii) it does contain and preserve different types of inclusions (fluid, mineral, etc.); (iii) it is the only material sampling mantle to depths of 800 km (Harte et al. 1999; McCammon 2001; Stachel and Harris 2009; Harte 2010), although the majority of the mined diamonds worldwide derive from shallower depth (150 to 250 km). Most of the diamonds formed in the sub-cratonic lithospheric mantle, in the so called 'diamond window' (Fig. 1; Stachel and Harris 2008), however, only 1% of these diamonds have mineral phases entrapped as inclusions (Stachel and Harris 2008). For the purposes of this thesis, only a short introduction on the geology of diamonds is presented. For a more complete review the reader is referred to e.g. Stachel and Harris (2008), Shirey et al. (2013) and reference therein.

The study of these mineral inclusion trapped in diamond allows retrieving several pieces of information about the earth interior and its active geodynamics providing the definition of the initiation of subduction processes (Shirey and Richardson 2011), tracking the transfer of material through the mantle transition zone (Stachel et al. 2005; Walter et al. 2011), recording the timing of ingress of fluids to the continental lithosphere (Richardson et al. 1984; Pearson et al. 1998; Shirey et al. 2004), preserving carbonatitic fluid that trigger deep mantle melting (e.g. Schrauder and Navon 1994; Kopylova et al. 2010), capturing the redox state of the mantle (e.g. Rohrbach and Schmidt 2011), and providing samples of primordial noble gases (e.g. Ozima and Igarashi 2000).

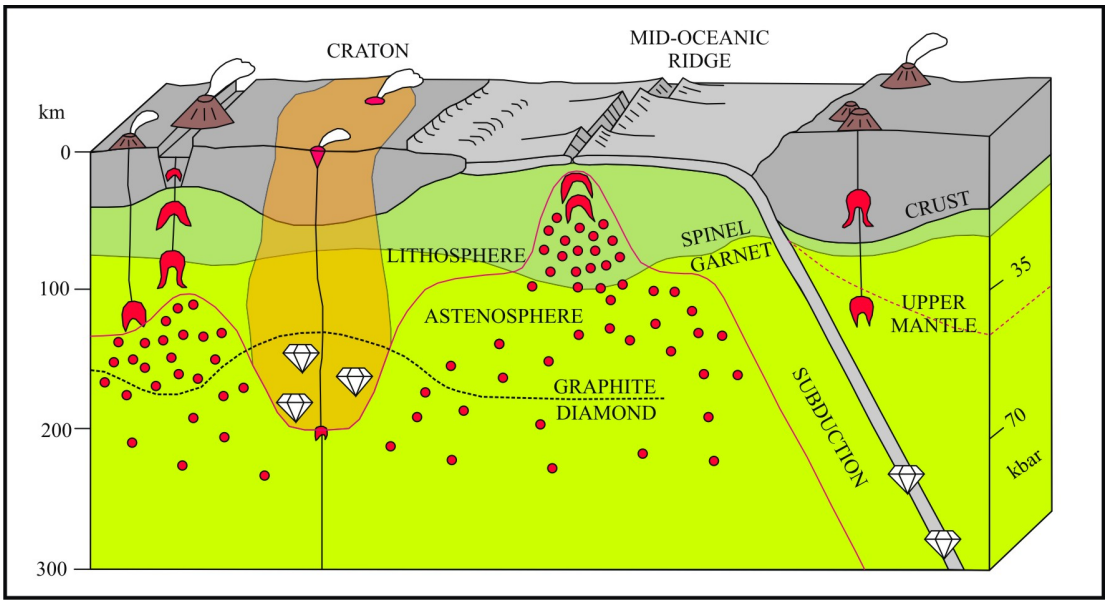

Fig. 1 - Schematic vertical section of the Earth's crust and part of the upper mantle (after Stachel and Harris 2008).

Although inclusion-bearing diamonds are so rare, they are geologically important, because they are the only direct and unaltered samples that we have from the Earth's mantle. For this reason the determination of their pressure of entrapment (i.e. depth of formation) is important to better constrain the chemico-physical environment in which they formed. The pressure of formation (P_e) can be estimated using two different approaches. The traditional method is based on the cation partitioning between mantle minerals (i.e. classical geobarometry). The greatest disadvantage of this method is that can only be applied to rare cases for instance only when the appropriate set of mineral assemblages is enclosed in a single diamond. An alternative method based on the residual pressure (P_{inc}) of the inclusion still trapped in the diamond at room temperature and pressure has been recently developed (e.g. Izraeli et al. 1999; Angel et al. 2014a,b). The P_{inc} arises from the different elastic properties (expansivity and compressibility) of the diamond host and the trapped inclusion, regardless the *P-T-t* path taken upon exhumation. This method can be potentially applied to any single mineral inclusion, but requires accurate knowledge of the thermoelastic parameters of both diamond host and inclusion. For this reason, this thesis is focused on the determination of the bulk modulus and thermal expansion of a series of mineral phases with end-member compositions (i.e. pyrope, almandine, grossular and uvarovite garnets). In addition, we

performed an experiment also on a complex composition in order to understand the variation of elastic properties within solid solutions. This will allow determine the entrapment pressure for garnets with composition similar to those found in diamonds.

Diamonds and their occurrence

Diamond, together with graphite and lonsdaleite, represent the three stable native carbon mineral on Earth. Diamond can crystallize in the Earth's upper mantle, from ca. 150 km down, and it is also present in the crust as a metastable phase. On the basis of their provenence, diamonds can be divided into two major groups, lithospheric diamonds (deriving from the subcratonic lithospheric mantle) and ultra-deep diamonds where the former are the most abundant and constitute about 90% of the diamonds mined worldwide (Fig. 2).

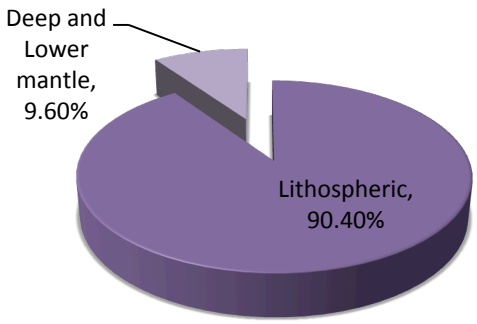

Fig. 2 – Relative abundance of diamond source areas in the earth's mantle (after Stachel and Harris 2008).

Diamond occurs in a variety of forms (e.g. polycrystalline, monocrystalline, and coated diamonds are the three main groups usually considered for geological purposes). Each of these shapes represents different environment of growth that are mainly controlled by supersaturation and resorption phenomena.

Diamond is an rare phase and even if some eclogites are known to contain 10-15% of diamonds, it usually occurs at the part-per-billion (ppb) level even in the most diamondiferous volcanic rocks. Because of its mechanical-physical resistance to dissolution-alteration processes, diamond can also be found at the Earth's surface,

where it is unevenly distributed as it is usually contained as xenocryst within the series of mainly three rare volcanic rocks (e.g. kimberlite, lamproite, and lamprophyre, see Gurney et al. 2010 for further details) that brought it to the surface in accidental circumstances. Kimberlites, directly associated to stable Archean continental nuclei called cratons (Fig. 3) are the most important hosts of diamonds (see Harlow and Davies 2005). Cratons are characterized by a relatively cold and thick (i.e. 250-300 km) lithospheric mantle generally old and tectonically stable with respect to the surrounding asthenosphere. These lithospheric mantle portions are called '*mantle keels*' and is where the so called 'diamond window' is located (see Fig.1). Cratons and kimberlitic magmas are so closely related because it is thought that the deep *mantle keels* of cratons facilitate the production of the kimberlitic magma by deepening the onset of melting of carbonated mantle (Shirey et al. 2013). Lamproites are important diamond-bearing rocks as well being indeed host for the world's largest diamond mines. On the other hand, diamonds in lamprophyres are much more rare with respect to kimberlites and lamproites. The common features of these three types of magmas are that (i) their source region is the deepest of all known magmas; (ii) they derived from a small amount of melting in the deep mantle; (iii) they are volatile and MgO rich and (iv) their upwelling to the surface is incredibly fast (i.e. ca. 30-50 m/s; e.g. Canil and Fedortchouk 1999; Wilson and Head 2007).

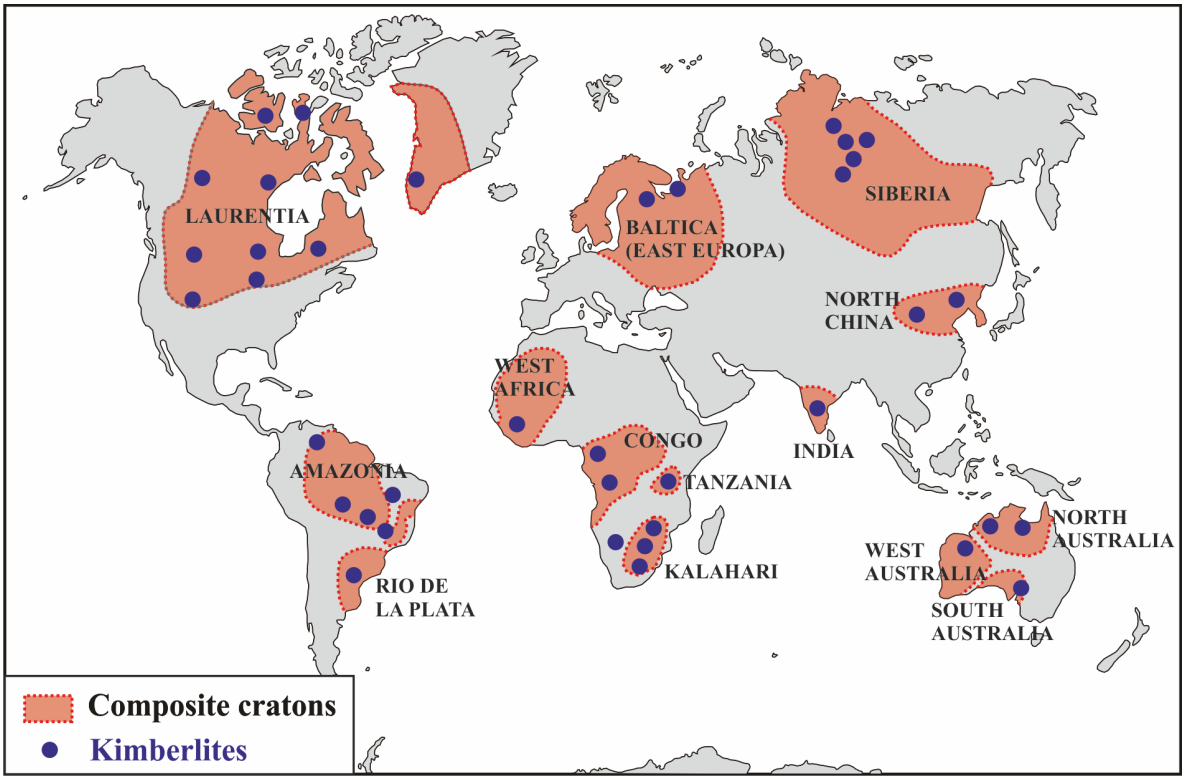

Fig. 3 – Location of major kimberlitic fields and cratons (modified and simplified after Bleeker 2003 and Eckstrand et al. 1995).

Moreover, diamond can be found in ultrahigh-pressure metamorphic rocks (Ernst 2001), which have been exhumed by collision due to orogenic processes. These are often referred to as 'microdiamonds' because of their limited size (10-100 μm). Even though occurrence of microdiamonds has been reported for the first time by Sobolev and Shatsky (1990) their conditions of formation are still a matter of debate (see review of Dobrzhinetskaya 2012). Lastly, diamonds are also found as products of extraterrestrial body impacts on the Earth's surface (generally called 'impact diamonds', Frondel and Marvin 1967; Nemeth et al. 2014).

Inclusions in diamonds

As mentioned above, only a small amount of diamonds contain mineral, fluid or melt inclusions which have been trapped during diamond formation. Mineral inclusions in diamonds from the subcratonic lithospheric mantle are mostly represented by garnet,

olivine, clinopyroxene, orthopyroxene, Mg-chromite and sulphides (Fig. 4). Among these olivine and garnet are certainly the most abundant (Fig. 4).

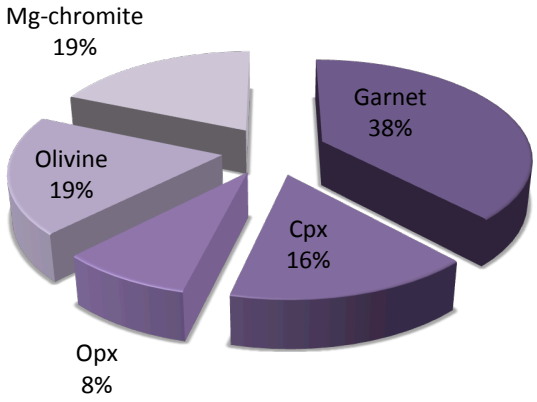

Fig. 4 – Relative abundance of the different mineral inclusions (after Stachel and Harris 2008).

These inclusions represent the only direct and unaltered probe for the Earth's upper mantle which otherwise would be inaccessible for direct observations. However, since mineral inclusions are commonly not bigger than 200 μm, their chemical analyses became possible only after the advance of the electron microprobe technique, with the first work made at the Carnegie Institution (Meyer 1968; Meyer and Boyd 1969) and at the Russian Academy of Science in Novosibirsk (Sobolev et al. 1969; 1970). Since then, geochemical studies on inclusions in diamonds fundamentally changed our understanding of where and when diamonds formed. These analyses led to important discoveries such as the finding that diamonds are genetically unrelated to their host magma, i.e. they are mantle xenocrysts, carrying crucial information about the chemico-physical environment of the mantle before or at the time of the diamond formation. Studies of diamond inclusions and kimberlite-hosted xenocrysts and xenoliths permitted to draw an evolution of cratonic regions. From the first experiments until now many new techniques were developed and applied to the study of diamond inclusions. Unfortunately the majority of these techniques are all destructive. Another crucial step forward in the study of mineral inclusion trapped in diamond has been made by Mitchel and Giardini in 1953 with the employment of X-ray diffraction to identify the mineral inclusions in a non-destructive way. This pioneer work was then followed by a lot of studies on diamonds from Russia (Orlov 1977) and South Africa (Harris et al. 1967).

Inclusions in diamonds can be protogenetic, syngenetic or epigenetic depending on whether the inclusion has formed before, during or after the diamond formation. Common thought was that an inclusion sitting in the middle of the diamond, indicating that it acted as seed for diamond nucleation must be protogenetic. Syngenetic inclusions were instead recognized because they showed a morphology imposed by the host diamond, which is cubic. The epigenetic inclusions formed along cracks, after the formation of the diamond, due to penetration of fluids or melts (Harris 1968); they may form within the Earth's mantle (Kopylova et al. 1997) or after emplacement in the Earth's crust (Meyer 1987). Only based on the mineralogy and mineral chemistry of the inclusions, which in turn reflects the paragenesis of the source rock where the diamond formed, the subcratonic lithospheric mantle can be classified in three suites (peridotitic, eclogitic and websteritic). However, following Stachel and Harris (2008), websterites are the less representative source rocks for diamonds (Fig. 5). Moreover, the peridotitic suite can be further subdivided in three classes, lherzolitic, harzburgitic and wehrlitic. Only on the basis of Cr_2O_3 content of the garnet, which is a fundamental phase occurring as inclusion in diamonds, the distinction between peridotitic and eclogitic suites is possible. On the other hand the websteritic suite cannot be well defined because the Cr_2O_3 and CaO contents overlap with those of the low-Cr_2O_3 peridotitic garnets. Moreover, it is important to highlight that the eclogitic-peridotitic abundance ratio, that is about 1:2 considering the worldwide database of Stachel and Harris (2008), strongly changes if diamonds of greater dimensions are included and if single kimberlite localities are considered. It has been shown by Stachel and Harris (2008) for the Premier and Finsch mines, that if the sieve sizes are increased the eclogitic diamonds become more frequent then the peridotitic one. However, this is not valid for the Venetia mine, where the proportion remains equal (Stachel and Harris 2008).

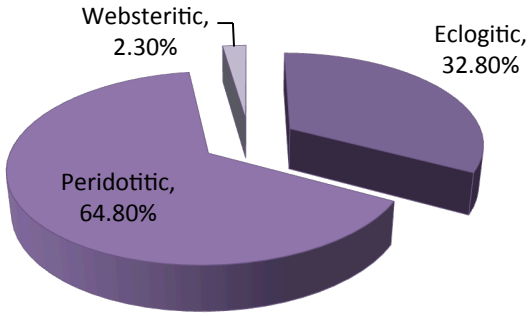

Fig. 5 - relative abundance of diamond paragenesis (after Stachel and Harris 2008). The database includes 2844 inclusion-bearing diamonds.

Garnets

Garnets are the most abundant inclusions and, as mentioned above, play a key role in determining the diamond source rock by means of the Cr_2O_3 and CaO content analysis. The Cr_2O_3 cut-off to distinguish between eclogitic and peridotitic garnets is set to 1 wt% by Gurney et al. (1984). Fig. 6 shows the typical CaO- Cr_2O_3 diagram used to classify mantle garnets. Generally the eclogitic garnets are characterized by a Cr_2O_3 content lower than 0.1 wt%.

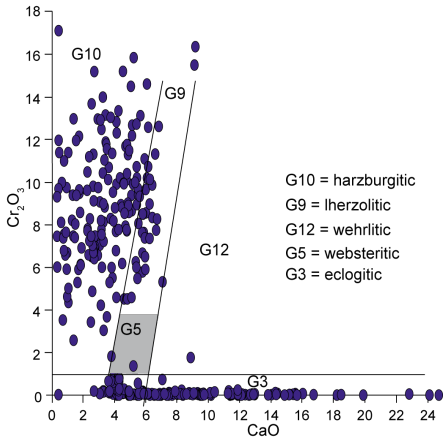

Fig. 6 - Plot of CaO and Cr_2O_3 contents in garnets inclusions in diamonds for literature data (reference list reported in Appendix A). Superimposed is the classification scheme of Grutter et al. (2004), which is one of the commonly used methods to discriminate mantle garnets from different source rock paragenesis. The G5 (websteritic) field overlap with the G9 (lherzolitic) field. Websteritic garnets are distinguished by lherzolitic garnets by having mg# [Mg/(Mg+Fe)] < 0.7.

Peridotitic garnets have a colours ranging from a pale pink to purple, while eclogitic garnets are orange. The average composition expressed in terms of 'classical' end members were calculated from the chemical data of the garnets reported in literature (database of Stachel and Harris, 2008). The average compositions (Fig. 7) are calculated on: 228 analyses for the peridotitic samples, 154 analyses for the eclogitic samples and 22 analyses for the websteritic samples.

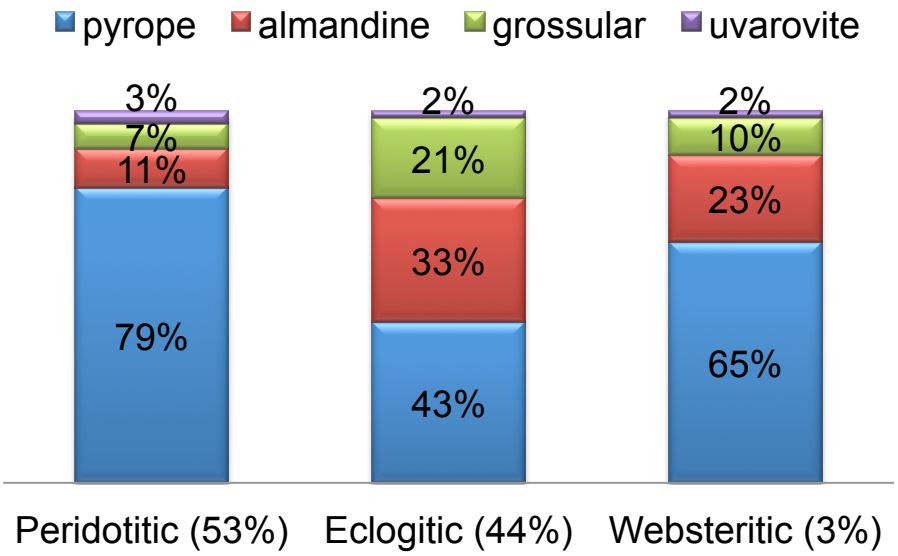

Fig. 7 – Average composition of garnets found as inclusions in diamonds. The composition is expressed in terms of 'classical' end members, which were calculated from the chemical data of the garnets reported in literature (Stachel and Harris 2008 and reported in Appendix A). The average compositions are calculated on: 228 analyses for the peridotitic samples, 154 analyses for the eclogitic samples and 22 analyses for the websteritic samples.

For a more detailed explanation of the major and trace element variation in garnets the reader is reminded to Stachel and Harris (2008) as this thesis is mainly focused on garnets behaviour upon compression and expansion.

Geobarometry of diamond inclusions

So far the pressure and temperature of diamond-inclusion pair has been determined using classical geothermobarometry. Unfortunately this method can be applied in rare cases and it has the big disadvantage that to be applied it needs the chemical composition of our inclusions, which therefore need to be exposed by polishing or breaking the diamond host. Conventional geothermobarometers are calibrated on high-

temperature, high-pressure experiments in simple and complex systems that approach the typical compositions of the mantle rocks. They are based on cation partitioning between two or more minerals in chemical equilibrium which therefore require the coexistence of these minerals in the samples under investigation (e.g. mantle xenolith, inclusions in the same diamond). These conditions are evident limiting factor for the applicability of the geothermobarometers to diamond inclusions for two main reasons: (i) non touching inclusions in the same diamond may have been incorporated in different times and at different *P-T* conditions; (ii) touching inclusions that do not fully represent the mineral assemblage of the source rock. For example garnet and olivine deriving from a lherzolitic source rock probably had enough time to re-equilibrate after being entrapped in the diamond and therefore their chemistry cannot be used anymore for barometric purposes.

Some geothermobarometers require in their formulation only the composition of a single mineral (e.g. Ryan et al. 1996; Nimis and Taylor 2000; Grütter et al. 2006; Simakov 2008; Creighton et al. 2009). Before the development of the elastic method, single-mineral geobarometry was the only suitable method for diamonds containing monomineralic inclusions (Nimis 2002). Although the composition of only one mineral is used in calculations, single-mineral methods are still based on the partitioning of major or minor components between two mineral phases, therefore chemical equilibrium with the missing mineral remains a necessary assumption. Problems in single-mineral thermobarometry may derive from simplified assumptions concerning the composition of the absent mineral and the effect of bulk chemistry variations. This is one of the reasons why most single-mineral thermobarometers tend to produce large uncertainties in the calculation of the *P–T* of equilibration. The most reliable geobarometer for monomineralic inclusions in diamonds is the single-clinopyroxene method of Nimis and Taylor (2000), which can be used only on peridotitic and pyroxenitic clinopyroxenes and shows uncertainties up to 0.5 GPa if its applicability is carefully evaluated (Nimis and Taylor 2000). Geobarometers based only on the compositions of garnet exist (e.g. Ryan et al. 1996; Grütter et al. 2006), but they produce only estimates of a minimum pressure if equilibrium with spinel cannot be proven, making these geobarometers unreliable to estimate the pressures of garnet inclusions in diamonds.

The elastic method

The problems of classic geobarometry mentioned above are even worst if one considers the eclogitic suites, for which no reliable geobarometers exist so far. For all these reasons an alternative method has been developed in the last few decades. As described in angel et al. (2014a,b; 2015) this method is based on the elastic behaviour of our host and inclusion. The two great advantages of the "elastic method" are that can be applied to any single inclusion and is a non-destructive alternative to the chemical geobarometry. It is based on a determination of the residual pressure of an inclusion, P_{inc}, still trapped in diamond at room temperature and pressure (i.e. ambient conditions). This residual pressure arises from elastic properties (expansivity and compressibility) contrast between the diamond host and the inclusion, regardless of the *P-T-t* path taken during the exhumation. This method requires accurate knowledge of the thermoelastic parameters of the diamond host and inclusion and a precise determination of P_{inc}. Among others, an important assumption that needs to be made is that the inclusions under investigation are syngenetic with their host diamond. On the other hand, if they were protogenetic, they will not represent the environment in which the diamond has formed, unless the chemical composition of the inclusions was reset at the time of diamond formation. Other important assumptions implied by the methodology are that (i) the inclusion has to be elastically isolated, meaning that the host has to encapsulate the inclusion and has to be at least 3 times thicker than the inclusion; (ii) the inclusion has to be spherical and (iii) both host and inclusion have to be elastically isotropic; (iv) the host and the inclusion did not undergo plastic or brittle deformation that would lead to at least partial stress release. Obviously this is the first and the simplest example to consider, which can give exact solutions in terms of the entrapment pressure. For all other cases (i.e. the inclusion is not isolated, the host and the inclusion are not elastically isotropic) the entrapment pressure cannot be evaluated algebraically but it has to be considered case by case by finite-element numerical modeling or use of approximations (Angel et al. 2015). Another phenomenon that we have to consider, when we calculate the entrapment pressure with this method, is the role of the relaxation on the host (Angel et al. 2014b).

The basic principle is that we have to imagine a single mineral of a phase (e.g. garnet) that grows or is encapsulated by another mineral phase (e.g. diamond) at a certain *P* and *T* condition. At this stage the cavity in the host will have the same volume as the mineral phase entrapped. At these conditions we do not have any important pressure or temperature gradient across the host. Now, if for example we bring this closed system (formed at high-*P*/*T*) at ambient *P*-*T* conditions the stiffer diamond will expand less than the relatively softer garnet inclusion. The inclusion would then be constrained to a smaller volume (i.e. higher pressure) than what it would have if free to expand. This pressure is the remnant pressure, P_{inc} (see Angel et al. 2015 for further details). Knowledge of this pressure allows backcalculating the P_e at which the pair formed.

The P_{inc} can be determined starting from measurements performed with different techniques such as single-crystal X-ray diffraction (Harris et al. 1970; Nestola et al 2011), microRaman spectroscopy (e.g. Nasdala et al. 2003; Barron et al. 2008) and strain birifrangence analysis (Howell et al. 2010). However, the observed remnant pressure does not correspond to the remnant pressure calculated using solely from the EoS of both phases, because there is a difference at the host/inclusion wall that will force the wall outwards, because the calculated remnant pressure is bigger than the pressure on the host (Angel et al. 2014b). As described in Angel et al. (2014b), it has to be considered, that the $P_{I,\,end}$ is comprise of two parts:

$$P_{I,end} = P_I^* + \Delta P_{I,relax}$$

, where P_I^*, which can be easily calculated from the EoS of the inclusion and host, while the relaxation term, $\Delta P_{I,relax}$, is difficult to estimate. P_I^*. The relaxation term in literature (e.g. Zhang 1998; Izraeli et al. 1999; Howell et al. 2012) was estimated as:

$$\Delta P_{I,relax} = \frac{-3K_I\,(P_{I,end} - P_{H,end})}{4G_H}$$

, where $P_{H,end}$ is the pressure of our host (i.e. in our example it will be the ambient pressure) and G_H is the shear modulus of our host. This equation was derived assuming that the inclusion is elastically isolated, that both the phases are elastically isotropic, and that the elastic properties of both the phases do not change varying the *P* and *T*.

Obviously the last assumption is not correct for the geological environments, which are characterized by huge changes in *P* and *T*. Therefore, Angel et al. (2014b) addressed the estimation of the relaxation term keeping only the first two assumptions. They derived their relaxation term applying the analysis of Goodier (1933) to the isothermal decompression of the host along the isomeke. The volume relaxation term, which results in the pressure relaxation ($\Delta P_{I,relax}$), that they derived applying the analysis of Goodier (1933) and using the notation of Torquato (2002) is expressed as:

$$-\varepsilon_H K_{21}$$

, where ε_H is the strain applied to the host and the parameter K_{21}, is an elastic interaction parameters whose value is dependent on the elastic properties of the host and the inclusion (for further details see Angel et al. 2014b). Once we have considered all the assumptions makes above we first move our host-inclusion system along an isothermal path in a *P-T* space (Fig. 8), considering their equations of state (for more details on EoS see Appendix A). We move our system long this path until the volume of the cavity in the host will perfectly match the volume of the inclusion, so no residual stress will be present anymore. At this point we will lay on an 'isomeke' (Adams et al. 1975), but we will be in the graphite diamond field. The isomeke is a path in the P-T space were the fractional volume change of the cavity in the host ($\partial \mathrm{V_H}/\mathrm{V_H}$) and the inclusion ($\partial V_I/V_I$) are the same (Angel et al. 2015). As described in Angel et al. (2015) the fractional volume change of an unconstrained phase is defined as:

$$\frac{\partial V_H}{V_H} = \alpha_H \partial T - \beta_H \partial P$$

, where α_H is the volume thermal expansion and β_H is the volume compressibility characteristic for the host. The same equation will be used for the fractional volume change of the inclusion. From these to equations we will constrain the changes in the P-T space as:

$$\frac{\partial P}{\partial T} = \frac{\alpha_I - \alpha_H}{\beta_I - \beta_H}$$

As written in Angel et al. (2015) the isomeke is a not straight line path in P-T space, because the variation of α and β for the close system will change differently. As defined

in Rosenfeld and Chase (1961) the only absolute constrain on the slope of the isomeke is that $\frac{\partial P}{\partial T} = 0$ at absolute zero because at this temperature α is zero.

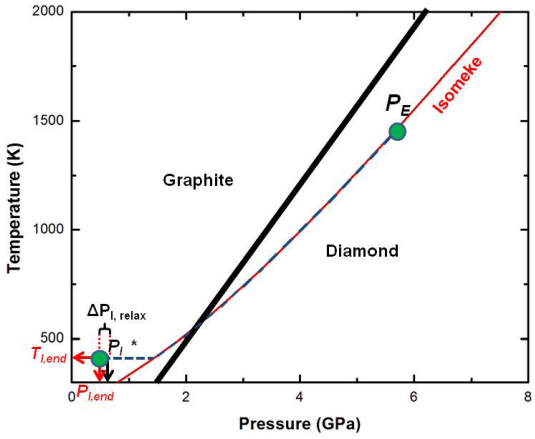

Fig. 8 – The use of an isomeke (solid red line) to calculate the entrapment pressure ($_{Pe}$) starting from room conditions ($P_{I,end}$ and $T_{I,end}$) for a hypothetical pure pyrope trapped in a diamond. The calculation first consider the mutual elastic relaxation of host and inclusion ($\Delta P_{I,relax}$) increasing the pressure to P_I^*, which is the virtual state. After that the pressure is increased isothermally to the isomeke. At last the calculation considers heating along the isomeke to P_e.

EXPERIMENTAL AND ANALYTICAL METHODS

Historical development of high-pressure and high-temperature experiments in Earth Science

The first experimental studies made at high-pressure and high-temperature on minerals and rocks were carried out by Sir James Hall in the 18th century (1761-1832). In his first experiments he reproduced the textures and mineral phase assemblages characteristic for natural basalts. After his experiments not much progress was made in experimental petrology and mineralogy. Meanwhile physicists and chemists became interested in high-pressure and high-temperature experiments. Percy W. Bridgman (1882-1961) probably was the most important pioneer of high-pressure experiments in the first half of the 20th century. In the same period, Tuttle and Bowen (1958) carried out experiments using cold seal pressure vessels. Boyd and England (1960) designed the piston cylinder device that allowed first experiments under upper-mantle conditions in non-specialized laboratories. In the meantime, two different groups, one at the University of Chicago (Jamieson et al. 1959) and the other one at the National Bureau of Standards (Weir et al. 1959), developed the diamond anvil cells. At the same time were designed the multi-anvil presses (Hall, 1958) with many further modifications and improvements (e.g. Kawai and Endo, 1970). Since the very first design by Hall (1958) so far these are the most frequently used devices to study in-situ investigation of rocks and/or minerals at extreme conditions. The multi-anvil apparatus and the diamond-anvil cell are two devices designed to generate high-pressure maintaining the sample under hydrostatic conditions.

Syntheses of gem-quality single crystals

Given the chemical compositions of garnet still trapped in diamonds (Table 1, Fig. 7) the project started from the investigation of the pyrope-almandine solid solution, which account for ~ 80 wt% of the total composition of these garnets. In situ high-pressure and high-temperature X-ray diffraction experiments were performed on synthetic single crystals of pure pyrope, almandine, and $Py_{60}Al_{40}$, which were kindly provided by Dr. Charles Geiger. In order to consider all the 'major' garnet end-member components, i.e. those that can affect the calculated average bulk modulus and thermal expansion value (Table 1, Fig. 7), synthetic single crystals of grossular

and uvarovite were needed as well. Syntheses were carried out at the Insitut of Mineralogie (Westfalische Wilhelms Univertaet, Muenster) and at the Bayerisches Geoinsitut, BGI (University of Bayreuth, Bayreuth). To obtain gem quality synthetic single crystals of garnets different approaches were used, which are described in the following sections.

	Peridotitic	**Eclogitic**	**Websteritic**
	65%	33%	2%
pyrope	79.3%	42.9%	64.5%
almandine	10.5%	33.1%	23.3%
grossular	6.6%	21.1%	9.9%
spessartine	0.6%	1.0%	0.7%
uvarovite	2.5%	0.7%	0.5%
andradite	0.2%	0.1%	0.5%

Table1 - Average compositions expressed in terms of 'classical' end members were calculated from the chemical data of the garnets reported in literature. The average compositions are calculated on: 228 analyses for the peridotitic samples, 154 analyses for the eclogitic samples and 22 analyses for the websteritic samples.

Flux method

The first syntheses were attempted using the simple technique that makes use of a relatively common equipment, which includes a platinum crucible, oxide powders, and a furnace. This is a solution growth technique, the so called 'flux method'. The starting materials are mixed with a solvent, the flux, which decreases the melting temperature of the oxide powders (reactants), used for the synthesis. The key features for a flux are: (i) having a low melting temperature; (ii) being easily separated from the products; (iii) not forming a stable phase with the reactants; (iv) needing a large difference between the boiling and melting point. In order to obtain uvarovite and grossular single crystals the syntheses were made following the experiment done by Lowell et al. (1971). The starting material was prepared by grinding an intimate mixture of different oxides in an agate mortar for ca. 1 hour under ethanol.

To synthesize uvarovite single crystals three attempts were made. For all of them the following oxide powders were used: CaO (99.0%, Alfa Aesar, Johnson Matthey Company), Cr_2O_3 (99.999%, Aldrich Chemical Company), SiO_2 (99.9%, Alfa Aesar, Johnson Matthey Company) for the uvarovite and Na_2O, K_2O and B_2O_3 for the flux.

For the first experiment the platinum crucible (Fig. 9a) with the oxide mixture was put in the furnace (Fig. 9b) and heated from room temperature to 473 K in 1 hour, and from 473 to 1273 K in 8 hours, to permit the decarbonation. After 24 hours the mixture was not molten, so the temperature was increased to 1473 K for 2-3 hours and then the sample was taken out the furnace.

Fig. 9: a) platinum crucible used for the syntheses and b) furnace used for the heating of the samples.

The first experimental product shows inhomogeneities and non-reacted parts in the synthesized uvarovite crystals (Fig. 10a, b). Therefore, a second experiment was performed using different oxide proportions with respect to the previous experiment. This time the mixture was of stoichiometric uvarovite composition, with Na_2O, K_2O and B_2O_3 powders in molar proportion 1:1:1.3 (Table 1C), used as flux. In both the first and second experiments the majority of the uvarovites are 80-90 μm in dimension, but there are also bigger crystals that are ~ 200 μm. However, both showed evidence of large interaction between the flux and the platinum crucible. A further synthesis with a lithium-tetraborate flux (Table 2C) was therefore carried-out. The interaction with the crucible was avoided, but the synthesized crystals were too small for our purposes.

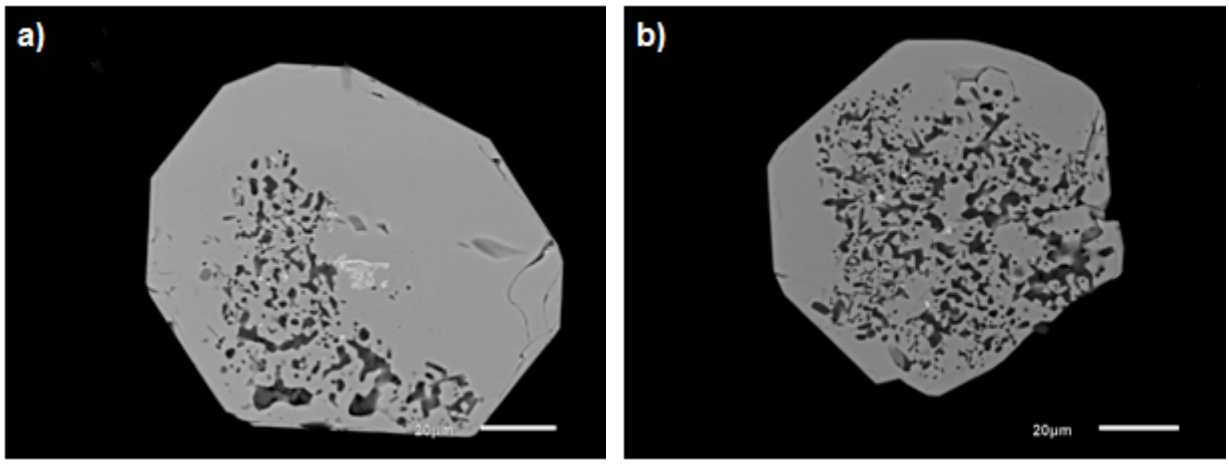

Fig. 10 – Synthetic single crystals of uvarovite obtained with the first experiment. The white inclusions represent unreacted Cr-rich oxides, while the darker areas are inclusions of unknown composition.

The oxides powders used for synthesizing grossular garnets were: CaO (99.0%, Alfa Aesar, Johnson Matthey Company), Al_2O_3 (99.999%, Aldrich Chemical Company), and SiO_2 (99.9%, Alfa Aesar, Johnson Matthey Company) mixed in stoichiometric amounts to obtain grossular composition; the flux used for these experiments was a lithium-tetraborate powder. A first experiment was run at room pressure condition and at 1123 K. In this case the flux was the15 wt % of the total amount (Table 3C). After two days nothing was molten, so the temperature was increased to 1223 K and kept for three days. After that the crucible was taken out the furnace, but no crystals were formed. In order to decrease the melting point of the mixture, 3g of a lithium-borate flux in molar proportion 2:1 was used in a second experiment (Table 4C). This molar proportion was used because of the low melting point as indicated in Ferreira et al. (2010). Again, no crystals formed, so a third experiment was done at the same condition as the second one, but the LiOH.H2O powder was dehydrated before the experiment, heating it at 573 K for 1 hour. Also in this case nothing crystallized. Given the low temperature stability field of grossular at ambient pressure (< 1123 K; reference), syntheses at higher temperatures with this methodology were not possible.

Cold-Seal-Pressure Vessel

Because of the unsuccessful synthesis of grossular using the flux method, syntheses of single crystals were attempted also at higher pressures by means of a cold-seal-pressure vessel (Fig. 11). With this procedure single crystals were grown hydrothermally. The experiments were performed at the Waestfalische Wilhelms Universitaet, Muenster. The hydrothermal ‘cold-seal’ apparatus follows the original ‘Tuttle design’, which utilizes the Bridgman seal (Fig. 12) (Tuttle 1949). Because of the large internal volume, it could either be used for the preparation of relatively large amounts of material or to run several samples of different composition under identical-temperature conditions. For the latter case the different starting composition are sealed in different metal capsules (i.e. in our case gold capsules, see Fig. 13). The system consists of high performance Mo-based metal autoclaves connected to a pressure system via a seal placed outside the furnace and cooled with is water. The autoclaves are externally heated by custom made Kanthal-wired high-temperature furnace. The employed system is pressurized with water and which allows to reach pressures up to 500 MPa and temperatures of about 800 °C. Pressure is generated

manually but is constantly monitored and the relative data are logged by a Labview based software.

Fig. 11 – Cold-Seal-Pressure-Vessel at the Institut für Mineralogie, Westfälische Wilhelms Universität, Münster.

The oxide mixture (Table 5C) was placed in a gold capsule with ca. 7% of water. The capsule was kept at 1073 K and 2 kbar for two weeks.

Fig. 12 – a) Pressure vessel used for the experiment and b) sketch of the pressure vessel (modified after Tuttle 1949).

Fig. 13 – Gold capsules used for the synthesis of garnets in hydrothermal conditions.

After the experiments the capsule was opened and the experimental product was analysed by optical microscopy to seek for garnet single crystals. Unfortunately, with this method I had been able to obtain only grossular powder with no suitable sized single crystals (< 80 μm).

Multi-anvil press

The most successful technique to synthesize single crystals of grossular and uvarovite garnet has revealed to be the multi-anvil apparatus (Fig. 15). High quality crystals characterized by sharp and intense diffraction peaks were obtained, as required for *in-situ* single-crystal X-ray diffraction experiments at high pressure and high-temperature.

Fig. 15 – Hymag-multi-anvil press at the Bayerisches Geoinsitut.

Stoichiometric mixtures of high-purity oxide powders (see Table 7C) were grinded in an agate mortar for 1 h under ethanol and then decarbonated at 1000 °C for 360 minutes; the temperature from 25 °C to 1000 °C was reached in 660 mins. The starting compositions were packed into platinum capsules of 3.5 mm length and

2 mm outer diameter. Water was used as a flux and was injected into capsules via a microsyringe. All experiments were performed using a Hymag press, one of the 6/8 Kawai-types of multi-anvil press (Kawai and Endo 1970) available at the Bayerisches Geoinstitut (Fig. 15), reaching 6 GPa and 1300°C. The experimental charge was heated in 23 minutes and the temperature was kept to 1300°C for 40 minutes. Relevant details of the press and of the assembly used for these experiments are reported in the following paragraphs. For more specific details about the experimental design the reader is referred to Keppler and Frost (2005).

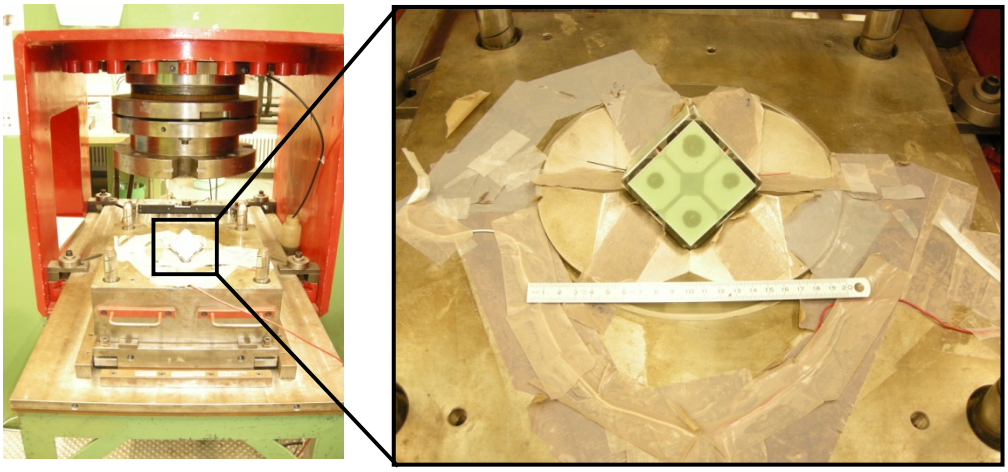

Fig.16 – Details of a 6/8 Kawai-type multi-anvil press with a completed 8-cubic packet of anvils placed on the lower part of the outer set of steel anvils. The total lenght of the ruler is 20cm.

The 6/8 Kawai-type multi-anvil press is characterized by an outer set of six hardened steel anvils, cut as segments from a cylindrical systems, shaped to compress an inner cubic packet of eight tungsten carbide (WC) cubic anvils each with a truncated corner (Fig. 16).

The outer anvils are mounted in two opposing steel guide blocks that are driven together using a uniaxial press (Kawai et al. 1973). When the eight WC anvils are assembled an octahedral cavity forms in the middle (Fig. 17). Gaskets, usually made of pyrophyllite, must be placed between the anvils (Fig. 17) in order to support the truncations and seal in the high-pressure region. In the inner hole an octahedron made of MgO doped with 5% Cr2O3 is placed

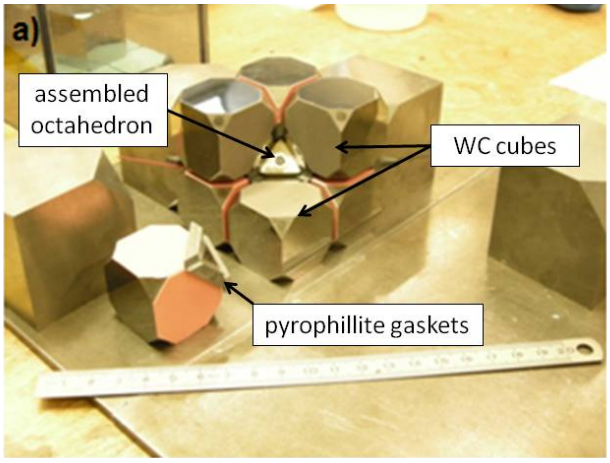

Fig. 17 – The eight WC anvils with the assembled octahedron placed in the inner cavity. Pyrophyllite gaskets are placed between the cubic ancvils.

as a pressure transmitting medium (Fig. 17). A hole is drilled in the octahedron in order to insert a tubular resistance heater, which in all our experiments was made of graphite (Fig. 18). A really important feature is the isolating material put around the heater; this prevent an excessive heat transport to the WC anvils, which enhance plastic deformation of the gaskets and increase the possibility to brake the WC anvils. For this reason in all the assemblies a cylindrical zirconia (ZrO_2) sleeve (Fig. 18) was put between the octahedron and the heater. ZrO_2 sleeves are effective

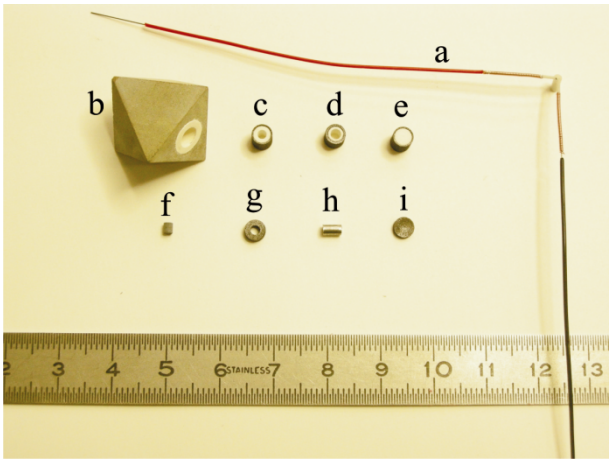

a) Thermocouple with the Al_2O_3 tube and two copper wire coils;

b) Octahedron with ZrO_2 sleeve;

c), d), e) graphite heater with inside the MgO sleeves;

f) pyrophyllite spacer;

g), i) graphite tops;

h) platinum capsule.

Fig. 18 – Components of an 18/11 octahedral high-pressure assembly used in the 6/8 multianvil.

insulators because the ZrO_2 is characterized by a much lower thermal conductivity (2.7 $Wm^{-1}K^{-1}$) compared to MgO (42 $Wm^{-1}K^{-1}$). The capsules are placed in the middle of the assembly and are separated from the graphite heater by an MgO sleeve (Fig. 18). MgO spacers are used below and above the capsules, where the above spacer is characterized by a hole for the insertion of an alumina (Al_2O_3) tube with for holes,

in which we insert a W3%Re97-W25%Re75 thermocouple (wire Ø = 0.25 mm) (Fig. 18). This kind of thermocouple is preferred to Pt-Rt13%Rh or chromel-alumel, because of the smaller pressure effect on the measured voltage (Takahashi et al. 1993; Li et al. 2003) and has a high melting temperature. Thermocouple wire can easily break because of tensional stresses during the extrusion of the gaskets occurring upon compression. For this reason copper wire coils, which can survive to significant extension, are placed in the gaskets as protection to the thermocouple wires. Moreover, graphite plugs are placed on the bottom and the top of the assembly, where latter has a hole that allows to put a phyrophyllite holder (Fig. 18). At this stage everything is assembled and can be fixed with alumina cement (Fig. 19).

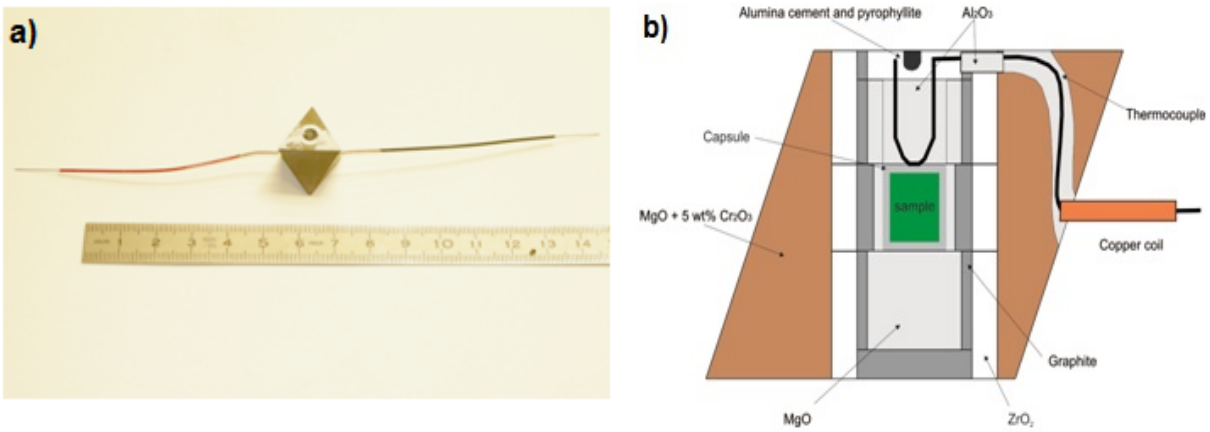

Fig. 19 – Assembled octahedron a) and a cross section of an assembled octahedron b).

Now the octahedron can be placed in the octahedral cavity formed by the eight WC anvils (Fig. 17a). The cubes are finally packed together using epoxy impregnated fiberglass laminate sheets (Fig. 20) in order to ensure electrical insulation from the guided six anvils.

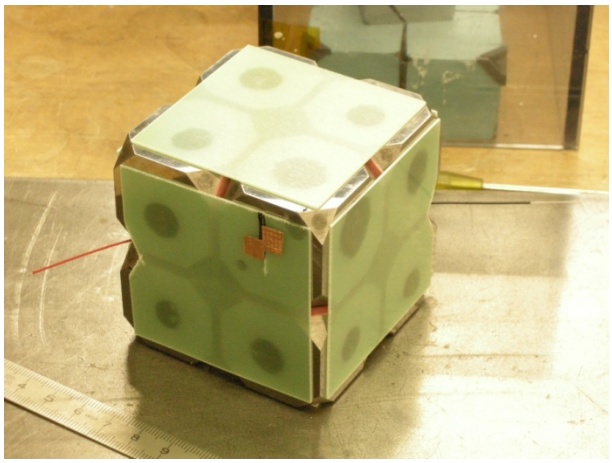

Fig. 20 – Eight WC cubic anvils packed together with impregnated fiberglass laminate sheets

to ensure electrical insulation from the guided six anvils.
The sample pressure in a multi-anvil needs to be calibrated as a function of applied load using phase transformations that occur at known conditions. The pressure calibration procedure is explained by Keppler and Frost (2005). The heating system and the thermocouple was connected to a Eurotherm® controller, which allows to control the heating power while simultaneausly checking the temperature. In the case of malfunctioning of the thermocouple, the temperature was estimated from the electrical power, based on previous experiments at the same conditions and with the same employed cell assembly.

Sample characterization

Electron microprobe analyses

Detailed major element analyses of the uvarovite and grossular garnets were performed with a Cameca SX-50 electron microprobe (IGG-CNR, Padua, Italy), equipped with four wavelength-dispersive spectrometers. Natural and synthetic minerals (wollastonite for Ca and Si, albite for Na, orthoclase for K, and pure Al, Mg, Cr, Fe, and Mn–Ti oxides) were used as standards. Analytical conditions were a 20 kV accelerating voltage, a 20 nA beam current, and a beam size of about 1 μm. Time counting was 10 s for peak and 5 s for background. X-ray counts were converted into weight percent oxides by using the CAMECA-PAP program. Estimated precision of the analysis are within ± 1–2 relative % for major and ± 2–5 relative % for minor oxides. The oxide wt% and the atoms per formula units (a.p.f.u.) based on 12 oxygens are reported in Table 1 in Manuscript 2.

In-situ high-pressure single-crystal X-ray experiments

The high-pressure experiments presented in this thesis have been carried out at the Department of Geosciences, University of Padova (Italy) and at the Bayerisches Geoinsitut, University of Bayreuth (Germany) using a STADI-STOE four-circle automated diffractometer (Fig. 21a), and a HUBER four-circle diffractometer (Fig. 21b) respectively.

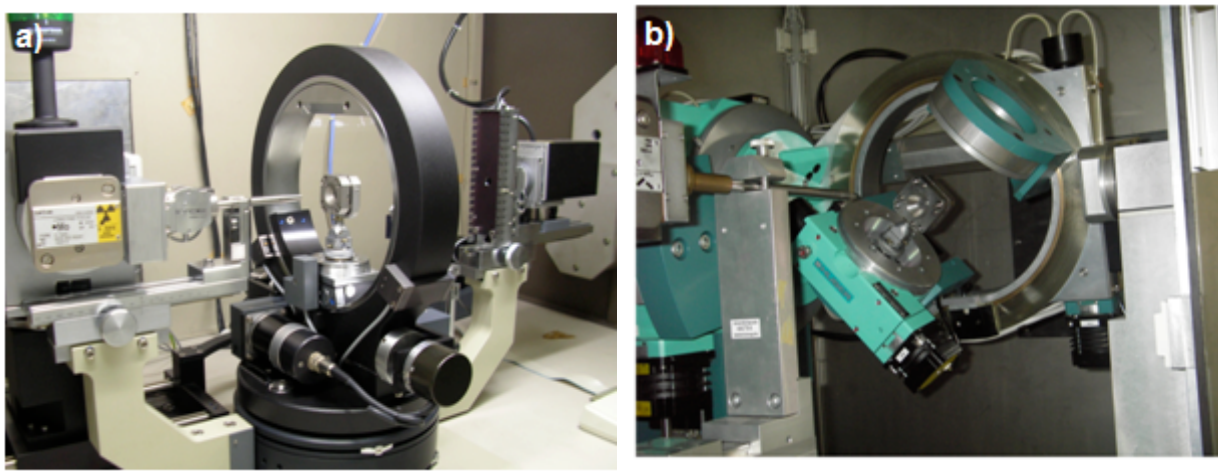

Fig. 21 – a) STADI-STOE four-circle diffractometer at the University of Padova and b) the HUBER four-circle diffractometer at the Bayerisches Geoinsitut. Both the diffractometers are equipped with a point detector.

Both the diffractometers were equipped with a point detector, operating with MoKα radiation at 50 kV and 40 mA and automated with SINGLE software (Angel and Finger 2011). Six different experiments were performed and the samples were loaded in an ETH-type diamond-anvil cell (DAC; Miletich et al. 2000) (Fig. 22) using a steel gasket, pre-indented to 100-110 μm of thickness and with a hole diameter of 230-250 μm.

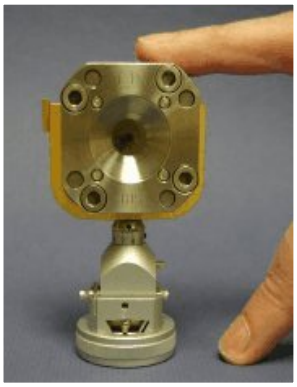

Fig. 22 – An ETH-type DAC (Miletich et al., 2000).

A 4:1 methanol:ethanol mixture was used as pressure transmitting medium, which remains hydrostatic up to about 9.5 GPa (Angel et al. 2007). For each experiment a single crystal of quartz was loaded in the DAC and used as a pressure calibrant (Angel et al. 1997). The unit-cell parameters were determined by centering not less than 27 reflections for each pressure step, in the 2θ range. The effects of the crystal

offsets and the diffractometer aberrations were removed by using the eight-position centering method (King and Finger 1979). Unconstrained unit-cell parameters always confirmed the cubic symmetry of garnet within 1 e.s.d.. Constrained unit-cell parameters were obtained by vector least-squares fit (Ralph and Finger 1982). The unit-cell edges and the relative unit-cell volumes for the three samples at different pressures are reported in Tables .

Diamond-anvil cell (DAC)

Diamond-anvil cell is the standard device to generate hydrostatic high-pressure environment in non-specialized laboratories. Nowadays, the diamond-anvil cells used for X-ray diffraction are characterized by opposing-anvil geometry. Two modes of diffraction geometry are used for high-pressure single-crystal X-ray diffraction experiments, the transmission and transverse geometry. In the transmission mode, which is the most used, the incident X-rays pass through the diamond, the sample, and the opposing diamond (Fig. 23a). In the transverse mode the incident and diffracted X-ray beams pass through the same diamond (Fig. 23b).

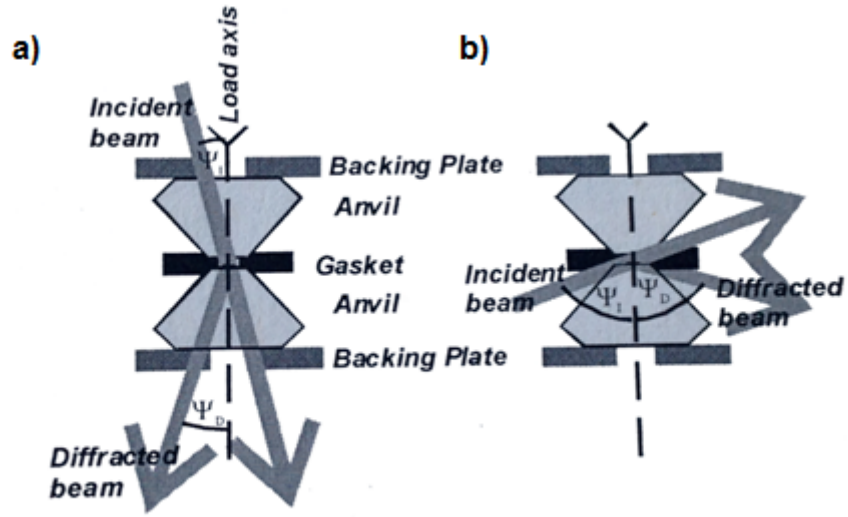

Fig. 23 – a) Transmission and b) transverse mode of diffraction geometry used in high-pressure, single crystal X-ray diffraction experiments (Angel, personal communication).

The basic working principles behind gasketed diamond-anvil cells are simple. The sample is placed in a pressure chamber created between the opposite diamond culets (the flat parallel faces) (Fig.24) of the two opposite-diamond anvils and the preindented and perforated gasket (metal foil) (Fig. 24). Inside the pressure chamber,

together with the sample under investigation a pressure calibrant (i.e. crystal of quartz for all of our experiments) (Fig. 25) and a pressure transmitting medium (i.e. in our experiments a mixture of methanol:ethanol 4:1), usually a fluid or a gas that exerts hydrostatic pressure onto the sample and the pressure calibrant are also placed.

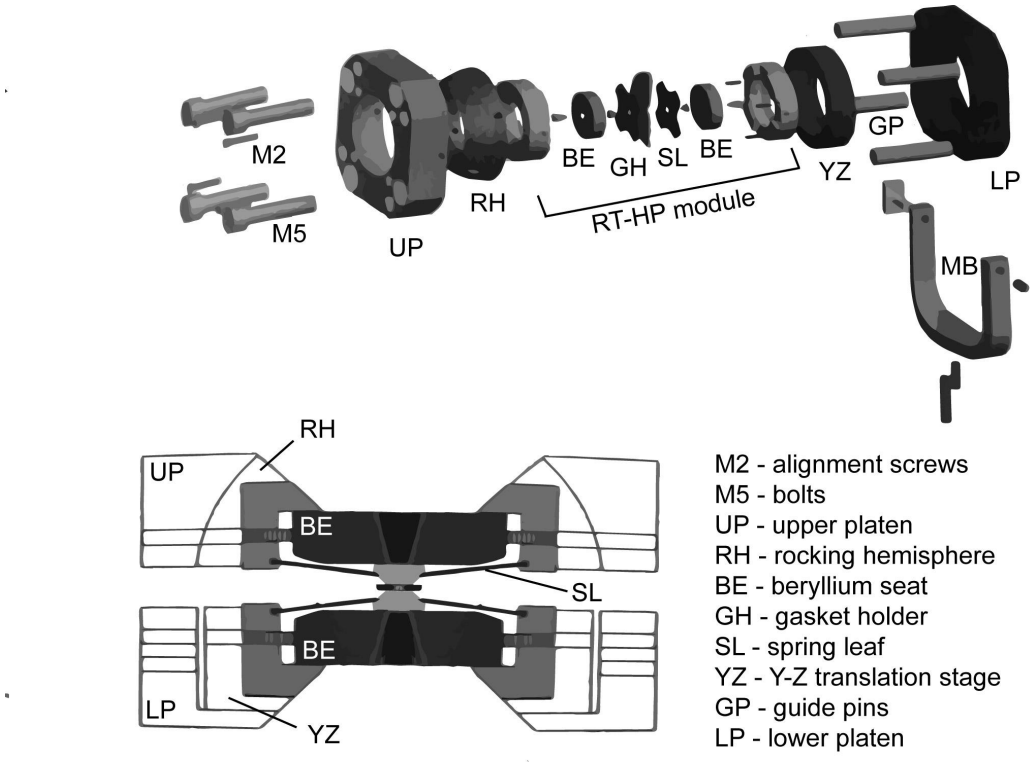

Fig. 24. – View section and exploded view of an ETH diamond-anvil cell (after Miletich 2000).

Fig. 25. – Photo of the pressure chamber with the sample and the crystal of quartz used as a pressure standard.

The pressure is generated by mechanically forcing together the two opposite diamond anvils. In most cases the force required is small, even to reach very high pressure. The basic features of a diamond anvil cell assembly (i.e. diamond anvils, backing plates; gaskets; pressure transmitting media and pressure standard) are briefly reviewed here below.

Diamonds are used as anvils because are transparent to electromagnetic radiation over a wide spectral range (from infrared to hard X-rays), allowing the *in situ* observation of the behaviour of samples at extreme conditions with different techniques (X-ray diffraction, Raman spectroscopy, Brillouin spectroscopy, etc.).

Diamond is also the hardest known material, being therefore able to maintain the pressure achieved in the chamber during the experiment. The highest pressure achieved in a DAC depends on the design of the anvils (i.e. cut, size of the culets). The majority of the designs are based on a modified brilliant cut where the diamonds are polished to provide anvil culets. This design was developed to maximize back reflections and spectral dispersion, but is not the design that gives the best strength for diamond anvil cell applications. A second design is the Drukker-cut. This cut is characterized by an enlarged table diameter and has an increased anvil angle. The highly stressed shoulder of the brilliant cut has been also removed. The anvils with this design can reach higher pressures, because the anvil can withstand greater applied force. Another aspect to consider is the anvil dimension that is the minimum sample volume, the required pressure, absorption and background effects and cost. Diamond anvils typically used for X-ray diffraction studies are approximately 1/3 carat, have a thickness of more or less 1.5 to 2 mm, and a table and culet diameter of about 3 mm and 0.6 mm respectively. The most critical parameters, that needs to be accounted while assembling an experimental mount, are those concerning the alignment of the diamond culets (both transverse and radial). The alignment tolerance between the culets has to be typically of the order of few microns and has to be maintained during the whole experiment.

Diamond anvils are supported in place by backing plates made of a stiff material, which needs to be as transparent as possible to the chosen radiation. In the majority of the DAC this material is polycrystalline beryllium. Advantages of the beryllium backing plates are that is are essentially transparent to X-rays, it can support almost the whole diamond table and is relatively easy to be machined. On the other hands beryllium has several disadvantages. It is a highly toxic material, the discs on the detector side of the cell cause a high and structured background (i.e. create its own powder-diffraction pattern) and the strength of this metal decreases rapidly on heating and/or cooling. Tungsten carbide is another material used to produce the backing plates. It is not toxic, its mechanical properties last over a wide range of temperatures, but the X-ray access is considerably decreased with respect to that of beryllium. An alternative material is boron or boron-carbide which is stiff and has a much lower X-ray absorption compared to beryllium (Adams and Christy 1992). However, because of the relatively low tensile strength discs are machined without the optical access hole. Lastly, diamond backing plates has been firstly proposed by Miletich et al. (2000), because this would allow (i) to generate higher pressures

(Yamanaka et al. 2001) and (ii) to significantly improve the quality of the structure refinements because, being single crystals they do not give rise to high and textured background (Miletich et al. 2000; Periotto et al. 2011).

The gasket is used to provide an encapsulated chamber in which the pressure transmitting medium is contained to apply hydrostatic pressure to the samples. It also provides mechanical support to the anvils at high pressure and prevents their failure due to the enormous shear forces at the anvil tips. The pressure that the gasket can support depends on its thickness, the diameter of the hole, and the shear strength of the material (Dunstan 1989). For the pressure ranges achieved in our experiments the gasket was 250 μm thick and preindented to a thickness of 90-110 μm. A hole of ca. 250 μm was drilled in the center of the preindentation. The gaskets used in the experiments were made of steel T301, but they can be also made of rhenium, martensitic tool-steel or alloys such as inconel or Cu-Be.

The pressure transmitting medium for single crystal studies, and in particular for diffraction experiments, is fundamental in order to guarantee the maximum pressure homogeneity to the entire sample(s) and calibrant(s). The medium has not to be affected by any differential stress or shear strain over the entire pressure range of the experiment (see Miletich et al. 2000 for further details). As a consequence crystals have to be immersed in a medium that displays hydrostatic behaviour. Such medium can be liquid, gaseous or a soft solid. Another noteworthy characteristic of the pressure medium used is that it must not dissolve and/or modify the high-pressure behavior of the sample(s) (i.e. it does not enter in the sample structure, see Hazen 1983 and Lee et al. 2002 for further details). The non-hydrostatic environment may lead to several undesirable problems; for instance, the non-hydrostatic stresses can modify the relative evolution of the unit-cell parameters with pressure (Angel et al. 2007 and references therein) and can affect pressure determination by the commonly used ruby fluorescence technique or by internal diffraction standard (Angel et al. 2007 and references therein). Therefore non-hydrostatic stresses may affect results from equation of state and elasticity studies (Angel et al. 2007). In our experiments a 4:1 mixture of methanol:ethanol, commonly used for SC-XRD studies, was used a pressure transmitting medium. This medium remains hydrostatic to the maximum pressure reached during our experiments (Angel et al. 2007) and is easy to load into the DAC.

As it is not possible to directly calculate the pressure from the applied load because the distribution of the load over the anvils is unknown as well as the amount

of losses due to internal friction and plastic or elastic deformation the accurate and precise determination of the pressure is one of the greatest issue during high-pressure experiments. Uncertainties arising from pressure determination are reduced using a well calibrated secondary standard material (i.e. quartz, fluorite or ruby).

In diamond-anvil the laser-induced fluorescence technique applied to luminescence sensors cells is commonly used. The advantages of this technique are that the luminescent crystals, (i.e. ruby or REE-doped oxyhalogenide crystal) need to be only few microns sized so they only occupy a small volume portion of the pressure chamber. These standard crystals contribute very little to the diffracted beam, it is quick and easy to use. Although the wavelength shift can be measured with a precision better than 0.01 GPa in pressure, the residual data scatter in diagrams with unit-cell volume against the pressures determined with the ruby fluorescence technique is greater than the estimated uncertainties. This issue may arise because of the strong temperature dependence of the ruby spectrum and/or the actual pressure change due to differential thermal expansivity of the components of the DAC. The ruby fluorescence measurements are made out of the diffractometer and this could cause few degrees change in temperature inside the DAC pressure chamber (5-6 K temperature difference gives the same shift as a 0.1 GPa pressure change as showed by Vos and Schouten 1991). The relatively simple solution to this problem is to use an internal diffraction standard that allows determining the pressure almost simultaneous with the sample measurements (i.e. with no need to remove the DAC from the diffractometer). The basic idea is that the pressure is determined measuring the unit-cell volume of a material for which the EoS coefficients have been previously calibrated against pressure. Therefore the measured unit-cell volume of the calibrant can be converted via EoS to pressure. A good calibrant materials have to encompass important characteristics:

(1) high symmetry and small unit-cell volume, to ensure the minimum interference with the diffraction peaks of the sample (i.e. ease of identification);
(2) significant unit-cell variation with pressure, to ensure calibration sensitivity;
(3) chemical and structural stability (absence of phase transition);
(4) strong diffraction intensity to minimize the physical sample volume;
(5) very low mosaicity and minimal crystal defects, that decrease the diffraction peaks frame halfwidhts maximum (FHWM);

(6) no reactivity with the chosen pressure transmitting medium.

In all of our experiments quartz was used as a standard pressure material. Quartz is the SiO_2 polymorph stable at ambient conditions and it does not undergo any phase transition until moderate pressures. The determination of the pressure with quartz leads to a precision of the order of 0.005-0.010 Gpa up to 10 Gpa. This calibrant provides an improvement of almost one order of magnitude over any of the previously used pressure calibrants (i.e. NaCl, gold, fluorite etc…). Moreover, its hexagonal symmetry allows an internal cross-check for even small non-hydrostatic stresses which would reflect in the unit-cell parameters changes with pressure.

ETH-type DAC

For our experiments we used the ETH-type DAC. This diamond anvil cell is a development of the former BGI-type cell (Allan et al. 1996), which is in turn a merge of that developed by Merrill-Bassett (1974) together with that of Mao-Bell (1980). The main features of this ETH-type DAC are:

(1) modular concept, which means that it has replaceable and exchangeable inner modules, each of them made for specific applications (standard room-temperature single crystal module, spectroscopic module and heatable single-crystal module);
(2) stable pressure generation that is possible through two pairs of right- and left-handed bolts with threads of half the standard pitch, which allow the pressure to be changed in small and more controllable increments;
(3) pressure stability is achieved through four tight-fitting guide pins which connect the two basic carrier platens;
(4) axial and radial alignment of anvils is achieved thanks to a ball-and-socket mechanisms for adjusting the parallelism of the opposing diamond culets;
(5) the cell geometry allows opening angles of maximum 45°;
(6) quick and reproducible positioning of the DAC which, thanks to the three-point mounting bracket and the two guide pins, can be mounted on goniometer head or sample stage in a relatively quick more precise manner within a few microns tolerance once the cell has been aligned.

High-temperature single-crystal experiments

The high-temperature single-crystal X-ray diffraction experiment, which were carried out at the University of Pavia, have been performed with two point detector diffractometer, a Philips PW1100 diffractometer operated by the software FEBO (control software developed locally) (Fig. 26a) and with a HUBER four-circle diffractometer automated by the SINGLE software (Angel and Finger 2011) (Fig.26b) for pyrope and grossular/uvarovite samples, respectively. Each instrument was equipped with a specifically designed micro-furnace controlled by an Eurotherm® temperature regulator. The crystals were mounted inside a thin quartz vial (0.3 mm inner diameter and 26 mm long, closed at the top by using oxy-methane flame) and were held in place by means of quartz wool. Because the maximum temperature reached during our experiments doesn't exceed 1500 K quartz-wool can be used to keep in

Fig. 26 – a) Philips PW1100 diffractometer at the University of Pavia equipped with the old design of the microfurnace and b) HUBER four-circle diffractometer at the University of Pavia equipped with the new design of the microfurnace. Both the diffractometers are equipped with a point detector.

position the samples in the vial. In order to avoid redox reactions of some samples with the environment buffers were loaded close to the crystals. The vial was mounted on a metal goniometer head on the diffractometer (Mo*Kα* radiation) operating at 50 kV and 30 mA. A micro-furnace was placed on top of the goniometer head. Diffraction data were collected up to T_{max} = 1073 K.

Microfurnace

So far five major types of heaters have been developed for single crystal high-temperature X-ray diffraction experiments: open flame, resistance-heated gas-flow, combustion-heated gas flow, radiative, and laser. Among these five different heaters

the choice of the device for in-situ diffraction experiments depends on the range of temperature that has to be reached and other environmental parameters. However, the devices used for high-temperature experiments have to satisfy some general requirements:

(1) it is fundamental to provide a stable and controlled isothermal environment for the entire sample, reducing the thermal gradient across the sample, which may lead to variation of the measured properties;

(2) sample has to be kept as much stable as possible on its position. The movement of the sample during the experiment will affect the quality of the measurement;

(3) the gaseous environment in the furnace has to be controlled. Some of the reasons are that the sample could overcome some redox reactions and at high temperatures the heating elements may require a vacuum or inert atmosphere;

(4) it has to access as much of the diffracted intensity as possible;

(5) it has to be easy to use.

All in-situ high-temperature X-ray diffraction experiments here presented have been carried-out by means of a radiative heater microfurnace. Below about 1400 K, radiative furnaces have generally been used because their simple design allows them to be built and handled easily (Hazen & Finger 1982).

The microfurnace used with the Philips PW1100 consisted of an H-shaped Pt-Rh resistance and a Pt/Pt-Rh thermocouple inside a steel cylindrical cage 1 inch wide closed with a Kapton film (Fig. 27). This device allows collecting diffraction data up to 2θ max ≈ 30°. Due to the low thermal conductivity of quartz and the distance between the

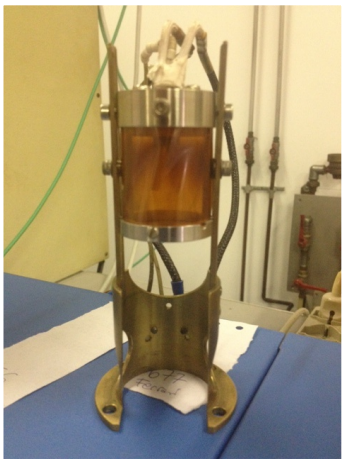

Fig. 27 – Old design of the microfurnace used with the Philips PW1100 consisted of an H-shaped Pt-Rh resistance and a Pt/Pt-Rh thermocouple inside a steel cylindrical cage 1 inch wide closed with a Kapton film.

thermocouple tip and the actual position of the crystal inside the quartz vial (ca. 1.5 mm), the reading of the controller is not the actual temperature of the crystal. To overcome this problem a temperature calibration of the microfurnace was undertaken using the known melting point of eight selected pure salts and measuring the thermal expansion of a spherical crystal of quartz across the α-β phase transition. Linear fitting performed on the observed melting points and on the observed transition temperature for the α–β quartz phase transition with the recorded temperature at the controller display yielded the following equation:

$$T\,(^{\circ}\mathrm{C}) = 8.818(4.684) + 1.154(10) \times T_{\mathrm{display}} \qquad (1)$$

While changing goniometer position the Temperature stability guaranteed with this device was typically within a few K. For further details on microfurnace calibration, see Càmara et al. (2012).

The furnace used with the Huber diffractometer is a newly designed H-shaped resistence heater developed starting from the design of the Philips one (see above). The greatest improvement on the micro furnace performances have been made firstly reducing the sizes of the metal structure, thus allowing for a much larger accessibility to the reciprocal space (i.e. up to about 70° in 2θ). Moreover, using a highly insulating machinable ceramic material such as Maccor© allowed to further reduce heat dispersion because of the insulation capability and the reduction of the bottom and top holes sizes, thus sensibly reducing the chimney effects. Lastly, a water cooling system has been added in order to allow reaching higher temperatures without compromising the diffractometer ϕ cunterbearing arm. Such cooling system improved sensibly the performances either in terms of thermal stability to better than 1K upon χ movements of about 45° and in terms of thermal gradients which resulted to be less than 5 K upon vertical movement of about 100 μm. For details of the furnace design and materials please refer to Figure 28 and Alvaro et al (2015, in prep).

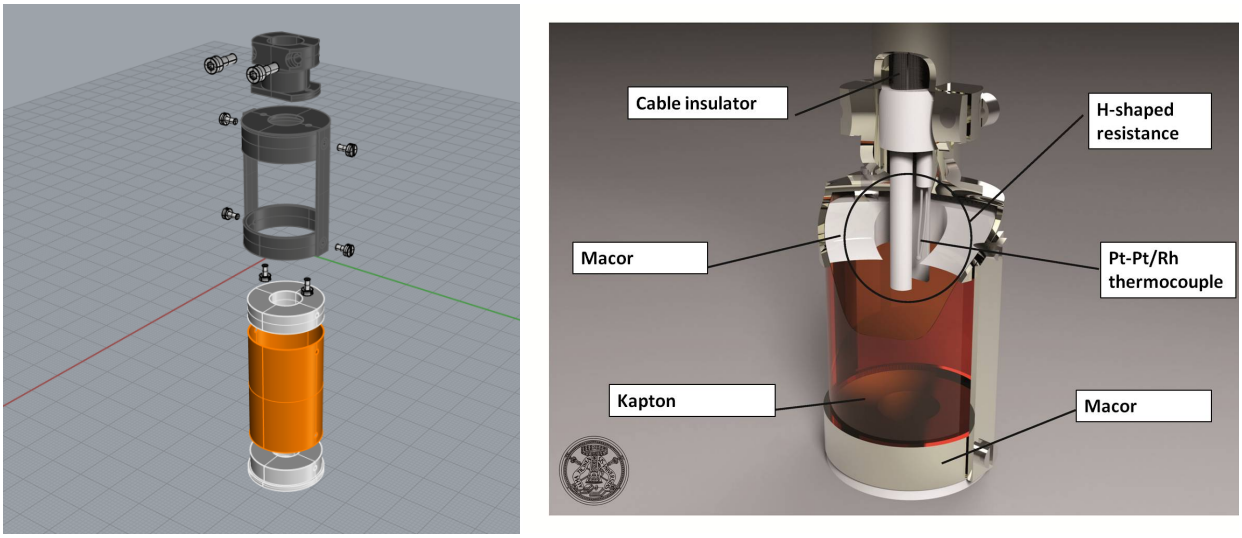

Fig. 28 – The newly designed H-shaped resistence heaters developed starting from the design of the Philips one (see above) (after Alvaro et al. in prep).

MANUSCRIPT 1

DIAMOND-GARNET GEOBAROMETRY: THE ROLE OF GARNET COMPRESSIBILITY AND EXPANSIVITY

Milani S.[a], Nestola F.[a*], Alvaro M.[a], Pasqual D.[a], Mazzucchelli M.L.[b], Domeneghetti M.C.[b], and Geiger C.A.[c]

[a] Dipartimento di Geoscienze, Università degli Studi di Padova, Via Gradenigo 6, I-35131 Padova, Italy

[b] Dipartimento di Scienze della Terra e dell'Ambiente, Università di Pavia, via Ferrata 1, I-27100 Pavia, Italy

[c] Fachbereich Materialforschung und Physik, Abteilung Mineralogie, Universität Salzburg, Hellbrunnerstrasse 34, A-5020 Salzburg, Austria

* Corresponding author e-mail: sula.milani@studenti.unipd.it

Abstract

The *P-V* and *T-V* Equation of State (EoS) of end-member pyrope (Py, $Mg_3Al_2Si_3O_{12}$) and the *P-V* EoS of end-member almandine (Alm, $Fe_3Al_2Si_3O_{12}$) as well as an intermediate garnet composition ($[Mg_{1.8}Fe_{1.2}]Al_2Si_3O_{12}$) were measured by *in-situ* high-pressure and high-temperature X-ray single-crystal diffraction experiments. The unit-cell volume of Py_{100}, Alm_{100}, and $Py_{60}Alm_{40}$ was measured at room temperature and high pressures up to about 8 GPa in a diamond-anvil cell. The high-temperature experiment was carried out using a micro-furnace from 293 K to 1073 K. The pressure-volume data were fitted to a third-order Birch-Murnaghan EoS giving the following coefficients: V_0 = 1506.15(16) Å^3, K_{T0} = 163.7(1.7) GPa and K' = 6.4(4) for pyrope, V_0 = 1533.52(10) Å^3, K_{T0} = 172.6(1.5) GPa and K' = 5.8(5) for almandine and V_0 = 1516.32(13) Å^3, K_{T0} = 167.2(1.7) GPa and K' = 5.6(5) for the intermediate $Py_{60}Alm_{40}$ composition. The unit-cell volume changes linearly across the join. The value of the first pressure derivative is the same for all three garnets within uncertainty, with an average value of K' = 6.0(4). The thermal expansion parameters, using a Kroll-type EoS, with the Einstein temperature fixed to 320 K are $\alpha_{(303K,\ 1bar)}$ = 2.543(5)*10^{-5} K^{-1} and V_0 = 1504.64(4) Å^3. The determined thermoelastic parameters were used in a thermal-pressure-type EoS to calculate the entrapment pressures, P_e, of garnet inclusions in diamond at mantle temperatures. The calculated P_e of 5.8 GPa for T = 1500 K agrees with estimated pressure conditions at which diamond crystallizes in the upper mantle based on other approaches of diamond-garnet formation. The use of larger K_{T0} values (≈170 GPa) for pyrope, as given in the literature, yields a higher P_e of 6.8 GPa for T = 1500 K, which may be to too high for garnet inclusion conditions.

Keywords: Pyrope, Almandine, Garnet, Bulk modulus, Diamond, Entrapment pressure

1. Introduction

About 1% of the diamonds (i.e. 10,897), originating from South Africa and Botswana, have mineral phases entrapped as inclusions from the 1,098,200 extracted between 1975 and 1985 (Stachel and Harris, 2008). Although inclusion-bearing diamonds are rare, they are geologically important, because they provide direct and unaltered samples from Earth's mantle. A determination of their pressure of formation (i.e. depth of provenance) can be used to constrain and understand the physico-chemical environment in which they formed. The pressure of formation can be estimated by two different methods. The traditional method is based on the cation partitioning between mantle minerals. However, this method can only be applied to rare cases, that is, when the appropriate mineral assemblage is present in the same inclusion [e.g. orthopyroxene and garnet (Nickel and Green, 1985), clinopyroxene (Nimis and Taylor, 2000)]. An alternative method has been developed (e.g. Rosenfeld and Chase, 1961; Zhang, 1998; Angel et al., 2014a, 2014b). It is based on a determination of the residual pressure of an inclusion, P_{inc}, still trapped in diamond at room temperature and pressure (i.e. ambient conditions). This residual pressure arises from the different elastic properties (expansivity and compressibility) between the diamond host and the inclusion, regardless of the *P*-*T*-*t* path taken during the exhumation. This method can potentially be applied to any single mineral inclusion, but it requires accurate knowledge of the thermoelastic parameters of the diamond host and inclusion and a precise determination of P_{inc}.

One is, moreover, interested in calculating the entrapment pressure, P_e, of a given inclusion (i.e. at the conditions of formation). Garnet and olivine are the most abundant minerals found as inclusions in diamonds. The thermoelastic parameters of diamond are determined to a precision that yields insignificant uncertainties in P_e

(Angel et al., 2014a), but the thermoelastic parameters of garnet are not known as well. More than 60% of garnet inclusions are peridotitic in nature, and are composed of more than 90% pyrope and almandine components, with minor grossular, uvarovite, and andradite (Stachel and Harris, 2008). However, published *P*-*V* and *T*-*V* Equations of State (EoS) of pyrope-almandine garnets are different. Geiger (1999) reviewed and analyzed the *P*-*V* and *T*-*V* behavior of end-member aluminosilicate garnets, based on published experimental results, including pyrope and almandine. Since then, a number of computational studies on the *P*-*V* and *T*-*V* behavior of pyrope and almandine, as well as more experimental results, have been published. Variations in the published data yield considerable differences in calculated entrapment pressures. Therefore, in order to avoid inconsistency issues arising from the use of different datasets, we measured the *P*-*V* EoS for three garnet compositions along the pyrope-almandine solid solution (i.e., Py_{100}, $Py_{60}Alm_{40,}$ and Alm_{100}) and the *T*-*V* EoS for synthetic end-member pyrope by *in-situ* high-pressure and high-temperature X-ray single-crystal diffraction, respectively. The former is done in a diamond anvil cell (DAC) and, here, we employ improved experimental methods that allow for a more accurate pressure description. The set of elastic coefficients obtained are, therefore, internally consistent and can be used to calculate the effect of compositional on elastic properties and, in turn, on the entrapment pressures of pyrope-almandine-rich garnet inclusions in diamond.

2. Methods

The garnets used in this study are synthetic single crystals of end-member pyrope, Py_{100}, end-member almandine, Alm_{100}, and a solid-solution composition, $Py_{60}Alm_{40}$. Their synthesis conditions are described in Geiger et al. (1991) and Armbruster et al. (1992). The crystals used for high-pressure experiments were ca.

80 x 30 x 30 μm, while the pyrope sample used for the high-temperature experiment was ca. 300 x 200 x 150 μm. The crystals were selected based on the absence of twinning and visible inclusions and on the quality of their diffraction peak profiles.

High-pressure single-crystal X-ray diffraction experiments were carried out with a STOE STADI-IV four-circle diffractometer (Mo*Kα* radiation) equipped with a point detector, operating at 50 kV and 40 mA, and automated by the software SINGLE (Angel and Finger, 2011). The samples were loaded in three different experimental runs in an ETH-type diamond-anvil cell (Miletich et al., 2000) using a steel gasket, pre-indented to 100 - 110 μm thickness and with a hole diameter of 230 - 250 μm. A pressure transmitting medium consisting of a 4:1 methanol:ethanol mixture was used, which remains hydrostatic up to about ~ 9.5 GPa (Angel et al., 2007). For each measurement, a single crystal of quartz was also loaded into the diamond-anvil cell for use as a pressure standard (Angel et al., 1997). The garnet unit-cell edge was determined by centering at least 27 reflections for each pressure measurement in the 2θ range of 14° to 29°. Any effects of crystal offsets and diffractometer aberrations were eliminated by using the eight-position centering method (King and Finger, 1979). The unconstrained unit-cell parameters, obtained by a vector least-squares fit (Ralph and Finger, 1982), always confirmed cubic symmetry within 1 e.s.d..

The high-temperature single-crystal X-ray diffraction experiment was performed with a Philips PW1100 diffractometer operated by the software FEBO (control software developed locally) and equipped with a micro-furnace, which is controlled by an Eurotherm temperature regulator. The pyrope crystal was mounted inside a thin quartz vial (0.3 mm inner diameter and 26 mm long) and was held in place by means of quartz wool. The vial was mounted on a metal goniometer head on the diffractometer (Mo*Kα* radiation) operating at 50 kV and 30 mA and equipped

with a 0.5 mm short collimator. A micro-furnace was placed on top of the goniometer head. The micro-furnace device and the temperature calibration procedure are described in Pandolfo et al. (2014). Diffraction data were collected up to θ_{max} = 34° and T_{max} = 1073 K.

The garnet unit-cell parameters were determined upon heating from 291 K to 1073 K at steps of 25 K and during cooling at steps of 50 K, in order to ensure the reproducibility of the data. At each temperature step, the unit-cell parameter was calculated by least-square fitting of a group of 60 selected reflections following the LAT procedure (see Pandolfo et al., 2014, for further details). The measured unit-cell parameters are listed in Supplementary Table A1. Diffraction peak profiles were collected at each temperature step on the same set of reflections to constantly monitor the quality of the crystal. The average FWHM value for the reflections, determined with WinIntegrStp (Angel, 2003), was 0.145(2)° even at high *T*, indicating no broadening of the peaks over the whole investigated *T* range.

3. Results and discussion

3.1 High-pressure behavior

The unit-cell edges and the unit-cell volumes for Py_{100}, Al_{100}, and $Py_{60}Al_{40,}$ at different pressures are reported in Supplementary Tables A2 to A4. The unit-cell volume of all samples decreases smoothly with increasing pressure, as shown in Fig. 1, up to the maximum hydrostatic pressure reached in this study of 7 to 8 GPa. This covers the range of pressure stability for upper mantle garnets. The *P*-*V* data were fitted using a third-order Birch-Murnaghan EoS (BM3-EoS, Birch, 1947), because F_E-f_E plots (Fig. 2) of the data can be fitted by straight lines with positive slopes (Angel, 2000). The BM3-EoS coefficients were refined simultaneously using the program EoS-FIT7c (Angel et al., 2014*c*) giving:

for **Py_{100}:** V_0 = 1506.15(16) Å^3, K_{T0} = 163.7(1.7) GPa and K_0' = 6.4(4) (ΔP_{max} = 0.039 GPa, χ^2_w = 1.1)

for **$Py_{60}Al_{40}$:** V_0 = 1516.32(13) Å^3, K_{T0} = 167.2(1.7) GPa and K_0' = 5.6(5) (ΔP_{max} = 0.060 GPa, χ^2_w = 1.2)

and

for **Al_{100}**: V_0 = 1533.52(10) Å^3, K_{T0} = 172.6(1.5) GPa and K_0' = 5.8(5) for **Al_{100}** (ΔP_{max} = 0.026 GPa, χ^2_w = 0.8).

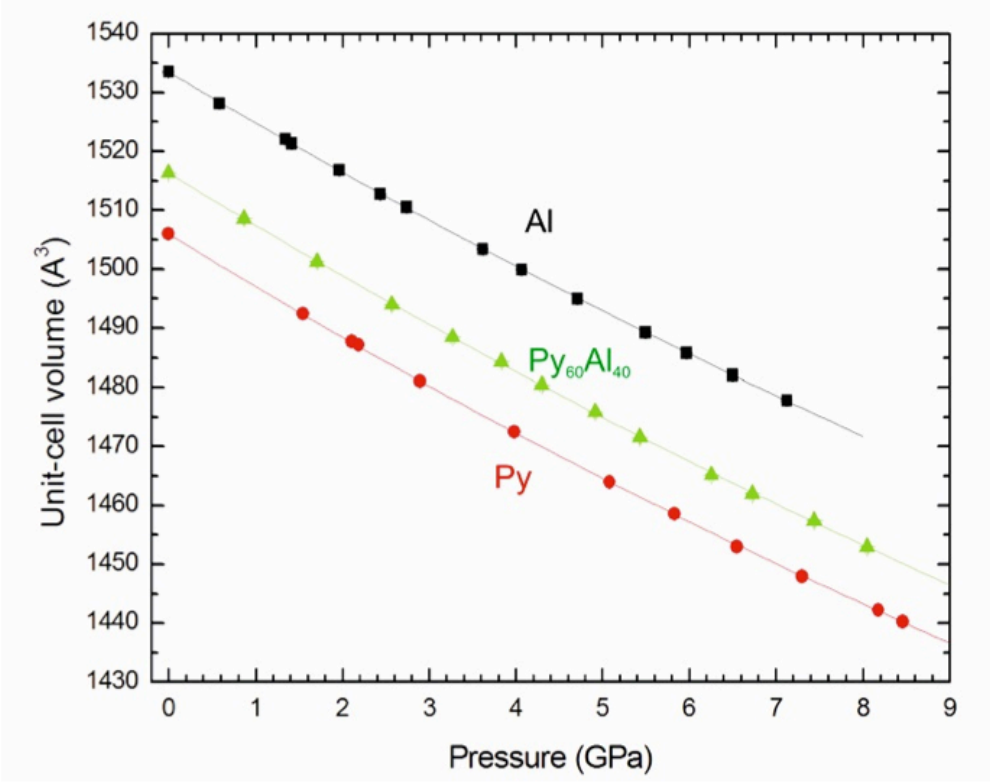

Figure 1. Pressure-volume behavior of end-member pyrope and almandine and the solid-solution composition $Py_{60}Al_{40}$. The solid lines are Birch-Murnaghan 3rd order EoS fits to the data. The error bars are smaller than the symbol size.

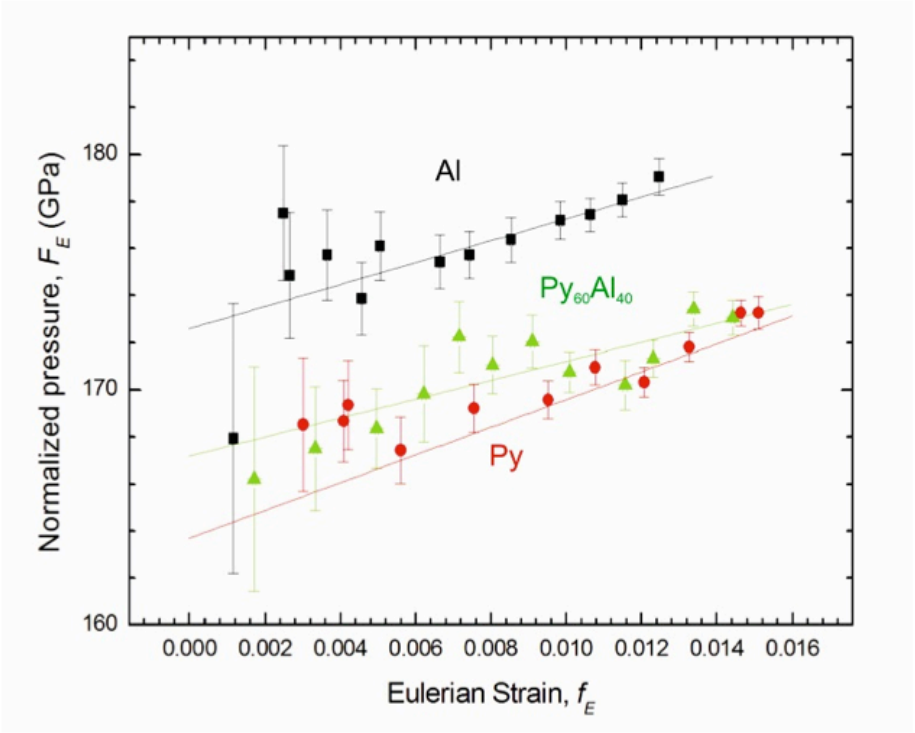

Figure 2. F_E-f_E plot for end-member pyrope and almandine and the solid solution composition $Py_{60}Al_{40}$. The solid lines are a Birch-Murnaghan 3rd order EoS fits to the data.

The ΔP_{max} and χ^2_w values indicate that all three EoS provide good fits to the data. The room pressure volume, V_0, and isothermal bulk modulus, K_{T0}, are a function of the Py content of the garnet (Fig. 3). An increase in almandine content causes a small increase in the molar volume because of the larger Fe^{2+} cation radius compared to that of Mg (Geiger and Feenstra, 1997; Skinner, 1956). The variation of the room-*P* volume data as a function of composition can be expressed as:

$$V_0\ (Å^3) = 1533.4(4) - 0.277(8)\cdot Py\ (mol\ \%).$$

Geiger (1999) gave a best estimate for the unit-cell volume of end-member almandine of 1530.81 $Å^3$ and 1503.21 $Å^3$ for pyrope. Garnet volumes can be slightly increased by the presence of small amounts of octahedral Fe^{3+} in almandine and

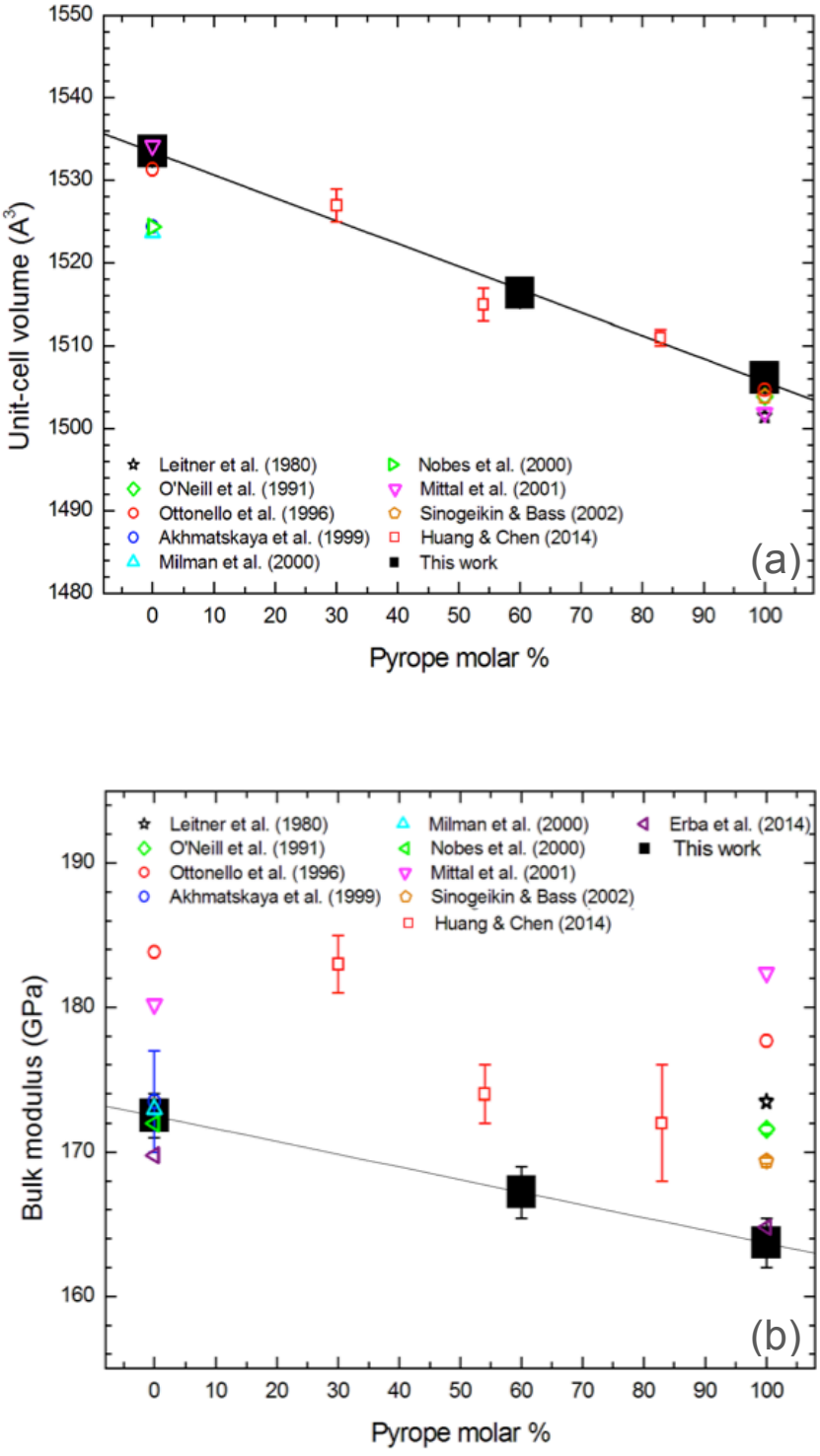

Figure 3. Unit-cell volume (a) and bulk modulus (b) values across the almandine-pyrope join showing linear behavior as a function of composition. The isothermal bulk moduli are for 298 K.

structural OH^- ("hydro-garnet substitution")in both garnets. The volume behavior across the Al-Py binary (Fig. 3(a)) is nearly linear (there are only small positive deviations from volumetric ideality – Geiger and Feenstra, 1997). The variation in bulk modulus (Fig. 3(b)) is also linear (e.g. Yeganeh-Haeri et al., 1990; Duffy and Anderson, 1989; Isaak and Graham, 1976) and reflects the compression ideality of the Py-Al solid solution. The room-*P* unit-cell volume of pyrope is smaller by about 27.7 $Å^3$ (i.e. 1.8%) than that of almandine. The bulk moduli of the two garnet end members differ by 5.1% with almandine being stiffer with K_{T0} = 172.6(1.5) GPa than pyrope with K_{T0} = 163.7(1.7) GPa. An increase in K_{T0} with increasing almandine component in garnet is confirmed by the K_{T0} value of 167.2(1.7) GPa with K_0' = 6(5) for the solid solution $Py_{60}Al_{40}$. The first pressure derivative, K_0', is the same for all garnets with a value of 6.0(4).

The bulk modulus of both pyrope and almandine have been determined by different experimental and computational methods (e.g. Brillouin spectroscopy, static compression experiments in both the diamond anvil cell and various large solid-media devices, ab-initio and other types of calculations) a number of times. Bulk moduli obtained with the Brillouin technique are adiabatic, giving K_S. Therefore, for the purpose of comparison, K_S needs to be converted to K_{T0} by applying the relationship $K_S = K_{T0}(1 + \alpha\gamma T)$, where α is the thermal expansion, γ the Grüneisen parameter, and T the temperature. Static DFT calculations provide K_{T0} at 0 K. Our high temperature diffraction data and published low temperature data for pyrope (Bosenick and Geiger, 1997) and almandine (Skinner, 1956) can be combined to describe their thermal expansion behavior. An analysis shows that the bulk modulus for pyrope decreases by ~5 GPa and that for almandine by ~3 GPa from 0 K to room temperature at ambient pressure. We have, therefore, adjusted the K_{T0} values from DFT calculations to room temperature conditions by -5 GPa for pyrope and -3 GPa

for almandine.

Our value for K_{T0} of pyrope is at the lower end of the range of published values (Fig. 3(b) and Supplementary Table A5), but it agrees with a recent DFT calculated value (Erba et al., 2014). The same is true for the case for the K_{T0} value of almandine (Fig. 3(b) and Supplementary Table A6). The largest differences in pyrope and almandine bulk modulus values are with the lattice dynamical calculation results of Mittal et al. (2001).

3.2 A critical analysis of published experimental and computational studies on the compression behavior of pyrope and almandine

In order to calculate the true pressure of entrapment, P_e, for a diamond-inclusion pair, it is crucial to have accurate and precise thermoelastic parameters for both phases. We analyze, here, in short form a number of bulk-modulus investigations made on end-member pyrope and almandine in the literature. The experimental set-ups and conditions and the computational methods, along with their results, are summarized in Supplementary Tables A5 and A6. The work of Huang and Chen (2014) presents an equation of state for binary Py-Alm solid solutions, but we decided not to consider this work in detail, because their measurements were made using silicon oil as the pressure-transmitting medium. Silicon oil does not ensure hydrostatic conditions at pressures above 2 GPa (Angel et al., 2007). Given that they measured the volume compression to pressures above 15 GPa, their data are probably affected by nonhydrostatic conditions.

3.2.1 Pyrope

We consider 23 papers, starting from 1970, relating to a determination of the bulk modulus of pyrope. We did not review results published before 1970, because

experimental high-pressure techniques were not as precise as those of more recent studies. We give a short summary of the various works and, from them, we selected certain K_{T0} results for use in calculating P_e of diamond-garnet pairs later in this paper.

In general, many experimental studies suffer from experimental problems relating to the presence of non-hydrostatic conditions at high-pressure. This is a serious issue and an on-going challenge to the experimenter even today. The early work of Takahashi and Liu (1970) and the early diamond anvil cell studies of Hazen and Finger (1978) and Leger et al. (1990) are probably affected by non-hydrostatic conditions. The low value of the bulk modulus (i.e. K_{T0} = 133 GPa) for pyrope in the former DAC study indicates technical problems. The results of Sato et al. (1978), Chen et al. (1999), Sinogeikin and Bass (2000), Zou et al. (2012), and Gwanmesia et al. (2006, 2007) may also be plagued by nonhydrostatic conditions in their respective experimental set-ups at elevated pressures. Thus, we do not consider their results in our calculations later on in the paper.

The bulk modulus determination of Levien et al. (1979), using a diamond anvil cell, is based on only five pressure measurements to a maximum P of 4.96 GPa. Thus, we do not consider their K_{T0} =175 (1) GPa value further (For a precise equation of state determination, three parameters must be refined (V_0, K_{T0}, K') and, thus, 5 data points is too small to allow robust least-squares fitting. In addition, for a stiff structure like garnet the maximum pressure achieved is probably too low to describe any possible volume curvature). The technically advanced DAC study of Zhang et al. (1998) made to very high pressures of 33 GPa deserves special consideration. They used helium, neon and a mixture of both as a pressure-transmitting medium. Helium is better in terms of hydrostaticity and they reported a K_{T0} value of 171(2) GPa for this case. However, in fitting their results, the unit-cell volume at room pressure was not used and the data were not weighted. Using their published volume-pressure data,

one calculates, using their V_0 value and weighting the data, K_{T0} = 178(1.6) GPa and K' = 3.7(2). Alternatively, if V_0 is included in the calculation, but the data are not weighted, one obtains K_{T0} = 165.8(4.5) GPa and K' = 4.7(3). Due to the resultant uncertainty, we do not consider these results further.

We kept the bulk modulus value of 173.5(1) GPa of Leitner et al. (1980) and 171.6(3) GPa of O'Neill et al. (1991), although they did not perform measurements at high pressure and thus no K' value is reported. Both are Brillouin scattering based values. Ottonello et al. (1996) calculated the bulk modulus and first pressure derivative values using empirical pair potentials and we decided to accept their results. We did not keep the ab-initio computational results of Akhmatskaya et al. (1999), where K_{T0} = 170 GPa, because their calculated unit-cell volume at 0 K appears too low based on experimental measurements at 20 K (Bosenick and Geiger, 1997). A similar problem appears to be the case with the calculations of Milman et al. (2000). We used the results from the computational work of Mittal et al. (2001), where K_{T0} = 182.4 GPa and the experimental Brillouin scattering results of Sinogeikin and Bass (2002) who give K_{T0} = 169.4(2) GPa. Finally, we kept the most recent ab-intio-based results of Erba et al. (2014), where K_{T0} = 164.8 GPa.

3.2.2 Almandine

There are 11 different studies concerning the pressure behavior of almandine, as summarized in Supplementary Table A6. As in the case of pyrope, we think the K_{T0} value of 175(7) GPa of Sato et al. (1978) may be affected by nonhydrostatic conditions in their experiments. Yagi et al. (1987) presented different K_{T0} values from 168 to 176 GPa and, thus, we did not consider their results further. The calculated bulk modulus of 183.833 GPa from Ottonello et al. (1996) is accepted as is. We do not take into account the bulk modulus value of 185(3) GPa of Zhang et al. (1999) for

similar reasons as for the case with pyrope. We use, further, the ab-initio-based results of Akhmatskaya et al. (1999), Nobes et al. (2000) and Milman et al. (2000), as well as the computational lattice dynamic values of Mittal et al. (2001) and the recent ab-initio results of Erba et al. (2014), although they do not calculate *K*'.

3.2.3 Summary

For calculating P_e of garnet inclusions in diamond (below), we selected the results on pyrope of Leitner et al. (1980), O'Neill et al. (1991), Ottonello et al. (1996), Mittal et al. (2001), Sinogeikin and Bass (2002), and Erba et al. (2014). The studies give an average K_{T0} value of 173.2 GPa. Only Ottonello et al. (1996) gives *K*' with a value of 5.7. In the case of almandine, we selected the results of Ottonello et al. (1996), Akhmatskaya et al. (1999), Nobes et al. (2000), Milman et al. (2000), Mittal et al. (2001), and Erba et al. (2014). They give an average K_{T0} value of 175.4 GPa. Four studies give *K*', which, when averaged, is equal to 4.3.

Following this, it is clear that we determined in this investigation notably lower values for K_{T0} for both pyrope with K_{T0} = 163.7(1.7) GPa and almandine with K_{T0} = 172.6(1.5) GPa and slightly higher *K*' values. In general, agreement is better for almandine than for pyrope. Because peridotitic garnets included in diamonds are richest in pyrope, we focus our further analysis on the various values for K_{T0} and *K*' and their effect on calculated P_e.

3.3 High-temperature behavior

The unit-cell volume of pyrope increases almost linearly with increasing temperature up to the maximum temperature of measurement of 1073 K. The measurements during heating and cooling agree within 1 standard deviation,

demonstrating that no irreversible change in the crystal occurred, thus indicating good experimental reproducibility (Fig. 4 and Supplementary Table A1).

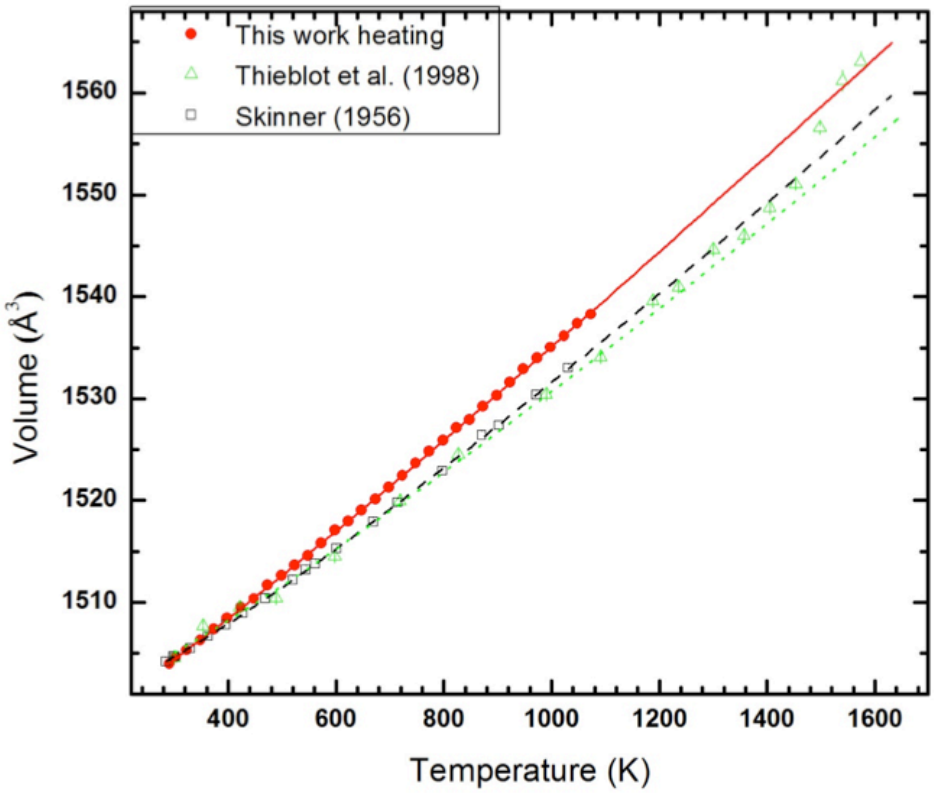

Figure 4. Temperature-volume data for pure pyrope compared with literature data from Skinner (1956) and Thieblot et al. (1998). The solid, dashed, and dotted lines are the Fei-type EoS fit to the data. The error bars are smalle than symbol size.

The temperature-volume data were fitted using the software EoSFit7c (Angel et al., 2014c) to a Fei-type EoS (Fei, 1995). The thermal expansion coefficients obtained are: a_0 = 3.01(19) 10^{-5} K^{-1}, a_1 = 5(20)·10^{-10} K^{-2}, and a_2 = -0.5(2) K, with V_0 = 1504.63(8) at 300 K. This gives a value for $\alpha_{(300K,\ 1bar)}$ of 2.5(2)·10^{-5} K^{-1} (Fig. 4 and Table 1(a)). A comparison of calculated unit-cell volumes, using the fitted coefficients, and the experimentally measured unit-cell volumes in the high temperature regime [see Pandolfo et al., 2014 for a discussion of δV and statistical parameters from the fitting,] confirm that the model equation provides a good fit over the whole temperature range.

Table 1a. Volume of pyrope at 303 K and 1073 K and thermal expansion behavior given by Fei-type and Kroll-type EoS.

$V_{303\,K}$ calculated (Å^3)	$V_{1073\,K}$ calculated (Å^3)	$\alpha_{303\,K}$ x10^{-5} (K^{-1})	a_0 x10^5 (K^{-1})	a_1 x10^{10} (K^{-2})	a_2 (K)	EoS formalism	Reference
1504.6(1)	1538.5(2.3)	2.5(2)	3.01(19)	5(20)	-0.5(2)		This work
1504.8(4)	1534.8(9.3)	2.0(8)	2.3(8)	60(80)	-0.4(7)	Fei-type[3]	Skinner (1956)[1]
1505.2(9)	1534.1(7.5)	1.7(6)	2.5(6)	30(50)	-0.9(10)		Thieblot et al. (1998)[2]
1504.64(4)	1538.86(6)	2.543(5)					This work
1504.6(1)	1534.6(2)	2.25(2)				Kroll-type	Skinner (1956)[1]
1504.4(3)	1534.1(1)	2.24(2)					Thieblot et al. (1998)[2]

Note: [1]data have been fitted to the entire range of temperature (284K-1031K); [2]data have been fitted to the range of temperature between 300K-1453K. [3]Fei-type coefficients reported are calculated using as T_{ref} the first experimental temperature collected for each data sets.

Table 1b. Room pressure-temperature Equations of State coefficients obtained with a BM3- and thermal-*P* type-EoS for end-member pyrope and almandine.

	K_{T0} (GPa)	K'	α_{303}x10^{-5} (K^{-1})	θ_E (K)	Reference
Py	163.7	6.4	2.543(5)	320	This work
Alm[1]	172.6	5.8	1.85(1)	600	Skinner (1956)

Note: [1]Data of Skinner (1956) and Armbruster et al. (1992); [2] Data of Skinner (1956) and Bosenick and Geiger (1997); [3]Fei-type coefficients are those of Zou et al. (2012), where T_{ref} is the first experimental temperature collected, with the α_2 = 0 fixed during refinement and $\partial K/\partial T$ fixed to -0.021 GPa/K.

Previous high-temperature volume measurements on an end-member synthetic pyrope and a natural pyrope-rich garnet from Dora Maira, Italy, were performed by means of powder X-ray diffraction by Skinner (1956) and by Thieblot et al. (1998), respectively. In order to facilitate comparison to our results, these literature data were also fitted using the Fei-type EoS (Fig. 4 and Table 1(a)). The data of Skinner (1956) were fit over the temperature range from 284 K to 1031 K, and those from Thieblot et al. (1998) from 300 K to 1453 K. All fitting results are reported in Table 1(a) and shown Fig. 4. As indicated in Table 1(a), there are small differences between our data and those from the literature. The thermal expansion coefficients at 300 K obtained from both the Skinner (1956) and Thieblot et al. (1998) data are smaller than those calculated from our fits. Differences between our data and those of Skinner (1956) are probably caused by differences in experimental methods. The lowest e.s.d.s given for the a_0 determinations of Skinner (1956) is 0.001 Å, which is 10 times greater than that from our measurements. This leads to larger uncertainties for the thermal expansion coefficient for the former. The larger differences between our data and those of Thieblot et al. (1998) can possibly be ascribed to both differences in the experimental technique used (i.e. powder diffraction vs. single-crystal diffraction) and to compositional differences in the garnets. Their natural pyrope contains some Ca and Fe (see Table 1 in Thieblot et al., 1998).

Our high T diffraction data for Py_{100} and the low-T diffraction data of Bosenick and Geiger (1997 - not using the more scattered data at 195, 220 and 295 K) can be combined into a single data set from 20 K to 1073 K (Fig. 5). These combined data were fit with a Kroll-type EoS (Kroll et al., 2012). The Kroll-type EoS gives a good description of the thermal expansion behavior for pyrope over a large temperature range and it is needed to make calculations of P_e for diamond-garnet pairs (see

below). The same procedure was done for end-member almandine by combining the high-*T* data set of Skinner (1956) with that of Armbruster et al. (1992) in the low-temperature regime from 100 to 293 K (Fig. 5).

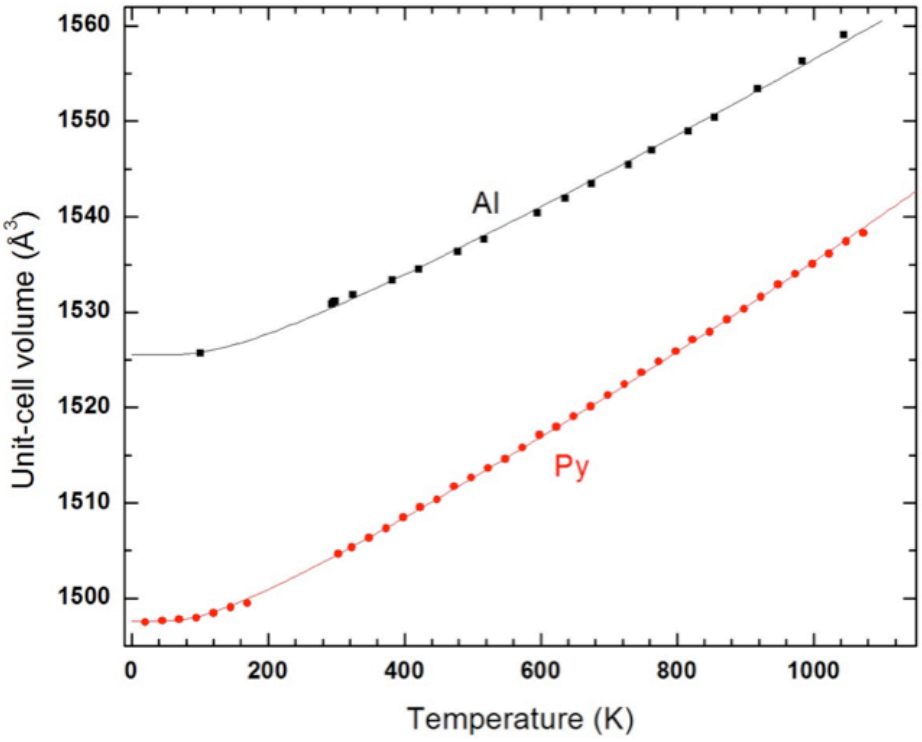

Figure 5. Volume data against temperature for pure pyrope and pure almandine resulting from the combination of the low-*T* data (Bosenick and Geiger, 1997 for pyrope and Armbruster et al., 1992 for pure almandine) with those at high-*T* (this work for pure pyrope and Skinner, 1956 for almandine).

Einstein temperatures, θ_E, of 320 K for Py and 600 K for Alm were used and they provide a reliable fit of the data, describing well the low-*T* behavior (i.e. below 300 K) for both end members. The reliability of both Einstein temperatures was further confirmed by a consideration of the saturation temperature behavior. The value of T_{sat} is about one half of that of θ_E, with 170 K for pyrope and 250 K for almandine, as obtained from fitting just the low-*T* data set using a Salje-type EoS (Salje et al., 1991). The fitting results obtained with the Kroll-type EoS (Kroll et al., 2012) are reported in Table 1(a).

4. Application to diamond geobarometry

Most garnets inclusions in diamond have an average pyrope component of ca. 84 mol % and 11 mol % almandine if the diamond is of harzburgitic origin and ca. 73 mol % and ca. 13 mol % almandine if the diamond is of lherzolitic origin (Stachel and Harris, 2008). Therefore, it is reasonable to expect that the compressibility behavior of pyrope-almandine garnets will have the largest effect on calculated entrapment pressures, P_e, in diamond. Thus, we model the P_e behavior of pyrope-almandine solid solutions included in diamond, and we analyze the effect of composition and the experimental uncertainty of the measured elastic parameters on calculated P_e values.

P_e can be considered as the pressure of formation of the diamond-garnet pair, when both are syngenetic in origin. The calculation of P_e is based on the assumption that, at the time of formation of the diamond-inclusion pair, the mineral inclusion and the void in the diamond host have the same volume when both are at the same P and T conditions (Angel et al., 2014*a* and references therein). When such a closed system is brought to ambient P-T conditions, the host will apply a residual pressure, P_{inc}, on the included phase, due to their different elastic properties. In our case, here, the stiffer diamond host will expand less than the softer garnet inclusion. The possible entrapment conditions for such a system can be described in P-T space by an isomeke line (Adams et al., 1975). This line defines the conditions at which the host and the inclusion have the same P, T and volume. For our P_e calculations, we assume a residual pressure on garnet of 0.5 GPa (e.g. Nestola et al., 2012) and we use the EoS for diamond given in Angel et al. (2014a). Furthermore, we use the thermal-pressure model of Holland and Powell (2011) taking our pressure-volume equation of state coefficients for pyrope and almandine and our volume thermal expansion coefficients for pyrope. This approach avoids the need to determine the variation of the bulk modulus with temperature, $\partial K/\partial T$. The final full set of EoS

coefficients that are obtained from the calculations are reported in Table 1(b).

The uncertainties in our measured garnet bulk modulus values and their first pressure derivative values, and their negative correlation, lead to an uncertainty in the isomeke pressure at room *T* of 0.008 GPa for pyrope and 0.007 GPa for almandine. These uncertainties are smaller than those arising from the pressure measurements on the recovered inclusion (P_{inc}). The values of 0.008 and 0.007 GPa for pyrope and almandine, respectively, can become larger at higher temperature at e.g. 1500 K - a temperature reported for lithospheric diamonds (Stachel and Harris, 2008) - with values of 0.13 GPa and 0.18 GPa for almandine and pyrope, respectively. In the case of a hypothetical end-member almandine crystal entrapped in diamond the entrapment pressures would be 16% lower than those for an end-member pyrope inclusion. This agrees with the respective stiffness of the two end-member garnets.

The variation in the different published elastic parameter values (Tables 2a and 2b) leads to differences in isomeke pressures of less than 0.02 GPa at room *T*. This is roughly the same as those uncertainties arising from a determination of the pressure, P_{inc}, on the inclusion. At higher temperatures, at e.g. 1500 K, once again, for the hypothetical case of an end-member almandine inclusion in diamond, differences in elastic properties give rise to variations in calculated entrapment pressures of up to 0.3 GPa. This corresponds to differences of about 10 km in depth. For the sake of comparison, variations in thermal expansion behavior for literature results lead to larger differences in calculated P_e values of ca. 3 GPa. An analogous calculation for the case of end-member pyrope included in diamond gives greater differences of up to about 0.6 GPa, corresponding to a difference in depth of formation of about 20 km. Larger differences in the isomeke lines of pyrope and almandine are observed up to about 1 GPa. They are six times greater than those

Table 2a. Entrapment pressures, P_e, for a hypothetical end-member pyrope inclusion trapped in diamond (P_{inc} = 0.50) calculated using various bulk modulus values from the literature.

K_{T0} for pyrope	Leitner et al., 1980	O'Neill et al., 1991	Ottonello et al., 1996	Mittal et al., 2001	Sinogeikin and Bass, 2002	Erba et al., 2014	This work
Temperature (K)							
300	0.827	0.821	0.844	0.805	0.815	0.816	0.802
1100	4.772	4.756	4.952	5.094	4.607	4.623	4.402
1200	5.171	5.154	5.367	5.524	4.992	5.009	4.766
1300	5.564	5.543	5.773	5.946	5.369	5.388	5.123
1400	5.950	5.927	6.174	6.362	5.74	5.761	5.474
1500	6.331	6.305	6.570	6.772	6.107	6.128	5.821
1600	6.708	6.679	6.960	7.177	6.469	6.492	6.164
1700	7.081	7.05	7.348	7.578	6.828	6.852	6.504
1800	7.452	7.418	7.733	7.977	7.184	7.210	6.842

Table 2b. Entrapment pressures, P_e, calculated for a hypothetical end-member almandine inclusion trapped in diamond (P_{inc} = 0.50) using various bulk modulus values from the literature.

K_{T0} for almandine	Ottonello et al., 1996	Akhmatskaya et al., 1999	Nobes et al., 2000	Milman et al., 2000	Mittal et al., 2001	Erba et al., 2014	This work
Temperature (K)							
300	0.864	0.827	0.821	0.826	0.848	0.825	0.827
1100	4.226	3.877	3.829	3.861	3.987	3.752	3.840
1200	4.575	4.195	4.142	4.178	4.311	4.054	4.154
1300	4.918	4.506	4.450	4.487	4.628	4.349	4.460
1400	5.255	4.813	4.753	4.793	4.941	4.640	4.763
1500	5.588	5.116	5.052	5.095	5.249	4.927	5.062
1600	5.918	5.416	5.347	5.392	5.553	5.211	5.358
1700	6.245	5.712	5.640	5.688	5.854	5.492	5.651
1800	6.570	6.007	5.929	5.981	6.154	5.770	5.942

Note: the *P*-EoS coefficient used for the P_e calculations are those reported in Supplementary Table, whereas the *T*-EoS are in those in Table 1(b).

associated with our uncertainties in the EoS parameters for pyrope and almandine.

An analysis of the differences in the calculated entrapment pressures, arising from both the uncertainties in the EoS parameters and variations in their values, demonstrate that our methodology should be precise enough to provide estimates of P_e with uncertainties smaller than 0.2 GPa. However, considering the variations in published garnet elastic properties, it is not possible to obtain accuracy for P_e of better than 0.6 GPa. We can determine the minimum entrapment pressures for inclusion of Py-Al garnets, with uncertainties less than 3% (Fig. 6), because differences in P_e related to experimental uncertainties are much smaller than those caused by variations in garnet composition using our method. Figure 6 shows the effect of pyrope's elastic behavior on P_e calculated for the solid-solution garnet $Py_{60}Al_{40}$. We think it is possible to calculate the P_e for any Py-Al garnet in diamond, provided that the diamond and the garnet have not undergone any brittle or plastic deformation.

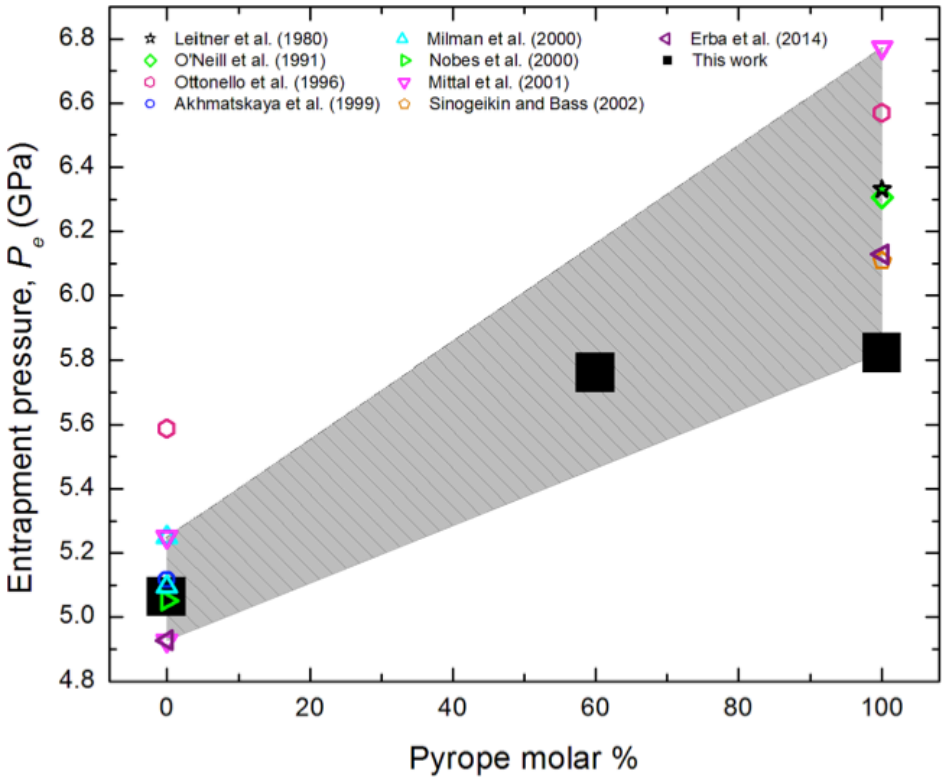

Figure 6. Entrapment pressures, P_e, calculated for any given Al-Py garnet inclusion in diamond assuming P_{inc} = 0.5 GPa and 1500 K, where the latter is the average temperature reported for lithospheric diamonds (Stachel and Harris, 2008).

4.1 Relationship between calculated entrapment pressures and mantle palaeogeotherms

Pressures calculated using the compression behavior for end-member pyrope inclusions in diamond (Table 2(a)) could provide a good model for natural garnets, as diamonds are usually pyrope-rich. We consider, therefore, calculated P_e values and the conditions at which diamond formation is thought to occur in the mantle for a model pyrope inclusion. We obtain P_e = 5.82 GPa at T=1500 K assuming a residual pressure of 0.5 GPa and our measured K_{T0} = 163.7 GPa for pyrope. Calculated P_e values are higher, ranging from 5.84 to 6.77 GPa (Fig. 6 and Table 2(a)) using the various bulk modulus values from the literature. We obtain P_e = 6.32 GPa using the averaged bulk modulus value from our selected literature data set where K_{T0} = 173.2 and K' = 5.7.

We can calculate, furthermore, P_e at which pyrope can be trapped in diamond at a fixed temperature, if the diamond-pyrope pair formation is assumed to occur under steady state geothermal conditions of the cratonic lithosphere. Based on the recent thermal modeling of palaeogeotherms (Ziberna et al., submitted; Mather et al., 2011; McKenzie et al., 2005), a P_e of 5.2 (2) GPa is calculated for 1500 K for warm cratonic mantle (e.g. Premier and Finsh mines of the Kaapvaal craton) and 5.9 (3) GPa for a relatively cooler mantle section (e.g. Novinka and Udachnaya of the Siberian craton). P_e for a fixed temperature will be even lower, if diamond formation would be associated with a thermal perturbation event, where the temperature would be higher than that for steady state conditions. The calculated P_e value of 5.8 GPa at T = 1500 K, obtained using the thermoelastic parameters in this work appears reasonable and more realistic compared to P_e = 6.8 GPa at T = 1500 K obtained with literature results. Our results appear to better agree with pressure-temperature conditions at which diamond forms in the upper mantle (see Shirey et al. 2013 for a review).

Acknowledgments

This work has been supported by the ERC Starting Grant (number 307322) to F. Nestola and the Austrian Science Fund (FWF, P 25597-N20) to C.A. Geiger. We thank R.J. Angel, P. Nimis, and L. Ziberna for fruitful discussions.

References

Adams, H.G., Cohen, L.H. and Rosenfeld, J.L., 1975. Solid inclusion piezothermometry I: comparison dilatometry. American Mineralogist 60, 574-583.

Akhmatskaya, E.V., Nobes, R.H., Milman, V., Winkler, B., 1999. Structural properties of garnets under pressure: An *ab initio* study. Zeitschrift für Kristallographie 214, 808-819.

Angel, R.J., 2000. Equations of state, in: Hazen, R.M., Downs, R.T. (Eds.), High-temperature and high-pressure crystal chemistry, Review in Mineralogy and Geochemistry, vol 41, Mineralogical Society of America and the Geochemical Society, Washington DC, pp 35–39.

Angel, R.J., 2003. Automated profile analysis for single-crystal diffraction data. Journal of Applied Crystallography 36, 295-300.

Angel, R.J., Finger, L.W., 2011. SINGLE: a program to control single-crystal diffractometers. Journal of Applied Crystallography 44, 247-251.

Angel, R.J., Allan, D.R., Miletich, R., Finger, L.W., 1997. The use of quartz as an internal pressure standard in high pressure crystallography. Journal of Applied Crystallography 30, 461-466.

Angel, R.J., Bujak, M., Zhao, J., Gatta, G.D., Jacobsen, S.D., 2007. Effective hydrostatic limits of pressure media for high-pressure crystallography. Journal of Applied Crystallography 40, 26-32.

Angel, R.J., Alvaro, M., Nestola, F., Mazzucchelli, M., 2014a. Diamond thermoelastic properties and implications for determining the pressure of formation of diamond-inclusion systems. Russian Geology and Geophysics Journal. (submitted).

Angel, R.J., Mazzucchelli, M., Alvaro, M., Nimis, P., Nestola, F., 2014b. Geobarometry from host-inclusion systems: the role of elastic relaxation. American Mineralogist, in press.

Angel, R.J., Gonzalez-Platas, J., Alvaro, M., 2014c. EosFit-7c and a Fortran module (library) for equation of state calculations. Zeitschrift für Kristallographie 229, 405-419.

Armbruster, T., Geiger, C.A., Lager, G.A., 1992. Single-crystal X-ray structure study of synthetic pyrope almandine garnets at 100 and 293 K. American Mineralogist 77, 512-521.

Birch, F., 1947. Finite elastic strain of cubic crystals. Physical Review 71, 809-824.

Bosenick, A., Geiger, C.A., 1997. Powder X ray diffraction study of synthetic pyrope-grossular garnets between 20 and 295 K. Journal of Geophysical Research 102, 22649-22657.

Chen, G., Cooke, J.A., Gwanmesia, G.D., Liebermann, R.C., 1999. Elastic wave velocities of $Mg_3Al_2Si_3O_{12}$-pyrope garnet to10 GPa. American Mineralogist 84, 384–388.

Duffy, T.S., Anderson, D.L., 1989. Seismic velocities in mantle minerals and the mineralogy of the upper mantle. Journal of Geophysical Research 94, 1895–1912.

Erba, A., Mahmoud, A., Orlando, R., Dovesi, R., 2014. Elastic properties of six silicate garnet end members from accurate ab initio simulations. Physics and Chemistry of Minerals 41, 151-160.

Fei, Y., 1995. Thermal expansion, in: Ahrens, T.J. (Ed.), Mineral Physics and Cristallography, A Handbook of Physical Constants. American Geophysical Union, Washington, DC.

Geiger, C.A. 1999. Thermodynamics of $(Fe^{2+},Mn^{2+},Mg,Ca)_3Al_2Si_3O_{12}$ Garnet: An analysis and review. Mineralogy and Petrology 66, 271-299.

Geiger, C.A., Feenstra, A., 1997. Molar volumes of mixing of almandine-pyrope and almandine-spessartine garnets and the crystal chemistry of aluminosilicate garnets. American Mineralogist 82, 571-581.

Geiger, C.A., Langer, K., Bell, D.R., Rossman, G.R., Winkler, B., 1991. The hydroxal component in synthetic pyrope. American Mineralogist 76, 49-59.

Gwanmesia, G.D., Liebermann, R.C., 1993. Hot pressing of polycrystals of high pressure phases of mineral phases of mantle minerals in multi-anvil apparatus. Pure and Applied Geophysics 141, 467-484.

Gwanmesia, G.D., Zhang, J., Darling, K., Kung, J., Li, B., Wang, L., Neuville, D., Liebermann, R.C., 2006. Elasticity of polycrystalline pyrope ($Mg_3Al_2Si_3O_{12}$) to 9 GPa and 1,000° C. Physics of the Earth and Planetary Interiors 155, 179–190.

Gwanmesia, G.D., Jackson, I., Liebermann, R.C., 2007. In search of the mixed derivative q2M/qPqT (M = G, K): joint analysis of ultrasonic data for polycrystalline pyrope from gas- and solid medium apparatus. Physics and Chemistry of Minerals 34, 85–93.

Hazen, R.M., Finger, L.W., 1978. Crystal structures and compressibilities of pyrope and grossular to 60 kbar. American Mineralogist 63, 297-303.

Holland, T.J.B., Powell, R., 2011. An improved and extended internally consistent thermodynamic dataset for phases of petrological interest, involving a new equation of state for solids. Journal of Metamorphic Geology 29, 333–383.

Huang, S., Chen, J., 2014. Equation of state of pyrope-almandine solid solution measured using a diamond anvil cell and in-situ synchrotron X-ray diffraction. Physics of the Earth and Planetary Interiors 228, 88-91.

Isaak, D.G., Graham, E.K., 1976. The elastic properties of an almandine-spessartine garnet and elasticity in the garnet solid solution series. Journal of Geophysical Research 81, 2483–2489.

King, H.E., Finger, L., 1979. Diffracted beam crystal centering and its application to high pressure crystallography. Journal of Applied Crystallography 12, 374–378.

Kroll, H., Kirfel, A., Heineman, R., Barbier, B., 2012. Volume thermal expansion and related thermophysical parameters in the Mg, Fe olivine solid-solution series. European Journal of Mineralogy 24, 935-956.

Leger, J.M., Redon, A.M., Chateau, C., 1990. Compressions of synthetic pyrope, spessartine, and uvarovite garnets up to 25 GPa. Physics and Chemistry of Minerals 17, 161–167.

Leitner, B.J.,Weidner, D.J., Liebermann, R.C., 1980. Elasticity of single crystal pyrope and implications for garnet solid solution series. Physics of the Earth and Planetary Interiors 22, 111–121.

Levien, L., Prewitt, C.T., Weidner, D.J., 1979. Compression of pyrope. American Mineralogist 64, 7–8.

Mather, K.A., Pearson, D.G., McKenzie, D., Kjarsgaard, B.A., Priestley, K., 2011. Constraints on the depth and thermal history of cratonic lithosphere from peridotite xenoliths, xenocrysts and seismology. Lithos 125, 729-742.

McKenzie, D., Jackson, J., Priestley, K., 2005. Thermal structure of oceanic and continental lithosphere.

Earth and Planetary Science Letters 233, 337-349.

Miletich, R., Allan, D.R., Kuhs, W.F., 2000. High-pressure single crystal techniques. in: Hazen, R.M., Downs, R.T. (Eds.), High-temperature and high-pressure crystal chemistry, Review in Mineralogy and Geochemistry, vol 41, Mineralogical Society of America and the Geochemical Society, Washington DC, pp. 445-519.

Milman, V., Akhmatskaya, E. V., Nobes, R. H., Winkler, B., Pickardc, C. J., White, J. A., 2000. Systematic *ab initio* study of the compressibility of silicate garnets. Acta Crystallographica Section B 57, 163-177.

Mittal, R., Chaplot, S. L., Choudhury, N., C.-K. Loong, 2001. Inelastic neutron scattering and lattice-dynamics studies of almandine $Fe_3Al_2Si_3O_{12}$. Physics Review B 61, 3983-3988.

Nestola, F., Merli, M., Nimis, P., Parisatto, M., Kopylova, M., Stefano, A.D., Longo, M., Ziberna, L., Manghnani, M., 2012. In-situ analysis of garnet inclusion in diamond using single-crystal X-ray diffraction and X-ray micro-tomography. European Journal of Mineralogy 24, 599-606.

Nickel, K.G., Green, D.H., 1985. Empirical geothermobarometry for garnet peridotites and implications for the nature of the lithosphere, kimberlites and diamonds. Earth and Planetary Science Letters 73, 158–170.

Nimis, P., Taylor, W.R., 2000. Single-clinopyroxene thermobarometry for garnet peridotites. Part I. Calibration and testing of a Cr-in-Cpx barometer and an enstatite-in-Cpx thermometer. Contribution to Mineralogy and Petrology 139, 541–554.

Nobes, R.H., Akhmatskaya, E.V., Milman, V., Winkler, B., Pickard, C.J., 2000. Structure and properties of aluminosilicate garnets and katoite: an ab initio study. Computational Materials Science 17, 141-145.

O'Neill, B., Bass, J.D., Rossman, G.R., Geiger, C.A., Langer, K., 1991. Elastic properties of pyrope. Physica and Chemistry of Minerals 17, 617–621.

Ottonello, G., Bokreta, M., Sciuto, P.F., 1996. Parameterization of energy and interactions in garnets: End-member properties. American Mineralogist 81, 429-447.

Pandolfo, F., Cámara, F., Domeneghetti, M.C., Alvaro, M., Nestola, F., Karato, S.I., Amulele, G., 2014. Volume thermal expansion along the jadeite-diopside join. Physics and Chemistry of Minerals, in press.

Ralph, R.L., Finger, L.W., 1982. A computer program for refinement of crystal orientation matrix and lattice constraints from diffractometer data with lattice symmetry constraints. Journal of Applied Crystallography 15, 537–539.

Rosenfeld, J.L., Chase, A.B., 1961. Pressure and temperature of crystallization from elastic effects around solid inclusions in minerals?. American Journal of Science 259, 519-541.

Salje, E.K.H., Wruck, B., Thomas, H., 1991. Order-parameter saturation and low-temperature extension of Landau theory. Zeitschrift fur Physik B Condensed Matter, 82, 399-343.

Sato, Y., Akaogi, M., Akimoto Syun-iti, 1978. Hydrostatic compression of the synthetic garnets pyrope and almandine. Journal of Geophysical Research 83, 335-338.

Shirey, S.B., Cartigny, P., Frsto, D.J., Keshav, S., Nestola, F., Nimis, P., Pearson, D.G., Sobolev, N.V., Walter, M.J., 2013. Diamonds and geology of mantle carbon, in: Hazen, R.M., Jones A.P., Baross, J.A. (Eds.), Carbon in Earth, Rev Mineral Geochem, vol 75, Mineralogical Society of America and the Geochemical Society, Washington DC, pp 355-421.

Sinogeikin, S.V., Bass, J.D., 2000. Single-crystal elasticity of pyrope and MgO to 20GPa by Brillouin scattering in the diamond cell. Phys. Earth Planet. Int. 120, 43–62.

Sinogeikin, S.V., Bass, J.D., 2002. Elasticity of pyrope and majorite-pyrope solid solutions to high temperatures. Earth and Planetary Science Letters 203, 549–555.

Skinner, B.J., 1956. Physical properties of end-members of the garnet group. American Mineralogist 41, 428-436.

Soga, N., 1967. Elastic constants of garnet under pressure and temperature. Journal of Geophysical Research 72, 4227– 4234.

Stachel, T., Harris, J.W., 2008. The origin of cratonic diamonds – Constraints from mineral inclusions. Ore Geology Review 34, 5-32.

Takahashi, T., Liu Lin-gun, 1970. Compression of ferromagnesian garnets and the effect of solid solutions on the bulk modulus. Journal of Geophysical Research 75, 5757-5766.

Thieblot, L., Roux, J., Richet, P., 1998. High-temperature thermal expansion and decomposition of garnets.

European Journal of Mineralogy 10, 7-15.

Yagi, T., Akaogi, M., Shimomura, O., Tamai, H., Akimoto, S., 1987. High pressure and high temperature equations of state of majorite, in: Manghnani, M.H., Sono, Y. (Eds.), High pressure research in mineral physics. Terrapub., Tokyo, pp 141–147.

Yeganeh-Haeri, A., Weidner, D.J., Ito, E., 1990. Elastic properties of the pyrope-majorite solid solution series. Geophysical Research Letters 17, 2453-2456.

Zhang, Y., 1998. Mechanical and phase equilibria in inclusion-host systems. Earth and Planetary Science Letters 157, 209-222.

Zhang, L., Ahsbahs, H., Kutoglu, A., 1998. Hydrostatic compression and crystal structure of pyrope to 33 GPa. Physics and Chemistry of Minerals 25, 301–307

Zhang, L., Ahsbahs, H., Kutoglu, A., Geiger, C.A., 1999. Single-crystal hydrostatic compression of synthetic pyrope, almandine, spessartine, grossular and andradite garnets at high pressures. Physics and Chemistry of Minerals 27, 52-58.

Ziberna, L., Nimis, P., Kuzmin, D., Malkovets, V.G., 2014. Optimized electron microprobe analysis for single-clinopyroxene geobarometry: applications to xenocrysts in kimberlites (Upper Muna field, Yakutia) and diamond inclusions (Premier, South Africa), submitted.

Zou, Y., Gréaux, S., Irifune, T., Whitaker, M.T., Shinmei, T., Higo, Y., 2012. Thermal equation of state of $Mg_3Al_2Si_3O_{12}$ pyrope garnet up to 19 GPa and 1,700 K. Physics and Chemistry of Minerals 39, 589-598.

Supplementary tables

Table A1. Unit-cell parameters and volume of pyrope at different temperatures.

T(K)	a(Å)		V(Å^3)	
291	11.4573	(6)	1503.98	(25)
303	11.4589	(3)	1504.64	(11)
323	11.4607	(4)	1505.34	(14)
348	11.4632	(3)	1506.33	(13)
373	11.4658	(3)	1507.33	(12)
398	11.4686	(4)	1508.47	(15)
423	11.4714	(3)	1509.54	(12)
448	11.4734	(3)	1510.36	(11)
473	11.4769	(4)	1511.72	(15)
498	11.4792	(3)	1512.63	(12)
523	11.4818	(3)	1513.65	(12)
548	11.4841	(3)	1514.58	(13)
573	11.4872	(3)	1515.80	(12)
598	11.4905	(3)	1517.12	(12)
623	11.4927	(3)	1517.98	(12)
648	11.4955	(4)	1519.07	(15)
673	11.4981	(3)	1520.12	(13)
698	11.5011	(3)	1521.30	(13)
723	11.5040	(4)	1522.44	(14)
748	11.5071	(3)	1523.68	(12)
773	11.5100	(3)	1524.83	(11)
798	11.5126	(3)	1525.89	(12)
823	11.5157	(3)	1527.12	(13)
848	11.5178	(4)	1527.93	(16)
873	11.5211	(3)	1529.24	(12)
898	11.5238	(4)	1530.32	(14)
923	11.5270	(4)	1531.61	(16)
948	11.5302	(3)	1532.90	(12)
973	11.5330	(3)	1534.00	(14)
998	11.5356	(3)	1535.03	(12)
1023	11.5383	(3)	1536.13	(10)
1048	11.5415	(3)	1537.42	(13)
1073	11.5437	(4)	1538.29	(16)

Note: Standard deviations are given in parentheses.

Table A2. Unit-cell edge and volume for pyrope at different pressures.

P (GPa)	a (Å)	V (Å^3)
0.0001(1)	11.4624(4)	1505.987(168)
1.546(6)	11.4280(5)	1492.479(177)
2.185(7)	11.4144(4)	1487.159(152)
2.895(7)	11.3986(4)	1481.014(152)
3.983(8)	11.3767(4)	1472.478(134)
5.081(9)	11.3547(3)	1463.947(123)
6.553(9)	11.3263(3)	1453.008(118)
7.304(10)	11.3132(3)	1447.958(123)
8.456(12)	11.2931(5)	1440.248(185)
8.175(11)[a]	11.2982(3)	1442.211(109)
5.829(9)[a]	11.3408(3)	1458.584(126)
2.110(7)[a]	11.4158(3)	1487.714(119)

[a]Data measured during decompression. Standard deviations are given in parentheses.

Table A3. Unit-cell edge and volume for almandine at different pressures.

P (GPa)	a (Å)	V (Å^3)
0.0001(1)	11.5317(3)	1533.493(126)
0.588(6)	11.5184(3)	1528.170(117)
1.413(7)	11.5012(3)	1521.345(118)
2.438(7)	11.4794(3)	1512.711(115)
3.619(9)	11.4558(3)	1503.388(122)
4.713(9)	11.4345(3)	1495.035(135)
7.129(10)	11.4013(3)	1477.828(170)
6.503(9)[a]	11.4013(3)	1482.065(133)
5.973(9)[a]	11.4109(3)	1485.791(110)
5.497(10)[a]	11.4198(3)	1489.274(123)
4.067(7)[a]	11.4469(3)	1499.912(121)
2.738(8)[a]	11.4739(3)	1510.533(119)
1.961(8)[a]	11.4898(3)	1516.840(107)
1.342(7)[a]	11.5031(3)	1522.113(117)

[a]Data measured during decompression. Standard deviations are given in parentheses.

Table A4. Unit-cell edge and volume for $Py_{60}Al_{40}$ at different pressures.

P (GPa)	a (Å)	V (Å^3)
0.0001(1)	11.4885(4)	1516.319(157)
0.225(21)	11.4841(6)	1514.582(241)
0.862(11)	11.4689(4)	1508.555(153)
1.704(13)	11.4504(4)	1501.274(159)
2.571(14)	11.4319(3)	1494.006(131)
4.300(20)	11.3971(4)	1480.417(137)
5.435(15)	11.3743(3)	1471.541(125)
6.729(18)	11.3495(4)	1461.957(140)
7.441(19)	11.3377(3)	1457.394(129)
8.046(23)	11.3262(4)	1452.951(133)
6.257(25)[a]	11.3578(5)	1465.160(183)
4.917(18)[a]	11.3853(4)	1475.817(164)
3.834(16)[a]	11.4071(5)	1484.319(197)
3.271(23)[a]	11.4177(6)	1488.437(227)

[a]Data measured during decompression. Standard deviations are given in parentheses.

Table A5. Literature results on the pressure behavior of pyrope.

	Experimental Method	V_0 (Å^3)	K_{T0} (GPa)	K'	Pressure Medium	P_{max}(GPa)	Synthesis Method
Takahashi and Liu, 1970	X-ray powder diffraction	1502.7	190(6)	5.45	NaCl	32.8	stiochiometric mixture of oxides in a piston cylinder device, at 1000°C & 25 kbar
Hazen & Finger, 1978	X-ray single crystal diffraction	1503.5 (4)	133.0(3)	-	water + glycerin	5.6 (1)	1300°C & 36 kbar, presence of water
Sato et al., 1978	X-ray powder diffraction	1503.9	171(3)	1.8(7)	methanol:ethanol; 4:1	10.0	oxides mixture in a tetrahedral anvil high pressure apparatus at 37 kbar & 1000 °C
Levien et al., 1979	X-ray single crystal diffraction	1503.4 (5)	175 (1)	4.5 (5)	methanol:ethanol; 4:1	4.96 (5)	Leitner & Weidner (1978)
Leitner et al., 1980	single crystal Brillouin	1501.517	173.5 (1)	-	-	-	piston cylinder, 26 kbar & 1200°C, mixture oxides + 10% H_2O
Leger et al., 1990	X-ray powder diffraction	1503.878	175(1)	3.4(1)	1 NaCl:1 pyrope 1 NaCl+1 pyrope+silicon grease	25	belt type apparatus, 3.7 GPa & 1000°C, 30 min
O'Neill et al., 1991	single crystal Brillouin	1503.878	171.6 (3)	-	-	-	1000°C & P_{H2O} = 235 kbar
Ottonello et al., 1996	fictive compression model	1504.706	177.678	5.7288	-	-	-
Zhang et al., 1998	X-ray single crystal diffraction	1502.9(3)	171 (2) 159(3) 168(1)	4.4(2) 6.4(6) 4.7(1)	He Ne He + Ne	33	synthesized hydrothermally at high pressure and temperature in a piston cylinder device (Armbruster et al., 1992)

Table A5. Continue.

	Experimental Method	V_0 (Å^3)	K_{T0} (GPa)	K'	Pressure Medium	P_{max}(GPa)	Synthesis Method
Chen et al., 1999	ultrasonic interferometry	-	169.8(2)	5.2(4)	sample surrounded by lead was put in a pyrophillite octhaedron and compresed by 8 WC cubes	10	5 GPa at 1350°C for 2 h; uniaxial sphere apparatus
Akhmatskaya et al., 1999	DFT	1479.60	170(2)	4.34(9)	-	100	-
Sinogeikin & Bass, 2000	Brillouin single crystal,	-	169.7(20)	4.1(3)	methanol:ethanol:water 16:3:1	20	-
Milman et al., 2000	DFT	1490.9	165	4.3	-	-	-
Mittal et al., 2001	lattice dynamic calculation	1501.91	182.4	-	-	-	-
Sinogeikin & Bass, 2002	single crystal Brillouin	1503.878(788)	169.4(2)	-	-	-	1000 °C & P_{H2O} = 23.5 kbar
Gwanmesia et al., 2006	ultrasonic interferometry	-	173.5(2)	3.9(3)	cubic boron-epoxy	8.7	polycristalline Py_{100} was hot pressed from a homogeneous glass in a Pt capsule, at 1000°C & 9 GPa
	X-ray		170(2)	4.3(3)			
Gwanmesia et al., 2007	ultrasonic interferometry	-	166.0(8)	5.46	-	0.3	polycristalline specimens of Py_{100} was hot pressed using a homogeneous glass of Py_{100} in a Pt capsule, surrounded by a NaCl at 1000°C & 9 GPa
Zou et al., 2012	X-ray using a Kawai-type apparatus	1500.7(19)	167(6)	4.6(3)		19	

Table A5. Continue.

	Experimental Method	V_0 (Å^3)	K_{T0} (GPa)	K'	Pressure Medium	P_{max}(GPa)	Synthesis Method
Erba et al., 2014	DFT	-	164.8	-	-	-	-
This work	single crystal X-ray diffraction	1506.15(16??)	163.7(1.7)	6.4(4)	methanol:ethanol, 4:1	8	synthesized hydrothermally at high pressure and temperature in a piston cylinder device (Armbruster et al., 1992)

Notes: All bulk modulus values are referenced to the isothermal value at 298 K. Thermodynamic parameters used for the adiabatic to isothermal bulk moduli conversion are: γ = 1.15 (Zou et al., 2012), α = 2.543*10^{-5} K^{-1} (this work) and T = 298 K. K_0 from DFT calculations at 0 K, value at 298 K is corrected by -5 GPa.

Table A6. Literature results on the pressure behavior of almandine.

	Expermental method	V_0 (Å^3)	K_{T0} (GPa)	K'	Pressure medium	P_{max}(GPa)	Synthesis Method
Takahashi and Liu, 1970	X-ray powder diffraction	1533.6	190(5)	3.0(5)	NaCl	32.8	synthesized at Carnegie Geophysical Laboratory (run 24, 1954)
Sato et al., 1978	X-ray powder diffraction	1531.2	175(7)	1.5(1.6)	methanol:ethanol, 4:1	10.0	oxide mixture in a tetrahedral anvil high pressure apparatus at 30 kbar & 1300 °C
Yagi et al., 1987	X-ray single crystal diffraction	1534.01(1.6)	168.3	4	methanol:ethanol, 4:1	6	oxides mixture at 4 GPa & 1000 °C
Ottonello et al., 1996	fictive compression model	1531.333	183.833	5.7466	-	-	-
Zhang et al., 1999	X-ray single crystal diffraction	1528.625(2)	185(3)	4.2(3)	Ne 0-14.6 He 11.6-21.3	21.3	synthesized hydrothermally at high pressure and temperature in a piston cylinder device (Armbruster et al., 1992)
Akhmatskaya et al., 1999	DFT	1524.4	173.5(3.5)	4.2(2)	-	-	-
Nobes et al., 2000	DFT	1524.4	172	3	-	-	-
Milman et al., 2000	DFT	1523.7	173	4.2	-	-	-
Mittal et al., 2001	lattice dynamic calculation	1534.2	180.2	-	-	-	-
Erba et al., 2014	DFT	-	169.8	-	-	-	-
This work	X-ray single crystal diffraction	1533.52(10)	172.6(1.5)	5.8(5)	methanol:ethanol, 4:1	7	synthesized hydrothermally at high pressure and temperature in a piston cylinder device (Armbruster et al., 1992)

Notes: All bulk modulus values are referenced to the isothermal value at 298 K. Thermodynamic parameters used for the adiabatic to isothermal bulk moduli conversion are: $\gamma = 1.22$ (Soga, 1967), $\alpha = 1.851(1)*10^{-5} K^{-1}$, and $T = 298$ K. K_0 from DFT calculations at 0 K, value at 298 K is corrected by -3 GPa.

MANUSCRIPT 2

EQUATIONS OF STATE FOR GROSSULAR AND UVAROVITE GARNETS

S. Milani, M. Alvaro, T. Boffa-Ballaran, S. Klemme, M.C. Domeneghetti, F. Nestola

ABSTRACT

In-situ high-pressure X-ray diffraction experiments were carried out on synthetic single crystals of grossular ($Ca_3Al_2Si_3O_{12}$) and uvarovite ($Ca_3Cr_2Si_3O_{12}$) garnets. Unit-cell volumes were measured from room pressure to about 8 GPa at room temperature in a diamond-anvil cell with a 4:1, methanol-ethanol pressure medium. Furthermore, a high-temperature experiment was carried out on a synthetic single crystal of grossular, using a micro-furnace from 293 K to 1073 K. The pressure-volume data were fitted to a third order Birch-Murnaghan equation of state (EoS) yielding the following EoS coefficients: V_0 = 1664.39(18) Å^3, K_{T0} = 167(2.0) GPa and $K`$ = 5.0(5) for the grossular and $V_0$ = 1731.07(18) Å$^3$, $K_{T0}$ = 157.9(1.8) GPa and $K`$ = 5.4(5) for uvarovite. The volume-temperature data for grossular fitted to a Kroll-type EoS, using an Einstein temperature value of 500 K, yielded the following coefficients: V_0 = 1664.49(5) Å^3 and $\alpha_{(300K,\ 1bar)}$ = 2.107(7)*10^{-5} K^{-1}. The thermoelastic parameters determined in this study will be used in a thermal-pressure-type EoS to (i) understand the variation of elastic properties within the grossular uvarovite solid solutions and (ii) calculate the entrapment pressures, P_e, of garnet inclusions in diamond at mantle P and T conditions.

Keywords: grossular, uvarovite, high-pressure, high-temperature, diffraction, bulk modulus, diamond

1. INTRODUCTION

Stable over a wide range of pressure and temperature conditions, garnets are among the most abundant phases in the Earth's upper mantle and transition zone. According to the pyrolitic compositional model, the Earth's upper mantle (e.g. up to approximately 410 km depth) is mainly composed of 63% olivine, 22% pyroxene, and 15% garnet by volume (Ringwood 1975; Ita and Stixrude 1992). Due to the broad chemical variability of garnets, investigating the compositional dependence of garnet elasticity within garnet solid solutions has always been the main focus of several mineral physics and petrology scientific articles (e.g. Takahashi and Liu 1970, Leitner

et al. 1980). It seems clear that a necessary prerequisite for understanding the variation of elastic properties within solid solutions is to provide accurate values for the end-members.

Moreover, garnet is one of the most abundant mineral phases found as inclusions trapped in lithospheric diamonds (Stachel and Harris 2008). Recently it has been shown that the pressure of formation for diamonds and their inclusions can be determined if the residual pressure of the inclusion and the thermoelastic parameters of the host and the inclusion are known (e.g. Izraeli et al. 1999; Nestola et al. 2011; Angel et al. 2014 a, b). Accurate characterization of the elastic properties of garnet end-members is therefore essential also to the aim of determining the entrapment pressure for diamond-inclusion pair (see Milani et al. 2015). Based on the Ca-Cr content in the garnet inclusions, the diamonds parageneses can be divided into three groups, peridotitic (lherzolitic, wherlitic, harzuburgitic), eclogitic and websteritic. A careful examination of 404 analyses of garnets found as inclusions in diamonds, of which 228 are peridotitic, 154 are eclogitic and 22 are websteritic, revealed that in the case of peridotitic garnets ca. 90% of them are composed by the pyrope-almandine solid solution and 10 % by the grossular and uvarovite components. Grossular and uvarovite components constitute up to the 23% in eclogitic garnets, while in the websteritic ones they represent about 12% (see Milani et al. 2015). Determining the equations of state of pyrope, almandine, grossular and uvarovite is therefore fundamental for the correct application of the geobarometer based on the thermoelastic parameters of these garnets thus constraining the pressure and hence the depth of formation for diamond-inclusion pairs. After the work by Milani et al. (2015), where the EoS for pyrope and almandine have been determined, here we provide new EoS for grossular and uvarovite determined using the same methodology. Therefore all of these data, consistent one to another, can be used to perform calculations of the thermoelastic parameters for intermediate compositions. Elastic properties of grossular and uvarovite garnets for both synthetic and natural single crystals and polycrystals have been widely investigated with several techniques, including ultrasonic interferometry, brillouin scattering and static compression methods (e.g. Zhang et al. 1999; Kono et al. 2010; Kawai et al. 2012) and DFT calculations (e.g. Erba et al. 2014).

2. Experimental and analytical methods

2.1 Sample synthesis and characterization

Synthetic single crystals of pure grossular (Gr_{100}) and pure uvarovite (Uv_{100}) garnets were synthesized from different starting materials using a multi-anvil apparatus at the Bayerisches Geoinsitut. A stoichiometric mixture of high-purity oxide powders were grinded in an agate mortar for 60 mins under ethanol and then decarbonated at 1000°C for 360 mins; the temperature from 25°C to 1000°C was reached in 660 mins. The starting compositions were packed into platinum capsules of 3.5 mm length and 2 mm diameter. In the uvarovite synthesis experiment 2 µl of H_2O was added with a syringe before closing the capsule to help the crystallization. Samples were synthesized at 6 GPa and 1300°C. The experimental sample was heated in 23 mins and the temperature was kept to 1300°C for 40 mins. Each multi-anvil experiment was performed with Cr-doped MgO octahedra of 18 mm edge length combined with tungsten carbide cubes of 11 mm truncation edge length. For all the experiments a graphite heater was employed. Experiments were quenched by cutting the electrical power supply to the furnace. Single-crystals of up to ca. 100 µm were recovered from the capsules. The compositions of the crystals have been determined by electron microprobe at the University of Padova using a Cameca CAMEBAX-micro operating at 20 nA and 20 kV with standards of pyrope for Mg, diopside for Si and Ca, Al_2O_3 for Al, Cr_2O_3 for Cr and Fe_2O_3 for Fe. Results from the chemical analyses are reported in Table 1. Four crystals (with size ca. 80 x 30 x 30 µm) were selected based on the absence of twinning and visible inclusions and on the quality of their diffraction peak profiles.

Table 1 Averaged composition obtained from EMPA analyses on grossular and uvarovite synthetic single crystal garnets.

	Grossular	Uvarovite
n. analyses	8	11
SiO_2	40.13 (13)	35.98 (18)
Al_2O_3	22.33 (10)	0.01 (01)
Cr_2O_3	0.03 (02)	29.11 (16)
CaO	37.83 (16)	33.80 (13)
Total	100.32	98.89

Standard deviations are given in parentheses.

2.2 High-pressure and high-temperature single crystal X-ray diffraction experiments

High-pressure experiments

High-pressure single-crystal X-ray diffraction experiments for the grossular garnet were carried out with a Huber four-circle diffractometer at the Bayerisches Geoinsitut, while the high-pressure single-crystal X-ray diffraction experiment for the uvarovite sample was carried out with a STOE STADI-IV four-circle diffractometer at the University of Padova. Both the diffractometers were equipped with a point detector, a MoKα radiation, operating at 50 kV and 40 mA, and automated by the SINGLE software (Angel and Finger 2011). The samples were loaded in two different experimental runs in an ETH-type diamond-anvil cell (Miletich et al. 2000) using a steel gasket, pre-indented to 100 - 110 μm of thickness and with a hole diameter of 230 - 250 μm. A pressure transmitting medium of methanol:ethanol mixture 4:1 was used, which remains hydrostatic up to about ~ 9.5 GPa (Angel et al. 2007). For each sample a single crystal of quartz was also loaded in the diamond-anvil cell and used as a pressure standard (Angel et al. 1997). During the centering procedure, the effects of crystal offsets and diffractometer aberrations were eliminated from the refined peak position by the eight-position centering method (King and Finger 1979). Unconstrained unit-cell parameters were obtained by vector least-squares centering (Ralph and Finger 1982) of not less than 20 reflections up to 2θ = 29°. The symmetry-constrained unit-cell edges reported in Table 2 and 3 were found to be within 1 e.s.d. deviation of the unconstrained ones thus confirming the cubic symmetry within 1 e.s.d.

High-temperature experiments

The high-temperature single-crystal X-ray diffraction experiments were performed at the University of Pavia with a HUBER four-circle diffractometer automated with SINGLE software (Angel and Finger 2011). This diffractometer is equipped with a newly designed micro-furnace (see Alvaro et al. 2015 for further details), which is controlled by an Eurotherm temperature regulator. The grossular single crystal was mounted inside a thin quartz vial (0.3 mm inner diameter and 26 mm long) and was held in place by means of quartz wool. The vial was mounted on a metal goniometer head on the diffractometer (Mo*Kα* radiation) operating at 50 kV and 30 mA and equipped with a 0.8 mm short collimator. The micro-furnace was placed on top of the goniometer head. The micro-furnace device and the temperature calibration

procedure are described in details in Alvaro et al. (2015). The room pressure unit-cell parameters (Table 4) were determined at 26 different temperatures up to 1073 K. The effects of the crystal offsets and the diffractometer aberrations were removed by using the eight-position centering method (King and Finger 1979) before starting the high-temperature measurements. Unconstrained unit-cell parameters confirmed the cubic symmetry within 1 e.s.d. therefore only constrained unit-cell parameters obtained by vector least-squares fit (Ralph and Finger 1982) are reported in Table 4.

Table 2
Unit-cell edge and volume at different pressures for grossular.

P (GPa)	a (Å)	V (Å^3)
0.0001(1)	11.8508 (3)	1664.344 (143)
1.013(9)	11.8275 (4)	1654.553 (150)
2.392(10)	11.7963 (4)	1641.467 (154)
3.568(10)	11.7712 (3)	1631.043 (128)
4.715(11)	11.7469 (3)	1620.946 (126)
6.559(15)	11.7101 (4)	1605.757 (152)
7.149(12)	11.6986 (3)	1601.046 (142)
7.674(19)	11.6886 (5)	1596.945 (195)

Standard deviations are given in parentheses.

Table 3
Unit-cell edge and volume at different pressures for uvarovite.

P (GPa)	a (Å)	V (Å^3)
0.0001(1)	12.0069 (5)	1730.993 (212)
0.861(9)	11.9857 (5)	1721.813 (219)
1.634(10)	11.9671 (5)	1713.833 (195)
2.309(10)	11.9511 (5)	1706.972 (234)
3.062(11)	11.9332 (5)	1699.305 (216)
3.534(13)	11.9228 (5)	1694.849 (220)
4.005(11)	11.9122 (5)	1690.336 (205)
4.663(13)	11.8980 (5)	1684.305 (208)
5.198(13)	11.8859 (5)	1679.169 (227)
5.907(13)	11.8711 (5)	1672.929 (198)
6.973(14)	11.8491 (6)	1663.608 (230)

7.547(15)	11.8381 (5)	1658.991 (225)

Standard deviations are given in parentheses.

Table 4
Unit-cell edge and volume of grossular at different temperatures.

T(K)	a(Å)	V(Å^3)
291	11.8499 (6)	1663.98 (20)
303	11.8503 (6)	1664.15 (23)
323	11.8525 (6)	1665.04 (25)
348	11.8548 (5)	1666.02 (21)
373	11.8570 (6)	1666.95 (24)
423	11.8627 (7)	1669.36 (28)
448	11.8648 (5)	1670.26 (22)
473	11.8673 (7)	1671.31 (31)
523	11.8726 (5)	1673.55 (21)
573	11.8776 (6)	1675.65 (26)
623	11.8826 (5)	1677.78 (22)
673	11.8880 (5)	1680.08 (22)
698	11.8905 (5)	1681.14 (21)
723	11.8934 (5)	1682.37 (23)
773	11.8984 (5)	1684.47 (23)
798	11.9009 (5)	1685.53 (22)
823	11.9041 (6)	1686.92 (23)
873	11.9088 (6)	1688.90 (25)
898	11.9114 (5)	1690.01 (22)
923	11.9139 (5)	1691.08 (23)
973	11.9193 (5)	1693.38 (22)
998	11.9224 (5)	1694.69 (21)
1023	11.9248 (5)	1695.71 (22)
1073	11.9297 (5)	1697.81 (22)

Note: Standard deviations are given in parentheses.

3. Results

The unit-cell volume for both samples (as reported in Table 2 and 3) decreases smoothly with increasing pressure, as shown in Fig. 1, up to the maximum hydrostatic pressure reached in this study of ca .7.5 GPa. Such pressure extensively covers the stability pressure range for upper mantle garnets. On the basis of the F_E-f_E plot (Fig. 2) a Birch-Murnaghan equation of state truncated at the third-order (BM3-EoS, Birch 1947) adequately describes the pressure-volume data. Simultaneous refinement of the BM3-EoS coefficients (volume, V_0, isothermal bulk modulus, K_{T0} and its first pressure derivative, $K`$) were performed using the program EoS-FIT7c (Angel et al. 2014c). The resulting coefficients were: $V_0$ = 1664.39(18) Å$^3$, $K_{T0}$ = 167.1(2.0) GPa and $K`$ = 5.0(5) for the grossular, and V_0 = 1731.07(18) Å^3, K_{T0} = 157.9(1.8) GPa and $K`$ = 5.4(5) for the uvarovite. The goodness of the fits was confirmed by the low ΔP_{max} value (calculated as $|P_{obs} - P_{calc}|$) being 0.010 GPa for grossular and 0.020 GPa for uvarovite. The values for the weighted χ^2 are 0.17 and 0.21 for grossular and uvarovite, respectively. These low χ^2 values means that the errors are overestimated (Angel 2000). At the same time the goodness of the data are confirmed by the small differences between the EoS coefficients obtained by the refinement and estimated by the F_E-f_E plot of Fig. 2, where the intercept corresponds to the bulk modulus, K_{T0}, and the slope of the straight line corresponds to the $K`$.

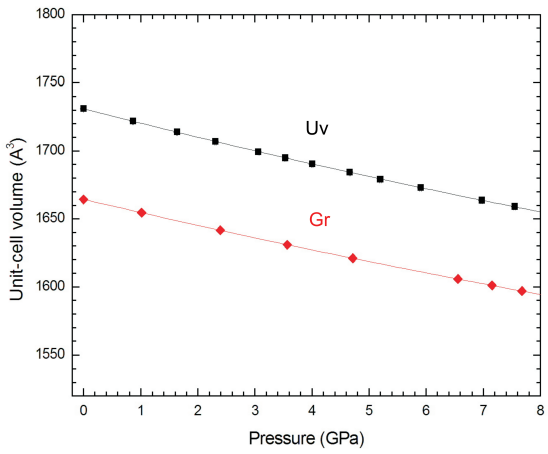

Fig. 1. Pressure-volume data for grossular and uvarovite. The solid lines are the Birch-Murnaghan 3rd – order EoS fit to the data. The error bars are smaller than the symbol size.

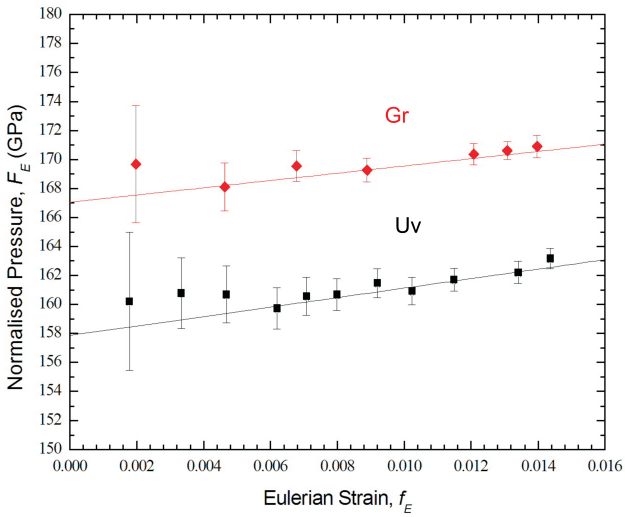

Fig. 2. F_E-f_E plot for grossular and uvarovite. The solid lines are the Birch-Murnaghan 3rd – order EoS fit to the data.

The evolution of the unit-cell volume of grossular with the temperature is reported in Fig. 3 and Table 4. A continuous linear increase of the unit-cell volume is observed as a function of temperature with no evidence of any irreversible change in the crystal occurred up to the maximum temperature reached (1073 K). Data collected both increasing and decreasing temperature overlap within experimental error, thus indicating good experimental reproducibility. The temperature-volume data were fitted using the software EoSFit7c (Angel et al. 2014c) to a Kroll-type EoS (Kroll et al. 2012). The thermal expansion coefficients obtained are $\alpha_{(303K,\ 1bar)}$ = 2.100(7)*10^{-5} K^{-1} and V_0 = 1664.42(5) Å^3. A comparison of calculated unit-cell volumes, using the fitted coefficients, and the experimentally measured unit-cell volumes in the high temperature regime [see Pandolfo et al. 2014 for a discussion of δV and statistical parameters from the fitting] confirms that the model equation provides a good fit over the whole temperature range.

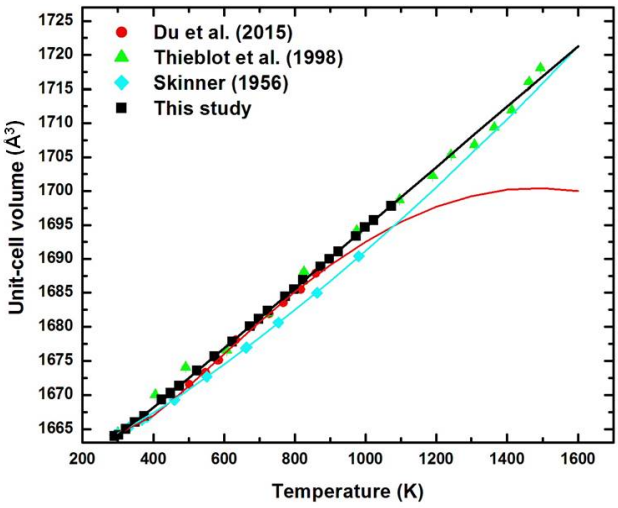

Fig. 3 Temperature-volume data for pure grossular compared with literature data from Skinner (1956), Thieblot et al. (1998), and Du et al. (2015). The solid lines are the Fei-type EoS fit to the data. The error bars are smaller than symbol size.

4. Discussion

The elasticity data determined in this work can be compared and combined to the existing literature data in order to better constrain the elastic behaviour of grossular and uvarovite garnets. The bulk modulus of grossular has been previously determined by different methods and authors (e.g. ultrasonic wave velocity, static compression experiments in diamond-anvil cell, ab-initio calculations) (Table 5, Fig. 4b). Only a few studies have been instead performed to determine the elasticity of uvarovite (Table 6, Fig. 4b). For purpose of comparison, the adiabatic bulk moduli (K_S) obtained with the ultrasonic wave velocity technique needs to be converted to K_{T0} by applying the relationship $K_S = K_{T0}\,(1 + \alpha\gamma T)$, where α is the thermal expansion, γ the Grüneisen parameter, and T the temperature. Static DFT calculations provide K_{T0} at 0 K. We therefore combined the high-temperature diffraction data of this work and previous low temperature data for grossular (Bosenick and Geiger 1997) to describe its thermal expansion behaviour and extrapolate the K_{T0} values from DFT calculations to room temperature conditions. The resulting K_{T0} at room temperature decreases by 2.5 GPa with respect to 0 K. These conversions were not possible for the uvarovite because reliable thermal expansion data could not be found in literature.

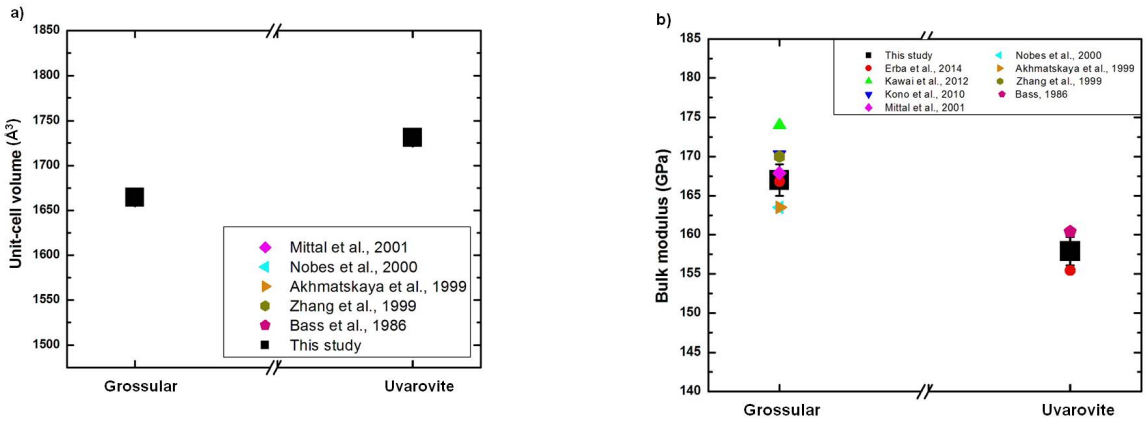

Fig. 4. Unit-cell volume (a) and bulk modulus (b) values obtained in this work compared with literture data. The isothermal bulk moduli are for 298 K.

Concerning the high-pressure studies, our V_0 values of grossular and uvarovite are in good agreement with literature data (Fig. 4a and Tables 5 and 6). The value for K_{T0} of grossular from this study approximately corresponds to the mid-range of previously published values (Fig. 4a, b and Tables 5 and 6) and agrees with a recent DFT calculated value (Erba et al. 2014). The largest difference in grossular bulk modulus value is with the lattice dynamical calculation results of Kawai et al. (2012). Also the value for K_{T0} of uvarovite roughly corresponds to the average of already published data (Fig. 4b and Table 6).

So far, high-temperature volume measurements on grossular garnet have only been performed by means of powder X-ray diffraction by Skinner (1956) on a not well characterized natural sample, and on synthetic grossular samples by Thieblot et al. (1998) and Du et al. (2015). For sake of comparison, these literature data have been re-fitted to Fei-type EoS (Fei 1995) (Table 7, and Fig. 3). However, while the data of Skinner (1956) have been fit over the entire temperature range from 284 K to 980 K, those from Thieblot et al. (1998) have been fitted from 300 K to 1453 K (i.e. well

Table 5. Literature bulk modulus values for grossular. The KT0 obtained by DFT have been extrapolated from 0 K to room temperature conditions (see text).

	Expermental method	V_0 (Å^3)	K_{T0} (GPa)	K'	Pressure medium	P_{max}(GPa)	Synthesis Method
Zhang et al., 1999	X-ray single crystal diffraction	1660.218(337)	170(4)	5.2(6)	Ne	11.8	synthesized hydrothermally at high pressure and temperature in a piston cylinder device (Armbruster et al., 1992)
Akhmatskaya et al., 1999	DFT	1667.0	166(2)	4.26(11)	-	-	-
Nobes et al., 2000	DFT	1666.96	166	4.3	-	100	-
Mittal et al., 2001	lattice dynamic calculation	1665.18	170.41	-	-	-	-
Kono et al., 2010	Ultrasonic wave velocity	-	170.3(8)	4.43(7)	MgO+NaCl sleves	17	Hot-pressed glass with grossular composition at ~7 GPa and ~1 673 K for 2 h using a 3 000-ton high-pressure apparatus
Kawai et al., 2012	DFT	-	176.5	4.43	-	30	-
Erba et al., 2014	DFT	-	169.3	-	-	-	-
This study	X-ray single crystal diffraction	1664.39(18)	167(2)	5.0(5)	methanol:ethanol (4 : 1)	7.7	Oxide mixture at 6 GPa and 1300°C in a multi-anvil press

Table 6. Literature bulk modulus values for uvarovite.

	Expermental method	V_0 (Å^3)	K_{T0} (GPa)	K'	Pressure medium	P_{max}(GPa)	Synthesis Method
Bass, 1986	Single crystal Brillouin	1726.70	160.4(2)	-	-	-	Flux method
Milman et al., 2001	DFT	1737.09	143(1)	4.73(18)	-	100	
Erba et al., 2014	DFT	-	155.43	-	-	-	-
This study	X-ray single crystal diffraction	1731.07(18)	157.9(1.8)	5.4(5)	methanol:ethanol (4 : 1)	7.7	Oxide mixture at 6 GPa and 1300°C in a multi-anvil press

Table 7. Thermal expansion behaviour of the grossular garnet fitted by a Fei-type EoS at 300 K.

$V_{303\ K}$ calculated (Å^3)	$\alpha_{300\ K}$ x10^{-5} (K^{-1})	a_0 x10^5 (K^{-1})	a_1 x10^{10} (K^{-2})	a_2 (K)	EoS formalism	Reference
1664.2(1)	2.3(3)	2.84(32)	-0.2(3)	-0.4(3)	Fei-type[4]	This work
1664.3(1)	1.7(4)	1.9(5)	0.8(5)	-0.4(4)		Skinner (1956)[1]
1664.3(3)	0.7(1.7)	6.60(18)	-4(2)	-4.1(15)		Du et al. (2015)[3]
1664.56(6)	2.102(7)				Kroll-type	This work

Note: [1]data have been fitted to the entire range of temperature (284 K to 980 K); [2]data have been fitted to the range of temperature between 300K-1453K not considering 3 outliers; [3] data have been fitted to the entire temperature range (296 K – 859 K) excluding two outliers. [4]Fei-type coefficients reported are calculated using as T_{ref} the first experimental temperature collected for each dataset.

below the decomposition temperature) excluding a few outliers at 607 K, 724 K, and 1241 K. On the other hand the data from Du et al. (2015) have been fitted to the entire temperature range 296 K to 859 K excluding two outliers at 393 K and 477 K. The results of all the extrapolations at 300 K are reported in Table 7 and shown Fig. 3. As shown in Table 7, there are considerable differences between our data and those from the literature. The thermal expansion parameters at 300 K from both Skinner (1956) and Du et al. (2015) are smaller than that calculated from our fitting. The discrepancy between our dataset and that by Skinner (1956) could be ascribed to the differences in composition as the sample used by Skinner (1956) referred to as a 'grossularite' has not been properly characterized. The thermal coefficient value obtained fitting the data by Du et al. (2015) is physically unreliable as with any thermal expansion model becomes negative high temperature. The same is true also for the data reported by Thieblot et al. (1998), where the thermal expansion value decreases with increasing temperature.

On the other hand, the very good agreement between our high-T data for grossular and those reported by Bosenick and Geiger (1997) for the low-T behavior on a synthetic pure grossular garnet allowed us to combine them in a unique dataset ranging from 45 K to 1073 K, without taking into account the more scattered data at 195, 220 and 295 K. This dataset allowed performing fit to a Kroll-type EoS (Kroll et al. 2012), leading to a much more reliable description of the thermal behavior for grossular from 20 K to 1073 K (Fig. 5 and Table 7). Furthermore, fitting the data by a Kroll-type EoS is fundamental to calculate the P_e for diamond-garnet pairs using a thermal pressure model as the results obtained with these two models are undistinguishable (see Angel et al. 2014 for further details). The reliability of the Einstein temperature used (500 K) has been confirmed by comparison with the saturation temperature (where $T_{sat} \approx \theta_E/2$) obtained from the fitting of the low-*T* data alone using a Salje-type EoS (Salje et al. 1991).

5. Implications on diamond inclusion geobarometry

The new data obtained here and the careful evaluation of literature data can be used to test how the uncertainties in elastic parameters and the adoption of different models affect the estimation of the entrapment pressure with the elastic method. As described by Angel et al (2014a,b), one of the fundamental step in the application of the elastic method for diamond inclusion geobarometry is the choice of the appropriate P-V-T equation of state. So far, the most used P-V-T EoS models require knowledge of the variation of the bulk

modulus with temperature at room pressure (here defined $\frac{\partial K_{0T}}{\partial T}$ model for the sake of simplicity). However, experimental determination of $\frac{\partial K_{0T}}{\partial T}$ is not straightforward. For this reason, the use of alternative models which allows to calculate the P-V-T

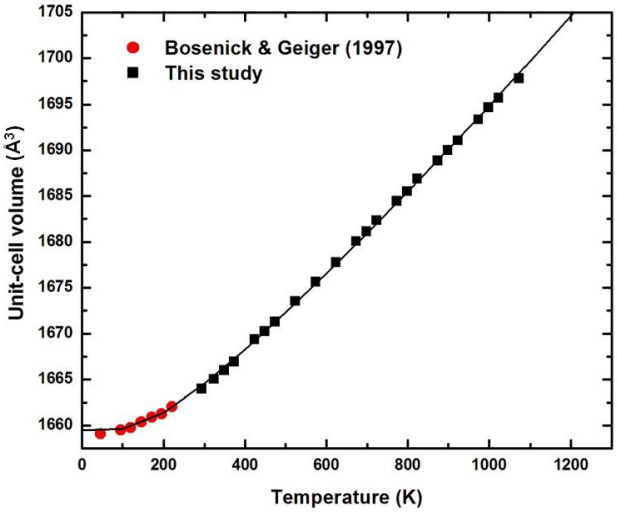

Fig. 5 Low-temperature volume data for pure grossular from Bosenick and Geiger (1997) combined with high-temperature volume data from this study. The solid line is the Kroll-type EoS fit to the data. The error bars are smaller than symbol size.

EoS without taking into account the $\frac{\partial K_{0T}}{\partial T}$ value (i.e. the thermal pressure model; Anderson 1995) is strongly encouraged. Thanks to the new experiments of Du et al. (2015), which derived the $\frac{\partial K_{0T}}{\partial T}$ values for grossular from their simultaneous PVT data, we can now compare how the adoption of these different EoS formalisms affects the calculated entrapment pressure. The calculation method here used is described in detail by Angel et al. (2014a,b). Assuming an hypothetical pure grossular included in a diamond, and a residual pressure of the inclusion of 0.5 GPa at 1500 K, using the $\frac{\partial K_{0T}}{\partial T}$ model result in a calculated pressure of 5.467 GPa, while using the thermal pressure model produce a calculate pressure of 5.741 GPa. This difference of ~ 0.3 GPa correspond to a difference in dept of formation of ~ 9 km.

A further test can be made evaluating how the calculated entrapment pressure changes with changing the grossular and uvarovite elastic parameters in the range of literature data. As a test case we considered a hypothetic garnet inclusion with a typical peridotitic composition ($Py_{79}Alm_{11}Gr_7Uv_3$), and a residual pressure of 0.5 GPa. Pyrope and

almandine parameters were taken from Milani et al. (2015). The thermo-elastic parameters of the peridotitic garnet were modeled with a weighted average. The final full set of EoS coefficients that are obtained from the calculations are reported in Table 8. The maximum difference in the calculated pressure that we observed by adopting different end-member data is ~ 0.09 GPa (i.e. 2.6 km).

Employing the pyrope and almandine data of Milani et al (2015) and the grossular uvarovite data here determined, the calculated pressure for the peridotitic garnet inclusion is 5.860 GPa. It is interesting to note that Milani et al (2015) obtained a value of 5.821 GPa for an hypothetical pure pyrope inclusion, assuming the same conditions in the calculations. This correspond to a difference of ~ 0.04 GPa (i.e. ~ 1.2 km), which highlight the strong influence of the pyrope component in the estimation of the entrapment pressure.

Table 8. Room pressure-temperature Equations of State coefficients obtained with a BM3- and thermal-*P* type-EoS for the hypothetical peridotitic garnet composition ($Py_{79}Alm_{11}Gr_7Uv_3$).

	K_{T0} (GPa)	K'	$\alpha_{303}x10^{-5}$ (K^{-1})	θ_E (K)
$Py_{79}Alm_{11}Gr_7Uv_3$	164.7	6.2	2.423(5)	369

Note: Coefficients for pyrope and almandine end-member are taken from Milani et al. (2015), while data for grossular and uvarovite are from this study.

6. Conclusions

A new set of thermo-elastic parameters of pure grossular and uvarovite single-crystals were determined by in-situ high-pressure and high-temperature single-crystal X-ray diffraction. The bulk-modulus values were obtained fitting the data to a BM3-EoS (Birch, 1947). The EoS coefficients obtained for the grossular are V_0 = 1664.39(18) Å^3, K_{T0} = 167.1(2.0) GPa and K` = 5.0(5), while for the uvarovite are: $V_0$ = 1731.07(18) Å$^3$, $K_{T0}$ = 157.9(1.8) GPa and $K$` = 5.4(5). The good agreement between our high-T data for grossular and those reported by Bosenick and Geiger (1997) for the low-T behavior on a synthetic pure grossular garnet allowed a much more reliable description of the thermal behavior of grossular from 20 K to 1073 K. The data were fitted by a Kroll-type EoS (Kroll et al. 2012), which was also used to determine the Einstein temperature (θ_E = 500 K). The

overall results will be critical not only to generally understand the variation of elastic properties of garnets within solid solutions, but also to calculate the entrapment pressures of garnet included in diamonds using the recent elastic method for diamond-inclusion geobarometry (Angel et al., 2014a,b). Furthermore, we also demonstrated that grossular and uvarovite end members do not significantly affect the calculation of the entrapment pressure for garnet inclusions in diamonds with peridotitic compositions.

Acknowledgment

This work has been supported by the ERC Starting Grant (n° 307322) to F. Nestola. We thank R.J. Angel and P. Nimis for the fruitful discussions.

References

Angel, R.J., 2000. Equations of state, in: Hazen, R.M., Downs, R.T. (Eds.), High-temperature and high-pressure crystal chemistry, Rev Mineral Geochem, vol 41, Mineralogical Society of America and the Geochemical Society, Washington DC, pp 35–39.

Angel, R.J., Finger, L.W., 2011. SINGLE: a program to control single-crystal diffractometers. J. Appl. Crystallogr. 44, 247-251.

Angel, R.J., Allan, D.R., Miletich, R., Finger, L.W., 1997. The use of quartz as an internal pressure standard in high pressure crystallography. J. Appl. Crystallogr. 30, 461-466.

Angel, R.J., Bujak, M., Zhao, J., Gatta, D., Jacobsen, S.D., 2007. Effective hydrostatic limits of pressure media for high-pressure crystallography. J. Appl. Crystallogr. 40, 26-32.

Angel, R.J., Alvaro, M., Nestola, F., Mazzucchelli, M., 2014a. Diamond thermoelastic properties and implications for determining the pressure of formation of diamond-inclusion systems. Russian Geology and Geophysics Journal. (submitted).

Angel, R.J., Mazzucchelli, M., Alvaro, M., Nimis, P., Nestola, F., 2014b. Geobarometry from host-inclusion systems: the role of elastic relaxation. American Mineralogist, in press.

Angel, R.J., Gonzalez-Platas, J., Alvaro, M., 2014c. EosFit-7c and a Fortran module (library) for equation of state calculations. Z. Krist. 229, 405-419.

Birch, F., 1947. Finite elastic strain of cubic crystals. Phys. Rev. 71, 809-824.

Bosenick, A., Geiger, C.A., 1997. Powder X ray diffraction study of synthetic pyrope-grossular garnets between 20 and 295 K. Journal of Geophysical Research 102, 22649-22657.

Du, W., Clark, S.M., Walker, D., 2015. Thermo-compression of pyrope-grossular garnet solid solutions: Non-linear compositional dependence. Am. Min., 100, 215-222.

Erba, A., Mahmoud, A., Orlando, R., Dovesi, R., 2014. Elastic properties of six silicate garnet end members from accurate ab initio simulations. Physics and Chemistry of Minerals 41, 151-160.

Fei, Y., 1995. Thermal expansion, in: Ahrens, T.J. (Ed.), Mineral Physics and Cristallography, A Handbook of Physical Constants. American Geophysical Union, Washington, DC.

Ita, J., Stixrude, L., 1992. Petrology, elasticity, and composition of the mantle transition zone. J. Geophys. Res. Solid Earth, 97, 6849–6866.

Izraeli, E.S., Harris, J.W., Navon, O. 1999. Raman barometry of diamond formation. Earth Planet. Sci. Lett., 173, 351–360.

Kawai K, Tsuchiya T., 2012. First principles investigations on the elasticity and phase stability of grossular garnet. J Geophys. Res. Solid Earth, 117, B02202.

King, H.E., Finger, L., 1979. Diffracted beam crystal centering and its application to high pressure crystallography. J. Appl. Crystallogr. 12, 374–378.

Kono, Y., Gréaux, S., Higo, Y., Ohfuji, H., Irifune, T. 2010. Pressure and temperature dependences of elastic properties of grossular garnet up to 17 GPa and 1650 K. J. Earth Sci., 21, 782–791.

Kroll, H., Kirfel, A., Heineman, R., Barbier, B., 2012. Volume thermal expansion and related thermophysical parameters in the Mg, Fe olivine solid-solution series. European Journal of Mineralogy 24, 935-956.

Leitner, B.J.,Weidner, D.J., Liebermann, R.C., 1980. Elasticity of single crystal pyrope and implications for garnet solid solution series. Physics of the Earth and Planetary Interiors 22, 111–121.

Milani S., Nestola F., Alvaro M., Pasqual D., Mazzucchelli M.L., Domeneghetti M.C., Geiger C.A., 2015. Diamond-garnet geobarometry: the role of garnet compressibility and expansivity. (submitted).

Miletich, R., Allan, D.R., Kuhs, W.F., 2000. High-pressure single crystal techniques, in: Hazen, R.M., Downs, R.T. (Eds.), High-temperature and high-pressure crystal chemistry, Rev Mineral Geochem, vol 41, Mineralogical Society of America and the Geochemical Society, Washington DC, pp 445–519.

Nestola, F., Nimis, P., Ziberna, L., Longo, M., Marzoli, A., Harris, J.W., Manghnani, M.H., Fedortchouk, Y., 2011. First crystalstructure determination of olivine in diamond: composition and implications for provenance in the Earth's mantle. Earth Planet. Sci. Lett., 305, 249–255.

Ralph, R.L., Finger, L.W., 1982. A computer program for refinement of crystal orientation matrix and lattice constraints from diffractometer data with lattice symmetry constraints. J. Appl. Crystallogr. 15, 537–539.

Ringwood, A. E.,1975. Composition and Petrology of the Earth's Mantle, McGraw-Hill, New York, 618 pp.

Salje, E.K.H., Wruck, B., Thomas, H., 1991. Order-parameter saturation and low-temperature extension of Landau theory. Zeitschrift fur Physik B Condensed Matter, 82, 399-343.

Stachel, T., Harris, J.W., 2008. The origin of cratonic diamonds – Constraints from mineral inclusions. Ore Geology Review 34, 5–32.

Skinner, B.J., 1956. Physical properties of end-members of the garnet group. American Mineralogist 41, 428–436.

Takahashi, T., Liu Lin-gun, 1970. Compression of ferromagnesian garnets and the effect of solid solutions on the bulk modulus. Journal of Geophysical Research 75, 5757–5766.

Thieblot, L., Roux, J., Richet, P., 1998. High-temperature thermal expansion and decomposition of garnets. European Journal of Mineralogy 10, 7–15.

Zhang, L., Ahsbahs, H., Kutoglu, A., Geiger, C.A., 1999. Single-crystal hydrostatic compression of synthetic pyrope, almandine, spessartine, grossular and andradite garnets at high pressures. Physics and Chemistry of Minerals 27, 52–58.

HIGH-PRESSURE BEHAVIOUR OF A SYNTHETIC ECLOGITIC GARNET

Rationale and aim of the work

As mentioned in the previous sections, thermoelastic geobarometry for estimating entrapment pressure of inclusion trapped in diamonds require precise values of the elastic properties of both diamond and inclusion. Garnet inclusions show a broad chemical variability and therefore the key point is to understand the compositional dependence of garnet elastic parameters. This can be done by determining the elastic properties of the relevant garnet end-members (see Fig. 7) thus retrieving the variation of the elastic properties within the solid solutions. The precise thermoelastic parameters of pyrope, almandine, pyrope-almandine solid solution, grossular and uvarovite as carefully determined in this work are therefore crucial for the application of the thermoelastic method to natural garnet inclusions still trapped in diamond.

Afters the elastic properties have been determined within a simple solid solution (i.e. involving only two end-members), the subsequent step is to understand how the elastic properties vary within more complex garnet solid solutions (i.e. three or more end-members), closer to that of natural garnets included in diamonds. For this reason, after the determination of the thermo-elastic parameters along different two end-members compositional joins (e.g. Manuscript 1 and 2) I performed an in-situ high-pressure single crystal X-ray diffraction experiment on a synthetic single crystal with eclogitic-like composition (i.e. $Py_{51}Al_{22}Gr_{27}$). The measured elastic properties of this complex solid solution have been compared to those calculated from the end-member elastic properties, to test if the compositional dependence of garnet elasticity can be reliably estimated assuming an ideal mixing model.

Materials and methods

The garnet, used for the experiments, kindly provided by Vincenzo Stagno, was synthesized at the Bayerisches Geoinsitut using a multi-anvil press. In order to characterize its chemical composition the sample was analysed with a Jeol electron microprobe at the Bayerisches Geoinsitut. Analytical conditions and standards used for the calibration of the electron microprobe were the same as those reported in the analytical method chapter. The compostion of this garnet can be written in terms of end-member components as $Py_{51}Al_{22}Gr_{27}$.

The high-pressure X-ray diffraction experiment was carried out at the University of Padova using a STOE STADI-IV four-circle eulerian cradle X-ray diffractometer. The diffractometer was equipped with a point detector, a MoKα radiation, operating at 50 kV and 40 mA, and automated by the SINGLE software (Angel and Finger 2011). The sample used for the high-pressure experiments was ca. 80 x 40 x 20 μm in size. The crystal was selected based on the absence of twinning and visible inclusions and on the quality of its diffraction peak profiles. The sample was loaded in an ETH-type diamond-anvil cell (Miletich et al. 2000) using a steel gasket, pre-indented to 100 - 110 μm of thickness and with a hole diameter of 230 - 250 μm. A methanol:ethanol mixture 4:1 was used as pressure transmitting medium, which remains hydrostatic up to about ~ 9.5 GPa (Angel et al. 2007; Klots et al. 2009). A single crystal of quartz was used as a pressure standard (Angel et al. 1997). The unit-cell edge was determined by centering no less than 20 reflections for each pressure step, in the 2θ range of 14°–29°. The effects of the crystal offsets and the diffractometer aberrations were removed by using the eight-position centering method (King and Finger 1979). Unconstrained unit cell parameters always confirmed the cubic symmetry within 1 e.s.d.. Constrained unit cell parameters were obtained by vector least-squares fit (Ralph and Finger 1982).

Results

The unit-cell edges and the relative unit-cell volumes for the two samples at different pressures are reported in Table 2.

Table 2
Unit-cell parameter and volume at different pressures for the eclogitic garnet ($Py_{51}Al_{22}Gr_{27}$).

P (GPa)	a (Å)	V (Å^3)
0.0001(1)	11.5874(5)	1555.797(212)
0.557(7)	11.5749(3)	1550.801(111)
1.163(9)	11.5611(3)	1545.237(134)
2.229(9)	11.5382(4)	1536.083(143)
3.388(10)	11.5140(4)	1526.419(150)
4.168(15)	11.4976(3)	1519.936(133)
5.155(10)	11.4772(4)	1511.859(144)
6.276(12)	11.4555(3)	1503.303(124)
8.257(12)	11.4199(3)	1489.297(107)

Standard deviations are given in parentheses.

As shown in Fig.29 the unit-cell volume decreases smoothly with increasing pressure up to the maximum hydrostatic pressure reached in this study of ca. 8.3 GPa. This pressure value certainly covers the range of pressure stability for upper mantle garnets.

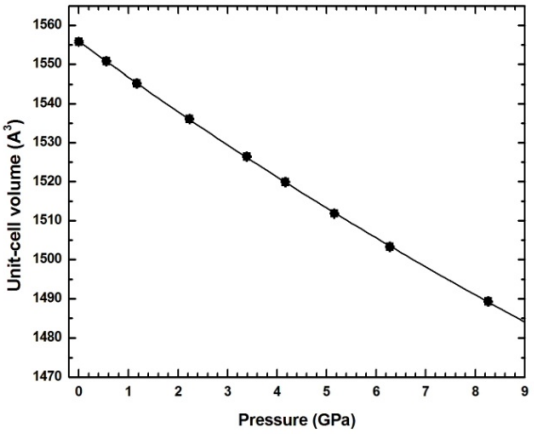

Fig. 29 - Pressure-volume behavior of the eclogitic garnet. The solid line is the Birch-Murnaghan 3rd order EoS fit to the data. The error bars are smaller than the symbol size.

Based on the F_E-f_E plot (Fig. 30) a Birch-Murnaghan equation of state truncated at the third-order (BM3-EoS, Birch 1947) was chosen to best fit the pressure-volume data. Simultaneous refinement of the BM3-EoS coefficients (volume, V_0, isothermal bulk modulus, K_{T0} and its first derivative, K_0') was possible using the program EoSFit7c (Angel et al. 2014c). The resulting coefficients are: V_0 = 1555.94(14) Å^3, K_{T0} = 166.2(1.9) GPa and K_0' = 5.7(5). The goodness of the fit results is confirmed by the low pressure shifts (ΔP_{max} = 0.031 GPa), calculated as $|P_{obs} - P_{calc}|$, and the weighted χ^2=1.33. At the same time the adequacy of the equation of state model used (i.e. 3rd order Birch-Murnaghan EoS) is confirmed by the small differences between the EoS coefficient obtained by the refinement and estimated by the F_E-f_E plot of Fig. 30, where the intercept correspond to the bulk modulus, K_{T0}, while the slope of the line correspond to the K_0'.

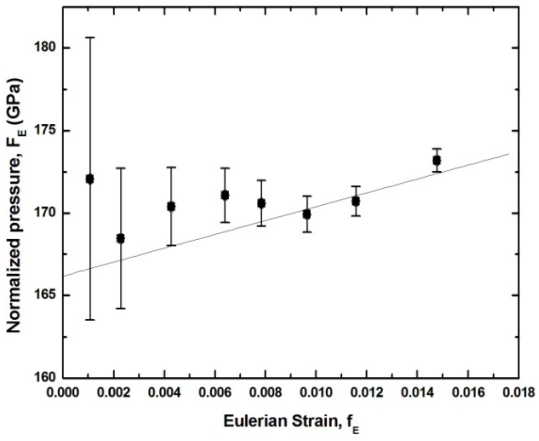

Fig. 2 - F_E-f_E plot for the eclogitic garnet. The solid line is a Birch-Murnaghan 3rd order EoS fit to the data.

Thermoelastic behaviour of the eclogitic garnet

It is well known that in nature garnet never occurs as a pure end-member and that in the majority of the cases the solid solutions are not ideal. In order to enable the application of the elastic method to calculate the entrapment pressure of garnet still trapped in a diamond, we need to determine the equation of state of the garnet inclusion, which is strongly dependent upon composition. The composition can be determined in-situ by novel X-ray diffraction techniques, which allow high-quality crystal structure refinement of the inclusion (Nestola et al. 2012). As mentioned in the introduction chapter, however, literature end-member and solid solution data do not precisely constrain the mixing properties of mantle garnets, hampering the application of the elastic method. The results of this thesis, which provide new high-quality thermoelastic parameters for mantle garnets, will be therefore fundamental to calculate reliable equations of state of garnets still trapped in diamonds. The experiment on the eclogitic garnet can be used as a test case to check whether these calculations produce elastic coefficients comparable to those measured and thus evaluate what the possibile differences means in terms of calculated entrapment pressure.

The EoS coefficients (V_0, K_0, K_0') were calculated by a weighted average of the EoS coefficients of the garnet end-member composition. Given the composition of the eclogitic-like garnet under investigation ($Py_{51}Al_{22}Gr_{27}$), the calculations were performed for a mixture of pyrope, almandine and grossular, in the molar proportion 51:22:27. The

EoS coefficients for the eclogitic-like garnet calculated by weighted average are: V_0 = 1554.90(24) Å^3; K_0 = 166.8(1.2) GPa, and K_0' = 5.9(4). The difference between the observed and calculated V_0 is about 0.1% (i.e. ca. 1.04 Å^3), while the differences in bulk modulus (K_{0T}) and its first pressure derivative (K_0') are 0.4% (i.e. 0.6 GPa) and 3.5% (i.e. 0.2), respectively.

Two set of entrapment pressures for the eclogitic-like garnet were therefore calculated, using both the observed and the extrapolated K_0 and K'. The elastic method used for these calculations is described in the introduction chapter. In both the calculations the residual pressure value of 0.5 GPa was assumed accordingly with Nestola et al. (2012). The values of thermal expansion (the same in both the calculations) were obtained by averaging the thermal expansion values for pyrope, grossular and almandine. Pyrope and grossular data were those obtained in this work, while the almandine data were obtained by fitting the high-temperature data from Skinner (1956) together with those by Bosenick and Geiger (1997) using a Kroll-type EoS. The results show that the differences between the calculated and measured K_0 and K' values produce a discrepancies in the entrapment pressures of about 0.03 GPa if the entire temperature range 1000 – 1800 K is considered (Table 2). This difference in entrapment pressures corresponds to less than 1 km in estimation of the depth of formation.

Table 2
Entrapment pressures, P_e, for a hypothetical eclogitic garnet ($Py_{51}Al_{22}Gr_{27}$) inclusion trapped in diamond (P_{inc} = 0.50) calculated using the observed bulk modulus and the calculated bulk modulus by a weighted average.

	K_{T0} observed	K_{T0} calculated
T (K)	P_e (GPa)	P_e (GPa)
300	0.998	1.001
1100	4.344	4.367
1200	4.684	4.708
1300	5.017	5.043
1400	5.345	5.372
1500	5.668	5.698
1600	5.988	6.020
1700	6.305	6.338
1800	6.620	6.655

DISCUSSIONS AND CONCLUSIONS

Determining the pressure of formation of inclusion-bearing diamonds is of fundamental importance to understand not only the diamond formation environment but also the nature and evolution of the upper mantle. As highlighted in the introduction chapter, the application of classical geobarometry on these inclusions is often not possible (due to the lack of the appropriate mineral assemblage) or, when it is applicable, produces too high uncertainties in the pressure determination. These uncertainties are due to different issues, from the phase equilibria experiments used for the calibration of the geobarometers to the application of the method to samples for which equilibrium cannot be constrained. In this respect, one of the main issues is that most of these uncertainties cannot be clearly quantified.

The elastic barometry, on the other hand, is based solely on the thermoelastic parameters of the host and the inclusion, which are known or can be determined with high precision. Moreover, the results of this work showed that the effect of the uncertainties of the thermoelastic parameters on the calculated pressure can be precisely quantified. With respect to classical geobarometry, the elastic barometry has therefore a great potential to be much more reliable in terms of the uncertainties if accurate elastic parameters of the inclusions are used. In addition, such barometry can be applied to a much larger number of diamonds as it is not strongly dependent on the composition.

Olivine and garnet-bearing diamonds constitute almost the 65 % of inclusion-bearing diamonds. Recently, the elastic barometry has been successfully applied to olivine inclusions (e.g. Nestola et al., 2011). The case of olivines, however, is relatively simple, because the range of composition of mantle olivines is very small (90-93 % forsterite), implying a small variation of the elastic behaviour. Moreover, variation of elastic properties within the olivine solid solution is ideal. Mantle garnets, on the other hand, are characterized by a wider compositional range, described by a larger number of end-members, and the mixing properties between these end-members can be not ideal. The key point of this work was therefore the determination of self-consistent set of elastic properties of the most important end-members of garnet included in diamonds (manuscript 1 and 2).

In-situ high-pressure and high-temperature single crystal X-ray diffraction experiments allowed to determine the bulk modulus of pyrope, almandine, grossular

and uvarovite and the thermal expansion of pyrope and grossular. The additional data obtained for the solid solution $Py_{60}Al_{40}$ indicate that the variation of the V_0 and bulk modulus within the almandine-pyrope solid solution is ideal. Overall, the combination of new X-ray diffraction experiments and the available literature data have been then used to constrain the behaviour of the most important garnet solid solutions.

An important step for the development of the elastic barometry for diamond-garnet pairs is to model the compositional dependence of elastic properties of garnets. This would allow the determination of the elastic properties of any garnet still trapped in a diamond if its composition is determined using a different approach (see Nestola et al. 2012). Preliminary calculations for a hypothetic pyrope-almandine garnet included in diamonds then show that the calculated entrapment pressure is strongly controlled by the pyrope component. In this hypothetic case the calculated pressure (5.821 GPa at 1500K, if a residual pressure of 0.5 GPa is assumed; see Table 2a in manuscript 1) is in good agreement with the expected pressure and temperature conditions along a typical geotherm of subcratonic lithospheric mantle sections. A further test on a hypothetical peridotitic garnet ($Py_{79}Alm_{11}Gr_7Uv_3$) confirmed the strong influence of the pyrope component in controlling the calculated pressure (5.860 GPa at 1500K, if a residual pressure of 0.5 GPa is assumed; see in manuscript 2).

An additional in-situ high-pressure single crystal X-ray diffraction experiment on a synthetic eclogitic garnet ($Py_{51}Al_{22}Gr_{27}$) revealed that simple weight average calculations can be used to model the compositional dependence of the thermoelastic parameters. The small differences observed between the calculated and measured thermoelastic parameters lead to a difference in entrapment pressure of 0.03 GPa (corresponding to 1km in depth of formation).

Thanks to the results of this study, the elastic properties of the relevant mantle garnet end-members and the behaviour within intermediate solid solutions are now better constrained. The data obtained for these garnets, listed and explained in detail in the previous chapters, will be fundamental for the application of the elastic method to determine the pressure of formation of garnet-bearing diamonds. It is important to emphasize again that the pressure calculated with this method are particularly sensible to variations in elastic parameters and therefore only the adoption of self-consistent set of data, like the one determined here, can result in low uncertainties of the estimated pressures.

However, some more data and more testing are needed before the method can be reliably applied to actual natural garnets still trapped in diamonds. Further testing is needed to verify if weight average calculations can be used to model the elastic behaviour of natural garnets. Additional high-temperature single-crystal X-ray diffraction experiments need to be carried out in order to determine the expansivity of pure almandine and uvarovite and solid solutions reproducing eclogitic and peridotitic garnets. These data will be used to understand if also the thermal expansion can be modelled by weight average calculations.

REFERENCES

- Adams DM, Christy AG (1992) Materials for high temperature diamond anvil cells. High Press Res 8:685-689.
- Adams HG, Cohen LH, Rosenfeld JL (1975) Solid inclusion piezomethry I: comparison dilatometry. Am Mineral 60:574-583.
- Allan DR, Miletich R, Angel RJ (1996) A diamond-anvil cell for single X-ray diffraction studies to pressures in excess of 10 GPa. Rev Sci Instrum 67: 840-842.
- Alvaro M, Angel RJ, Marciano C, Milani S, Zaffiro G, Scandolo L, Mazzucchelli ML, Rustioni G, Domeneghetti MC, Nestola F (2015) Development of a new micro-furnace for “in situ” high-temperature single crystal X-ray diffraction measurements. (in prep).
- Angel RJ, Finger LW (2011) SINGLE: a program to control single-crystal diffractometers. J Appl Crystallogr 44:247-251.
- Angel RJ, Allan DR, Miletich R, Finger LW (1997) The use of quartz as an internal pressure standard in high pressure crystallography. J Appl Crystallogr 30:461-466.
- Angel RJ, Bujak M, Zhao J, Gatta D, Jacobsen SD (2007) Effective hydrostatic limits of pressure media for high-pressure crystallography. J Appl Crystallogr 40:26-32.
- Angel RJ, Alvaro M, Nestola F, Mazzucchelli M (2014a) Diamond thermoelastic properties and implications for determining the pressure of formation of diamond-inclusion systems. Russian Geol Geophys J. (in press).
- Angel RJ, Mazzucchelli M, Alvaro M, Nimis P, Nestola F (2014b) Geobarometry from host-inclusion systems: the role of elastic relaxation. Am Mineral 99: 2146-2149.
- Angel, R.J., Gonzalez-Platas, J., Alvaro, M., 2014c. EosFit-7c and a Fortran module (library) for equation of state calculations. Zeit Kristall 229: 405-419.
- Angel RJ, Nimis P, Mazzucchelli M, Alvaro M, Nestola F (2015) How large are departures from lithostatic pressure? Constraints from host-inclusion elasticity, J Met Geol (submitted).
- Barron LM, Mernagh TP, Barron BJ (2008) Using strain birefringence in diamond to estimate the remnant pressure on an inclusion. Aust J Earth Sci 55:159-165.
- Birch, F., 1947. Finite elastic strain of cubic crystals. Phys Rev 71: 809-824.
- Bleeker W (2003) The late Archean record: a puzzle in ca. 35 pieces. Lithos 71: 99-134.

- Boyd FR, England JL (1960) Apparaturs for phase-equilibrium measurements at pressures up to 50 kilobars and temperatures up to 1750˚C. J Geophys Res 65:741-748.
- Ca´mara F, Gatta D, Meven M, Pasqual D (2012) Thermal expansion and high temperature structure evolution of zoisite by single crystal X-ray and neutron diffraction. Phys Chem Minerals 39:27–45.alvaro
- Canil D, Fedortchouk Y (1999) Garnet dissolution and the emplacement of kimberlites. Earth Planet Sci Lett 167: 227–237.
- Creighton S, Stachel T, Matveev S, Höfer HE, McCammon C, Luth RW (2009) Oxidation of the Kaapvaal lithospheric mantle driven by metasomatism. Contrib Mineral Petrol 157:491–504.
- Dobrzhinetskaya LF (2012) Microdiamonds − Frontier of ultrahigh-pressure metamorphism: A review. Gondwana Res 21:207-223.
- Dunstan DJ (1989) Theory of the gasket in high-pressure diamond anvil cells. Rev Sci Instrum 60: 3789-3795.
- Ernst WG (2001) Subduction, ultrahigh-pressure metamorphism, and regurgitation of buoyant crustal slices — implications for arcs and continental growth. Phys Earth Planet Int 127: 253-275.
- Eckstrand OR, Sinclair WD, Thorpe RI (1995) Geology of Canadian Mineral Deposit Types: Geological Survey of Canada, Geology of Canada, no. 8.
- Frondel C, Marvin UB (1967) Lonsdaleite, a hexagonal polymorph of diamond. Nature 214: 587-589.
- Goodier JN (1933) Concentration of stress around spherical and cylindrical inclusions in minerals. T Am Soc Mech Eng 39-44.
- Grutter HS, Gurney JJ, Menzies AH, Winter F (2004) An updated lassification scheme for mantle-derived garnet, for use by diamond explorers. Lithos 77: 841-857.
- Grutter HS, Latti D., Menzies A (2006) Cr-saturation arrays in concentrate garnet compositions from kimberlite and their use in mantle barometry. J Pet 47: 801-820.
- Gurney JJ, Harris JW, Rickard RS (1984) Minerals associated with diamonds from the Roberts Victor MineIn: KimberlitesII:The mantle and crust-mantle relationships. Kornprobst J (ed) Elsevier., Amsterdam, Netherlands (NLD), p 25-32.
- Gurney JJ, Helmstaedt HH, Richardson SH, Shirey SB (2010) Diamonds through time. Econ Geol 105:689-712.

- Hall HT (1958) Some high-pressure, high-temperature apparatus design considerations: Equipment for use at 100000 atmospheres and 3000 °C. Rev Sci Instrum, 29:267-275.
- Harlow GE, Davies RM (2005) Diamonds. Elements 1: 67-70, doi: 10.2113/gselements.1.2.67.
- Harris JW (1968) The recognition of diamond inclusions. Part 2: epigenetic mineral inclusions. Industrial Diamond Review 28: 558–561.
- Harris JW, Henrique R, Meyer HOA (1967) Orientation of silicate mineral inclusions in diamonds. Crystal Growth 7: 118–123.
- Harris JW, Milledge HJ, Barron THK, Munn RW (1970) Thermal expansion of garnets included in diamond. J Geophys Res 75:5775-5792.
- Harte B (2010) Diamond formation in the deep mantle; the record of mineral inclusions and their distribution in relation to mantle dehydration zones. Mineral Mag 74:189-215.
- Harte B, Harris JW, Hutchison MT, Watt GR, Wilding MC (1999) Lower mantle mineral associations in diamonds from Sao Luiz, Brazil. *In:* Mantle Petrology; Field Observations and High-Pressure Experimentation: A Tribute to Francis R. (Joe) Boyd. Fei Y, Bertka CM, Mysen BO (eds) Geochemical Society−University of Houston, Department of Chemistry, Houston, Texas, p 125-153.
- Hazen, R. M. (1983) Zeolite molecular sieve 4A: Anomalous compressibility and volume discontinuities at high pressure. Science 219: 1065–1067.
- Hazen RM, Finger LW (1982) Comparative crystal chemistry. Wiley, New York, 231 p.
- Howell D, Wood IG, Dobson DP, Jones AP, Nasdala L, Harris JW (2010) Quantifying strain birefringence halos around inclusions in diamond. Contrib Mineral Petrol 160:705-717.
- Howell D, Wood IG, Nestola F, Nimis P, Nasdala L (2012) Inclusions under remnant pressure in diamond: A multi-technique approach. Eur J Mineral 24:563-573.
- Izraeli ES, Harris JW, Navon O (1999) Raman barometry of diamond formation. Earth Planet Sci Lett 173: 351–360.
- Jamieson JC, Lawson AW, Nachtrieb ND (1959) New Device for obtaining X-Ray Diffraction Patterns from Substances Exposed to High Pressure. Rev Sci Instrum 30:1016-1019.

- Kawai N, Togaya M, Onodera A (1973) A new device for pressure vessels. Proc Jpn Acad 49:623-626.
- Kawai N, Endo S (1970) The generation of ultrahigh hydrostatic pressures by a split sphere apparatus. Rev Sci Instrum 41:1178-1181.
- Keppler H, Frost D (2005) Introductio to minerals under extreme conditions. EMU Notes in Mineralogy 7:1-30.
- King HE, Finger LW (1979) Diffracted beam crystal centering and its application to high-pressure crystallography. J Appl Crystallogr 12:374-378.
- Klotz S, Chervin J-C, Munsch P, Marchand GL (2009) Hydrostatic limits of 11 pressure transmitting media. Journal of Physics D: Applied Physics 42: 075413.
- Kopylova MG, Rickard RS, Kleyenstueber A, Taylor WR, Gurney JJ, Daniels LRM (1997) First occurrence of strontian K–Cr-loparite and Cr-chevkinite in diamonds. Geologiya i Geofizika 38: 382–397.
- Kopylova M, Navon O, Dubrovinsky L, Khachatryan G (2010) Carbonatitic mineralogy of natural diamondforming fluids. Earth Planet Sci Lett 291:126-137.
- Lee, Y., Vogt, T., Hriljac, J. A., Parise, J. B., Hanson, J. C. & Kimk, S. J. (2002) Non-framework cation migration and irreversible pressure-induced hydration in a zeolite. Nature (London), 420: 485–489.
- Li J, Hadidiacos C, Mao HK, Fei Y, Hemley RJ (2003) Behavior of thermocouples under high pressure in a multi-anvil apparatus. High Pressure Res 23:389-401.
- Lowell J, Navrotsky A, Holloway JR (1971) Synthesis of uvarovite using a sodium-potassium-borate flux. J Am Ceram Soc 54:466.
- Mao HK, Bell PM (1980) Design and operation of a diamond-window, high-pressure cell for the study of single-crystal samples loaded cryogenically. Carnegie Inst Wash Yrbk 79: 409-411.
- McCammon C (2001) Deep diamond mysteries. Science 293:813-814.
- Merril L, Bassett WA (1974) Miniature diamond anvil pressure cell for single-crystal X-ray diffraction studies. Rev Sci Instrum 45: 290-294.
- Meyer HOA (1968) Chrome pyrope — an inclusion in natural diamond. Science 160: 1446–1447.
- Meyer HOA (1987) Inclusions in diamond. In: Nixon, P.H. (Ed.), Mantle xenoliths. John Wiley & Sons Ltd., Chichester, pp. 501–522.

- Meyer HOA, Boyd FR (1969) Mineral inclusions in diamonds. Carnegie Institute Washington Yearbook 67: 1446–1447.
- Miletich R, Allan DR, Kuhs WF (2000) High-pressure single crystal techniques, in: Hazen, RM, Downs RT (Eds), High-temperature and high-pressure crystal chemistry, Rev Mineral Geochem, vol 41, Mineralogical Society of America and the Geochemical Society, Washington DC, pp 445–519.
- Mitchell RS, Giardini AA (1953) Oriented olivine inclusions in diamond. Am Mineral 38: 136–138.
- Nasdala L, Brenker FE, Glinnemann J, Hofmeister W, Gasparik T, Harris JW, Stachel T, Reese I (2003) Spectroscopic 2D-tomography; residual pressure and strain around mineral inclusions in diamonds. Eur J Mineral 15:931-935.
- Nemeth P, Garvie LAJ, Aoki T, Dubrovinskaia N, Dubrovinsky L, Buseck PR (2014) Lonsdaleite is faulted and twinned cubic diamond and does not exist as a discrete material. Nature Commun 5, doi: 10.1038/ncomms6447.
- Nestola F, Nimis P, Ziberna L, Longo M, Marzoli A, Harris JW, Manghnani MH, Fedortchouk Y (2011) First crystal-structure determination of olivine in diamond; composition and implications for provenance in the Earth’s mantle. Earth Planet Sci Lett 305:249-255.
- Nestola F, Merli M, Nimis P, Parisatto M, Kopylova M, De Stefano A, Longo M, Ziberna L, Manghnani M (2012) In situ analysis of garnet inclusion in diamond using single-crystal X-ray diffraction and X-ray micro-tomography. Eur J Mineral 24: 599-606.
- Nimis P (2002) The pressures and temperatures of formation of diamond based on thermobarometry of chromian diopside inclusions. Can Mineral 40:871–884.
- Nimis P, Taylor WR (2000) Single clinopyroxene thermobarometry for garnet peridotites. Part I. Calibration and testing of a Cr-in-Cpx barometer and an enstatite-in-Cpx thermometer. Contrib Mineral Petrol 139: 541-554.
- Orlov YL (1977) The mineralogy of the diamond. John Wiley and Sons, NewYork. 235 pp.
- Ozima M, Igarashi G (2000) The primordial noble gases in the Earth; a key constraint on Earth evolution models. Earth Planet Sci Lett 176:219-232.
- Pearson DG, Shirey SB, Harris JW, Carlson RW (1998) Sulphide inclusions in diamonds from the Koffiefontein kimberlite, S Africa; constraints on diamond ages and mantle Re-Os systematics. Earth Planet Sci Lett 160:311-326.

- Periotto B, Nestola F, Balic-Zunic T, Angel RJ, Miletich R, Olsen LA (2011) Comparison between beryllium and diamond-backing plates in diamond-anvil cells: Application to single-crystal x-ray diffraction high-pressure data. Rev Sci Instrum 82: 055111.
- Ralph RL, Finger LW (1982) A computer program for refinement of crystal orientation matrix and lattice constraints from diffractometer data with lattice symmetry constraints. J Appl Crystallogr 15:537-539.
- Richardson SH, Gurney JJ, Erlank AJ, Harris JW (1984) Origin of diamonds in old enriched mantle. Nature 310:198-202.
- Rohrbach A, Schmidt MW (2011) Redox freezing and melting in the Earth’s deep mantle resulting from carboniron redox coupling. Nature 472:209-214.
- Rosenfeld JL, Chase AB (1961) Pressure and temperature of crystallization from elastic effects around solid inclusions in minerals?. Am J Sci 259: 519-541.
- Ryan CG, Griffin WL, Pearson NJ (1996) Garnet geotherms: pressure temperature data from Cr-pyrope garnet xenocrysts in volcanic rocks. J Geophy Res 101: 5611-5626.
- Schrauder M, Navon O (1994) Hydrous and carbonatitic mantle fluids in fibrous diamonds from Jwaneng, Botswana. Geochim Cosmochim Acta 58:761-771.
- Shirey SB, Richardson SH (2011) Start of the Wilson cycle at 3 Ga shown by diamonds from subcontinental mantle. Science 333:434-436.
- Shirey SB, Richardson SH, Harris JW (2004) Integrated models of diamond formation and craton evolution. Lithos 77:923-944.
- Shirey SB, Cartigny P, Frost DJ, Keshav S, Nestola F, Nimis P, Pearson DG, Sobolev Nv, Walter MJ (2013) Diamonds and the geology of mantle carbon. Rev Mineral Geochem 75:355-421.
- Simakov SK (2008) Garnet–clinopyroxene and clinopyroxene geothermobarometry of deep mantle and crust eclogites and peridotites. Lithos 106:125–136.
- Sobolev NV, Shatsky VS (1990) Diamond inclusions in garnets from metamorphic rocks: a new environment for diamond formation. Nature 343:742-746.
- Sobolev NV, Lavrent’ev Y, Pospelova LN, Sobolev EV (1969) Chrome pyropes from the diamonds of Yakutia. Dokl Akad Nauk 189:162-165.

- Sobolev NV, Bartoshinsky ZV, Yefimova ES, Lavrent'yev YG, Pospelova LN (1970) Association of olivine, garnet and chrome-diopside from Yakutian diamonds (in Russian). Doklady Akademii Nauk SSSR 192:1349–1353.
- Stachel T, Brey GP, Harris JW (2005) Inclusions in sub-lithospheric diamonds; glimpses of deep earth. Elements 1:73-87.
- Stachel T, Harris JW (2008) The origin of cratonic diamonds - constraints from mineral inclusions. Ore Geol Rev 34:5-32.
- Stachel T, Harris JW (2009) Formation of diamond in the Earth’s mantle. J Phys Condens Mat 21:364206.
- Takahashi E, Shimazaki T, Tsuzaki Y, Yoshida H (1993) Melting study of a peridotite KLB-1 to 6.5 GPa, and the origin of basaltic magmas. Phil Trans R Soc Lond A 342:105-120.
- Torquato S (2002) Random heterogeneous materials: microstructure and macroscopic properties. Springer-Verlag, New York.
- Tuttle OF (1949) Two pressure vessels for silicate-water studies. Geol Soc Am Bull 60:1727-1729.
- Tuttle OF, Bowen NL (1958) Origin of granite in the light of experimental studies in the system NaAlSi3O8-KAlSi3O8-SiO2-H2O. Mem Geol Soc Am 74:1-145.
- Vos WL, Schouten JA (1991) On the temperature correction of the ruby pressure scale. J Appl Phys 69: 6744-6746.
- Walter MJ, Kohn SC, Araujo D, Bulanova GP, Smith CB, Gaillou E, Wang J, Steele A, Shirey SB (2011) Deep mantle cycling of oceanic crust; evidence from diamonds and their mineral inclusions. Science 334:54-57.
- Weir CE, Lippincott ER, Van Valkenburg A, Bunting EN (1959) Infrared studies in the l-to-15 micron region to 30,000 atmospheres. J Res Natl Bur Stand, Sec. A 63:55-62.
- Wilson L, Head JW (2007) An integrated model of kimberlite ascent and eruption. Nature 447: 53-57.
- Yamanaka T, Fukuda T, Hattori T, Sumiya H (2001). New diamond anvil cell for single-crystal analysis. Rev Sci Instr 72:1458-1462.
- Zhang Y (1998) Mechanical and phase equilibria in inclusion-host system. Earth Planet Sci Lett 157: 209-222.

APPENDIX A

Equations of State (EoS)

The Equations of State (EoS) define the relationship of the volume or density to intensive variables. Usually the EoS is used to describe the variation of the volume of a material with pressure or temperature. The EoS that describes the variation of the volume with pressure can be isothermal or adiabatic and they describe the change in elastic properties of a material with pressure. While thermal EoS describes the variation of the volume with temperature. The EoS are useful to determine the behaviour of minerals in the deep Earth either defining the variation of the density of a mineral with P and T or the change in seismic velocities, thus allowing to predict mineral assemblages and their stability in the Earth's interior (Fig. 1A). More particularly, by means of high-pressure and high-

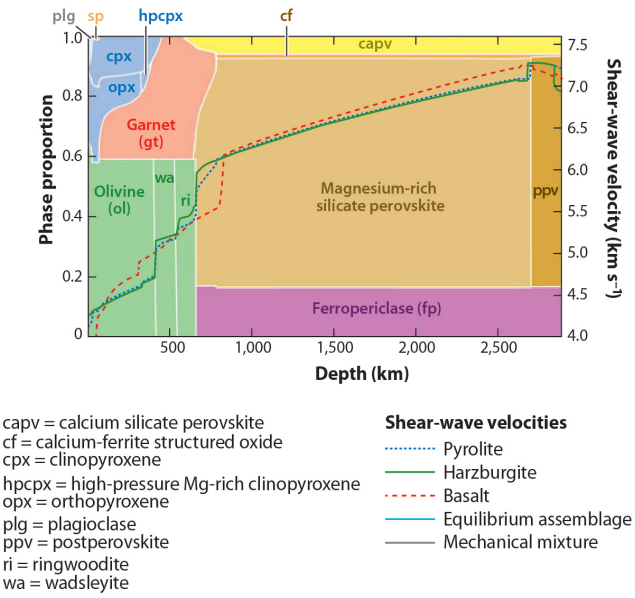

Fig. 1A – Calculated phase proportions in a pyrolitic mantle. Superimposed are the shear-wave velocities of pyrolite (modified after Stixrude and Lithgow-Bertelloni, 2012).

temperature experiments we can bracket phase transitions, determine softening mechanism due to changes in mineral structures and better describe cation partitioning. In last few decades the EoS have been also used to determine the pressure at which a mineral inclusion has been trapped in a mineral host. The derivation of EoS for solids material has been extensively discussed in several scientific manuscripts (e.g.

Anderson, 1995; Duffy and Wang, 1998; angel et al., 2000). Hereafter only a short introduction will be presented. It is important to remind the reader that there is no absolute thermodynamic basis for specifying the correct form of the EoS to be used for solids. All the developed and widespread EoS are based upon a number of assumptions. The validity of these assumptions can only be judged if the EoS used for our purposes fits well or not the measured experimental data.

Isothermal EoS

In all the experiments presented in this thesis the adopted EoS was the isothermal Birch-Murnaghan, because it is the EoS that describe better natural Earth solids. The other most used isothermal EoS are Murnaghan, Tait, Natural Strain, and Vinet (Angel et al., 2014). All these EoS are parameterized fits to P-V data, almost always in terms of the Bulk Modulus, K, that gives us some information about the stiffness of a material, and its pressure derivatives, K' and K'' i.e. :

$$K = -V(\partial P/\partial V); \qquad K' = (\partial K/\partial P); \qquad K'' = (\partial^2 K/\partial P^2)$$

These EoS are derived from the concept of a choice of the finite strain definition or inter-atomic potentials. The Murnaghan EoS (Murnaghan, 1937) is derived from the concept of finite strain. This EoS is the most widespread because it has the simplest formulation. Therefore it can be derived from the assumption that the bulk modulus is linearly related to the pressure. This permits the algebraic solution of P in terms of V and vice versa. It is mostly used to calculate metamorphic phase equilibria and it can be applied only to small compressions up to about 10%. It fails for higher amount of compression, because it has a constant K' and a $K''=0$ (Angel et al., 2014). The modified Tait EoS by Huang and Chow (1974) is a generalized form of the Murnaghan EoS, as demonstrated by Freund and Ingalls (1989). For this reason this EoS is easily invertible. The Birch-Murnaghan EoS (Birch 1947) assumes that the compressional strain energy of a solid is describable as a Taylor series expansion of the finite Eulerian strain, f_E (see below for further details). The Natural Strain EoS developed by Poirier and Tarantola (1998) is based on the “natural” or “Hencky” measure of linear strain. Because the finite-strain EoS do not accurately represent the volume variation for solids under very high compression, Vinet et al. (1986, 1987) developed an EoS from a general inter-atomic

potential. This EoS, in addition to accurately fit data at high pressure, it is excellent for simple solids. For this reason expansions of this EoS to include a refineable *K″* are not needed, at least if no phase transition occurs and it is not intended for complex materials with significant degrees of internal structural freedom such as bond-banding (Jeanloz, 1988).

Birch-Murnaghan EoS

As mentioned above the Birch-Murnaghan EoS is a 'finite strain EoS (Birch, 1947), derived from the assumption that the strain energy of a solid undergoing compression can be expressed as a Taylor series in the finite Eulerian strain (f_E). The Eulerian strain is defined as:

$$f_E = \left[\left(V_{0T}/V_{PT}\right)^{2/3} - 1\right]/2$$

The full expression of the Birch-Murnaghan EoS to 4th-order is:

$$P = 3K_{0T} f_E \left(1+2f_E\right)^{5/2}\left(1+\frac{3}{2}\left(K'_{0T}-4\right)f_E + \frac{3}{2}\left(K_{0T}K''_{0T} + \left(K'_{0T}-4\right)\left(K'_{0T}-3\right) + \frac{35}{9}\right)f_E^2\right)$$

In this way the EoS has non-zero coefficients of f_E^2 and yields a four-parameter EoS (V_0, K_0, K_0', K_0''). This equation of state can be truncated to the second or third order in energy depending on the fit of the data. The truncation to the third order implies zero coefficients of f_E^2 and we will obtain a three-parameter EoS (V_0, K_0, K_0'). For the second order truncation the coefficient of f_E will be set to zero and K' will be fixed to four and higher order terms are ignored. The advantages of this EoS are: fits correctly P-V data for V/V_0 to 0.8, provides correct K_0, and it is convenient to fit P-V data for crust and mantle materials. Unfortunately this EoS cannot be inverted, the V∂P integrals must be numerical, and it is problematic for thermodynamic databases.

Recently it has been found that the Birch-Murnaghan and Tait EoS to P-V data normally give indistinguishable parameters within the uncertainties, but the Birch-Murnaghan EoS typically having marginally better formal measures of statistical fit (Angel et al., 2014). Moreover, the 4th-order fits of the two equations are usually indistinguishable from the statistical and numerical point of view (Angel et al., 2014).

Thermal EoS

While high-P methods and techniques have been extensively developed in the past century, high-T ones did not undergo substantial improvements. As a matter of fact, nowadays common single-crystal X-Ray diffraction high-T in situ experiment allows to reach temperature of about 1200 K with temperature stabilities and uncertainties of about 20-30 K at the highest T.

The thermal expansion of a material is defined as:

$$\alpha(T) = V^{-1}\left(\partial V/\partial T\right)_P$$

Where the integration of this expression gives the variation of the volume with temperature at a constant pressure:

$$V_{0T} = V_{00}\exp\int_{T_{ref}}^{T}\alpha(T)dT$$

As highlighted by Angel et al. (2014), to which the reader is referred for a complete review, the equation for α(T) are that $\frac{\partial\alpha}{\partial T}$ = 0 at absolute zero is the only thermodynamic constraint for the determination of the thermal expansion. For this reason, depending on the results of the fitting to the experimental data, different authors proposed different equations of state to describe the thermal behaviour of Earth's material.

In this work, three equations of state have been used. The Fei Eos has been used to compare the obtained values with literature data. The Salje EoS has been used to fit the low temperature data to obtain the saturation temperature and the Kroll EoS was useful to fit the data at low and high temperature and therefore obtain a more reliable description of the thermal behaviour of the sample.

Fei EoS

For purpose of comparison with the earlier literature data the thermal EoS proposed by Fei (1995) has been used. As explained in Angel et al (2014) what Fei (1995) proposed is an expansion of the earlier Berman (1988) EoS expression to $\alpha = \alpha_0 + \alpha_1 T + \alpha_2 T^{-2}$ (with *T* in Kelvin). This leads to the high-temperature volume at zero pressure given as:

$$V_{0T} = V_{00} \exp\left(\alpha_0 (T - T_{ref}) + \frac{1}{2}\alpha_1 \left(T^2 - T_{ref}^2\right) - \alpha_2 \left(\frac{1}{T} - \frac{1}{T_{ref}} \right) \right)$$

With this formulation, the actual values of α_0, α_1 and α_2 that describe a *V-T* curve are those at 0K, and *not* those at T_{ref}, so their values are independent of T_{ref}. It also has the advantage that the derivative $\frac{1}{V_{0T}} \frac{\partial V_{0T}}{\partial T}$ is exactly $\alpha = \alpha_0 + \alpha_1 T + \alpha_2 T^{-2}$ at all temperatures. The disadvantage is that the full expression predicts non-physical behaviour at low temperatures because the term T^{-2} causes the value of α to diverge towards infinity as *T* approaches 0K. If $\alpha_2 = 0$ the simplified form $\alpha = \alpha_0 + \alpha_1 T$ remains mathematically valid at all temperatures although it does not yield $\alpha = 0$ at *T* = 0K.

Salje EoS

In order to obtain reliable estimate of the Einstein temperature (θ_E) for performing fitting that includes the low T regime Salje et al. (1991) proposed an equation of state that address the saturation of thermal expansion at low temperature:

$$V_{0T} = \left[p_0 + p_1 \theta_{sat} \coth\left(\theta_{sat}/T\right) \right]^3$$

in which θ_{sat} is termed the "saturation temperature". In fact the thermal expansion coefficient only becomes zero below $T \approx \theta_{sat}/10$. At moderate temperatures, above about $3\theta_{sat}$ (θ_{sat} is typically 200-500K), the thermal expansion becomes almost independent of temperature, which is not observed for most materials.

Kroll form of Holland-Powell 2011

As extensively discussed in Angel et al (2014) it is clear that simple expressions in temperature for the thermal expansion coefficient do not simultaneously meet the thermodynamic requirement $\alpha(T) = \partial\alpha/\partial T = 0$ at *T* = 0 and match the experimental observation that $\alpha(T)$ becomes linear with temperature at high temperatures. The solution originally proposed by Kumar (2003, and references therein) and re-assessed and discussed by Kroll et al. (2012) make use of an equation for thermal expansion that

explicitly relates the volume to lattice energy of the material. The main disadvantage of the Kumar thermal expansion is that it is referenced to absolute zero. Holland and Powell (2011) developed a similar function that is expressed in terms of parameters at a reference temperature. Although this formulation is not quite as robust in extrapolation as the Kumar expression when the underlying data are sparse, if the data are sufficient it produces fits and parameters that are indistinguishable from those of the Kumar equation (Kroll *et al.*, 2012). Tribaudino et al. (2011) and Kroll et al. (2012) give different but equivalent expressions, of which the latter is perhaps clearer:

$$V_{0T} = V_{00}\left[-K'_{00} + \left(1 + K'_{00}\right)\left(1 - \frac{K'_{00}\left(K'_{00}+2\right)}{\left(K'_{00}+1\right)}A\right)^{B}\right]$$

The two expressions for *A* and *B* are:

$$A = \alpha_{0,Tref}\left(\frac{\theta_E}{C}\right)\left(\frac{1}{\exp\left(\theta_E/T\right)-1} - \frac{1}{\exp\left(\theta_E/T_{ref}\right)-1}\right)$$

$$B = -1/K'_{00}\left(K'_{00}+2\right)$$

In the expression for *A*, the factor $C = \frac{\left(\theta_E/T_{ref}\right)^2 \exp\left(\theta_E/T_{ref}\right)}{\left(\exp\left(\theta_E/T_{ref}\right)-1\right)^2}$. The Einstein temperature, θ_E, in the *coth* functions provides the saturation at low temperatures, below $T \approx \theta_E/10$. The value of α_0 is the thermal expansion coefficient at T_{ref}. The value of θ_E can be approximated from the molar standard state entropy (e.g. Holland & Powell, 2011), but tests indicate that its precise value is not critical for the correct description of the volume variation with temperature and, consequently, it normally cannot be reliably determined by refinement to data.

P-V-T equations of state

A P-V-T equation of state describes the simultaneous variation of volume of a phase with pressure and temperature. This can be described by combing any thermal expansion model with any isothermal equation of state, and a model of the variation of

bulk modulus with temperature at room pressure, $\partial K_{0T}/\partial T$. A fisrt approach is to assume K0/T constant, but this lead to non-physical negative thermal expansion coefficients. Hellfrich and Connolly (2009), on the other hand, proposed an alternative method based on the definition of the Anderson-Gruneisen parameter. An additional method, which has been adopted in this work, is instead based on the concept of thermal pressure (e.g. Anderson 1995). As noted by Angel et al (2014) this method yields indistinguishable *P*-*V*-*T* relationships and also avoids negative values of thermal expansion.

Thermal Pressure

Combined low- and high-temperature data are fitted with a Kroll-type EoS (Kroll et al., 2012). The Kroll-type EoS gives a good description of the thermal expansion behavior over a large temperature range and it is needed to make calculations of P_e for diamond-inclusion pairs. In the Kroll-type EoS the Einstein temperatures, θ_E, is a paramount parameter. The Einstein temperature is calculated from the saturation temperature, T_{sat}, which is about one half of that of θ_E, as obtained from fitting just the low-*T* data set using a Salje-type EoS (Salje et al., 1991).

As described in Angel et al. (2014) the idea of thermal pressure (e.g. Anderson, 1995) is that the total pressure at a given *V* and *T* can be expressed as the sum of two terms:

$$P(V,T) = P(V,T_{ref}) + Pth(T)$$

The function $P(V,T_{ref})$ is the isothermal equation of state for the material at the reference temperature, but using the 'observed' volume from *P* and *T*. The thermal-pressure function $Pth(T)$ is the pressure that would be created by increasing the temperature from T_{ref} to *T* at constant volume at room pressure. The thermal pressure at T_{ref} is thus zero, so at T_{ref} the thermal-pressure EoS reduces to the isothermal EoS. The thermal pressure at other temperatures clearly depends on the bulk modulus. The inverse problem of determining *V* at a given *P* and *T* consists of calculating the $Pth(T)$, and then solving the isothermal EoS at T_{ref} to find *V* for an 'effective pressure' equal to $P(V,T_{ref}) = P(V,T) - Pth(T)$.

Fitting isothermal and thermal EoS

In order to fit an EoS one of the variables has to be set as dependent and the others are chosen as independent variables. Experimentally it would be obvious to set as a dependent variable the volume on the independent variables of pressure and temperature. Therefore to determine the coefficient of the EoS one would expect to fit volume to pressure and temperature. All the equations can be written in the form *P = f (V, T) or P = f (η, T*). The 'least squares' method is the best method to estimate the EoS parameters, if the experimental uncertainties are uncorrelated and normally distributed. For high-pressure experiments the number of data is not large to define a 'proper' normal distribution of the uncertainties. For this reason the uncertainties have to be estimated correctly and the outliers in the dataset have to be excluded. The experiment and the instrument have to be designed carefully to avoid any systematic error in the dataset.

The process of least squares attempts to minimize the weighted-chi squared value of:

$\chi^2_{w\,?} = \frac{1}{n-m} \sum_i^n w_i \left(P_{obs,j} - EoS\left(V_{obs,j}, T_{obs,j}\right)\right)^2$ (nn)

, where *m* is the number of parameters refined and *n* is the number of data points, each with a weight w_i defined through the effective variance method by:

$w_i = \sigma_i^{-2} = \sigma_P^{-2} + \sigma_V^{-2}.\left[\left(\frac{\partial P}{\partial V}\right)_T\right]^{-2} + \sigma_T^{-2}.\left[\left(\frac{\partial P}{\partial T}\right)_V\right]^{-2}$ ()

In general this method leads to the V_0 and K_0 parameters displaying the largest influence on the data fit, and thus should always be the first values refined before other terms are added to the EoS (Angel 2000). The value obtained of the weighted chi-square, χ^2_w, provides also a measure of the goodness of the fit. If the χ^2_w = 1 indicates that the uncertainties have been correctly assessed, that the obtained EoS parameters fit correctly the dataset, and that the refinement has converged. A value of χ^2_w < 1.0 has no statistical meaning and does not represent a better fitting to the data, it could suggest that the uncertainties of the data have been overestimated. While a value of χ^2_w > 1 suggests that the EoS does not represent the dataset and its uncertainties (Angel,

2000). This could be due to an incorrect EoS model, the uncertainties of the data underestimated or a few data-points having the wrong values.

As mentioned above the Birch-Murnaghan can be truncated to a second, third or fourth order, adding more coefficient to the fit of an EoS. The order at which the curve must be truncated cannot be evaluated looking at the P-V plot (e.g. Fig.). The visual evaluation of the Birch-Murnaghan EoS is done by the F-f plot, which can be applied to any isothermal EoS based upon finite strain. For the Birch-Murnaghan EoS the finite strain is based upon the Eulerian definition, while the F is a 'normalised pressure' and it is defines as:

$$F = \frac{P}{3f_E\left(1+2f_E\right)^{5/2}}$$

The PV data are transformed into f_E and F_E and plotted as f on the abscissa (Fig.). This leads to a quick method of assessing the appropriate order for truncation of the EoS: 2nd order fit for data plotted as a horizontal straight line, 3rd order for data plotted on a non-horizontal linear line, and 4th order or higher for data plotted on a parabolic curve (Fig.). From this diagram we also can have an indication of the compressional behaviour of our material, because the intercept on the F axis gives the value of K_0 and the K_0' is equal to the inclination of the straight line. The associated uncertainties in f_E are typically so small that they are ignored and those of F vary inversely with pressure so inherently decrease as the pressure increases.

APPENDIX B

Table 1B: Calculated and weighed amounts of the powders used for the uvarovites synthesis (first experiment).

Oxides	calculated (g)	weighed (g)	flux	calculated (g)	weighed (g)
$CaCO_3$	1.07	1.07	Na_2CO_3	0.24	0.24
Cr_2O_3	0.54	0.54	K_2CO_3	0.32	0.32
SiO_2	0.64	0.65	H_3BO_3	0.19	0.19

Table 2B: Calculated and weighed amounts of the powders used for the uvarovites synthesis.

Oxides	calculated (g)	weighed (g)	flux	calculated (g)	weighed (g)
$CaCO_3$	1.35	1.35	Na_2CO_3	0.32	0.32
Cr_2O_3	0.68	0.68	K_2CO_3	0.42	0.42
SiO_2	0.81	0.81	H_3BO_3	0.49	0.49

Table 3B: Calculated and weighed amounts of the powders used for the uvarovites synthesis.

Oxides	calculated (g)	weighed (g)	flux	calculated (g)	weighted (g)
$CaCO_3$	1.35	1.35	$Li_2B_4O_7$	0.75	0.76
Cr_2O_3	0.68	0.68	-	-	-
SiO_2	0.81	0.82	-	-	-

Table 4B: Calculated and weighed amounts of the powders used for the grossular synthesis.

Oxides	calculated (g)	weighed (g)	flux	calculated (g)	weighed (g)
$CaCO_3$	1.70	1.70	$Li_2B_4O_7$	0.45	0.46
Al_2O_3	0.58	0.58	-	-	-
SiO_2	1.02	1.02	-	-	-

Table 5B: Calculated and weighed amounts of the powders used for the LiOH - H_3BO_3 flux.

Flux	calculated (g)	weighed (g)

$LiOH.H_2O$	0.63	0.63
H_3BO_3	2.80	0.21

Table 6B: Calculated and weighed amounts of the powders used for the grossular synthesis.

Oxides	calculated (g)	weighed (g)	flux	calculated (g)	weighed (g)
$CaCO_3$	1.70	1.70	$LiOH.H_2O$ - H_3BO_3	1.02	1.02
Al_2O_3	0.58	0.58	-	-	-
SiO_2	1.02	1.02	-	-	-

Table 7B: Calculated and weighed amounts of the powders used for the grossular synthesis.

Oxides	calculated (g)	weighed (g)	flux	calculated (g)	weighed (g)
$CaCO_3$	1.70	1.70	LiO_2	0.33	0.33
Al_2O_3	0.58	0.58	H_3BO_3	0.43	0.43
SiO_2	1.02	1.02	-	-	-

Table 8B: Calculated and weighed amounts of the powders used for the grossulars synthesis.

Oxides	calculated (g)	weighed (g)
$CaCO_3$	0.63	0.63
Al_2O_3	0.21	0.21
SiO_2	0.38	0.38